Chaosmakers for Epilepsy

by

Aaron Courville

A Thesis submitted in conformity with the requirements

for the degree of Master of Applied Science

Department of Electrical and Computer Engineering

and

Institute of Biomaterials and Biomedical Engineering

University of Toronto

Canada

Abstract

Epileptic seizures correspond to episodes of increased rhythmicity of the chaotic neuronal activity in the healthy brain. It is believed that through the suppression of the rhythmic dynamics, seizures may be eliminated. This is the objective of the chaosmaker.

The chaosmaker employs a Radial Basis Function (RBF) model to learn the chaotic dynamics from the time series. The strategy is to detect the transition to rhythmic activity, then employ nonlinear system theory in a control strategy to return the system to chaotic dynamics. The detection algorithm compares the chaotic dynamics, represented by the RBF model, to the dynamics of the system under observation. Once a change toward rhythmicity is detected the chaosmaker perturbs the measured system variable such that the next state vector is placed on the unstable manifold of the rhythmic cycle. We illustrate the approach with applications to two examples of chaotic systems: the Henon map and the mapped clock oscillator (MCO) model. The chaosmaker was successful at restoring chaotic dynamics in periods of rhythmic activity in both systems.

Acknowledgements

Contents

List of Figures

List of Tables

Chapter 1

Introduction

1.1 A Perspective on Epilepsy

This thesis is an exploration of a novel approach to therapy for individuals with epilepsy. Our strategy is based on recent experimental findings that suggest epilepsy arises from qualitative changes in the dynamics of brain activity. In the healthy brain, the pattern of electrical activity is complex and chaotic. The onset of an epileptic seizure is characterized by rhythmic activity of lower complexity. If neuronal dynamics are controlled to ensure that high complexity activity is maintained then we can achieve suppression of seizures. Just as the pacemaker acts to regulate the activity of the heart to avoid cardiac arrest, our chaosmaker would act to break the rhythmic activity of the brain and thereby suppress epileptic seizures.

One motivation for the development of this strategy is to assist the 20% of the epileptic populations for whom anticonvulsive drug therapies are ineffective. For these individuals, the only recourse currently available is surgery. This involves cutting or removing the area of the brain thought to be the physical source of the seizure, known as the epileptic focus. Surgery can only be considered in cases where the focus is localized away from the major motor and speech centers of the brain. Even in such cases, impairment of language or motor functions can result. It is clear that a need for alternative therapy exists. Our chaosmaker, with its radically different approach to the treatment of epilepsy, could fill this need.

1.2 Objectives

Our objective is to develop a seizure suppression strategy that is applicable to the control of biological neural networks. In order for the chaosmaker to be relevant, its function must not rely on knowledge of the system equations, as these equations are not available for biological neuronal networks. The strategy must be based solely on information provided by a measured time series of the brain's electrical activity. Thus we must begin our development of these strategies with the development of a time series model capable of learning chaotic dynamics.

Before the control strategy can suppress seizures, they must be detected. As a result, we add the development of a detection strategy to our objectives. The method of detection must be able to distinguish the onset of rhythmicity in the dynamics under observation. The algorithm must be capable of reliably detecting all forms of rhythmic activity from the fully developed chaos of the healthy system.

The control strategy must be capable of restoring the chaotic pattern of activity without access to any internal system parameters. An optimal control strategy would quickly restore the chaotic neuronal activity using minimal stimulation. The use of excessive control activity is discouraged because it would result in increased interference with the autonomous functioning of the brain. Our goal is to employ an algorithm which uses the inherent dynamics of the biological neuronal network to maintain chaos.

The long-term objective of this research is to develop a device which is capable of learning the healthy chaotic dynamics of a small part of the brain and detect a change to a rhythmic pattern of activity. Once rhythmicity is detected the device would deliver an electrical stimulus which would restore chaotic activity. Such a device would likely have electrodes implanted in the region of the brain corresponding to the epileptic focus.

1.3 Scope

The work presented here constitutes an early step on the road to realizing the potential of nonlinear system theory to combat epilepsy. As an exploration, we leave many questions unanswered and many avenues of research untraveled. Some of these prospects will be

2

addressed in the section on Future Work concluding this document.

In this thesis, we develop detection and control strategies to detect and eliminate rhythmic dynamics in systems near a transition to chaotic dynamics. These systems represent models of dynamics similar to those observed in the epileptic brain. We also develop the radial basis function (RBF) model as the time series model upon which the detection and control algorithms are based. The effectiveness of these algorithms is demonstrated in their application to two examples of chaotic systems, the Henon map and the Mapped Clock Oscillator (MCO) model.

The first four chapters of this thesis are dedicated to the introduction of background concepts. Chapter 2 provides a brief introduction to a number of concepts which will be used in the development of the detection and control strategies. Chapter 3 contains a review of the literature supporting our claims that the dynamics of epileptic electrical activity may be considered stabilizations of one or more of the infinite unstable periodic orbits located within healthy chaotic activity. Chapter 4 reviews recent work in techniques of controlling chaos that lead to the work of Schiff *et al.* [1] and their attempt to apply these techniques to the brain slice.

Chapters 5, 6 and 7 contain the original research contributions of this thesis. Chapter 5 presents an application of the radial basis function network to learning and modelling chaotic systems. In this chapter, we show the results of learning the chaotic dynamics of two chaotic systems: the Henon map and the mapped clock oscillator (MCO) model of hippocampal CA3 cells. In chapter 6, we describe the rhythmicity detection algorithm and demonstrate its ability to detect spontaneous transitions to periodic activity in the two systems. Chapter 7 contains a description of the control strategy and its application to the Henon map and the MCO model.

1.4 Hypothesis

It is our hypothesis that the RBF model will effectively capture the chaotic dynamics of both the Henon map and the MCO model through access to a time series alone. We further believe that the detection strategy will quickly identify a transition to rhythmic activity with high specificity and sensitivity. Finally it is hypothesized that the control strategy will be

3

effective in restoring chaos during the rhythmic episodes of the two systems.

1.5 Assumptions

As is inevitable in scientific research, the work in this thesis is based on certain assumptions about the natural world. In the development of the detection and control strategies, we make two key assumptions concerning the electrical activity of biological neuronal networks, in both healthy and epileptic brain states

1. Healthy brain dynamics are chaotic. A basic premise of this thesis is that brain dynamics are chaotic, in the sense that they exhibit local instability and are globally bounded to a strange attractor. We assume that the dynamics of the electrical activity of the brain is not critically dependent on any random process and that there is a structure to the patterns of this activity.

2. Epilepsy is rhythmicity from chaos. Epileptic seizures are the physical manifestation of the spontaneous stabilization of unstable patterns of activity in the healthy chaotic brain dynamics. We assume that the stablization of this pattern is the cause of the increased rhythmicity observed in EEG recordings at the onset of epileptic seizures.

Chapter 2

Chaotic Systems

This work draws on a number of basic concepts of nonlinear dynamics. In this chapter we present a brief review of the concepts relevant to the development of the detection and control strategies. We begin by defining chaos and introducing the Lyapunov exponent and the invariant manifold. Next, we describe a number of nonlinear time series analysis techniques that we use throughout the thesis. The final two sections introduce the subject systems to which the learning strategies are applied.

2.1   Chaotic Systems

While there remains no universally accepted definition of chaos, there is some consensus on the characteristics common to chaos. These characteristics are summarized in the following working definition:

> **Chaos** *is longterm aperiodic behaviour in a nonlinear deterministic system that exhibits sensitive dependence on initial conditions [2].*

In this definition, we introduce three separate ideas that are critical to our understanding of chaos, which warrant a little explanation.

Long-term aperiodic behaviour   Chaotic systems can exhibit behaviour which never repeats exactly (see Figure 2.2 for an example of a chaotic time series).

Deterministic System Chaotic systems are deterministic meaning that the evolution of trajectories are not dependent on random or noisy inputs or parameters. The irregular behaviour arises solely from the nonlinear dependence of the evolution of trajectories on the system variables.

Sensitive Dependence on Initial Conditions When a chaotic system is evolved from nearby initial conditions, the resulting trajectories will, on average, diverge exponentially fast. Of all deterministic systems, chaotic systems are the only ones to display sensitive dependence on initial conditions (SDIC) (see Figure 2.4 for an example of SDIC).

2.2 Lyapunov Exponents

SDIC and the aperiodic behaviour of chaotic systems are both consequences of the local exponential divergence of trajectories. This local divergence of trajectories may be quantitatively characterized by the Lyapunov exponents.

Consider, for an n-dimensional system, the evolution of trajectories covering an infinitesimal sphere in the n-dimensional state space. During its evolution, the sphere will become distorted into an infinitesimal ellipsoid. Let $\delta_k(t)$, $k = 1, \ldots, n$, denote the length of the kth principle axis of the ellipsoid. Then $\delta_k(t) \propto \delta_k(0)e^{\lambda_k t}$, where the λ_k are the Lyapunov exponents. There are n distinct Lyapunov exponents for an n-dimensional systems.

Trajectories are diverging exponentially in the direction associated with the positive Lyapunov exponents and converging exponentially in the directions associated with the negative Lyapunov exponents. A Lyapunov exponent of zero indicates that the divergence or convergence is not exponential, but says nothing to indicate if the trajectories are diverging or converging.

2.3 Invariant Manifolds

A k-dimensional manifold in R^n $(1 \leq k < n)$ may be thought of as the solution of the equation

$$\eta(x) = 0 \tag{2.1}$$

6

where $\eta : R^n \to R^{n-k}$ is sufficiently smooth (that is, sufficiently many times continuously differentiable). For example, the unit circle

$$\{x \in R^2 \mid x_1^2 + x_2^2 = 1\}, \tag{2.2}$$

is a one dimensional manifold in R^2. Similarly, the unit sphere

$$\{x \in R^n \mid \sum_{i=1}^{n} x_i^2 = 1\}, \tag{2.3}$$

is an $(n-1)$-dimensional manifold in R^n.

Consider the autonomous system

$$\dot{x} = f(x). \tag{2.4}$$

A manifold $\{\eta(x) = 0\}$ is said to be an invariant manifold for the autonomous system if

$$\eta(x(0)) = 0 \mapsto \eta(x(t)) \equiv 0, \forall t \in [0, t_1) \subset R, \tag{2.5}$$

where $[0, t_1)$ is any time interval over which the solution x(t) is defined. Essentially once a trajectory is on an invariant manifold it will remain on that invariant manifold for all time over which the solution is defined.

There are two types of invariant manifolds that are important to our discussion: stable invariant manifolds and unstable invariant manifolds. Stable invariant manifolds direct trajectories towards a fixed point where $\dot{x} = 0, \forall t \in [0, t_1) \subset R$. Unstable invariant mainfolds direct trajectories away from a fixed point. Eigenvectors are specific cases of invariant manifolds in linear systems.

The deterministic dynamics of chaotic systems evolve along a complex entity in state space known as a strange attractor (see Figure 2.1). The shape of the attractor is determined by the structure and position of the invariant manifolds. The concept of the invariant manifold will become important in the development of the chaos preservation strategy.

2.4   Time Series Analysis

Very often when studying biological systems, accurate mathematical models are not available and one has to study the system from an observed time series alone. This is exactly the

case for the brain, our system of interest. While relatively good models of the electrical activity of individual neurons exist; the interactions of the countless number of cells that form the organization of the brain is well beyond our ability to model at the cellular level. Yet, there is significant evidence for structure in the recording of the electrical activity of neurons embedded in networks. This evidence is reviewed in Chapter 3. Here we shall review some of the tools we use to analyze nonlinear time series data.

2.4.1 State Space Reconstruction

In sections 2.1 to 2.3, we described the properties of chaotic systems. Through this description we relied heavily on the concept of the state space. Unfortunately, we measure results in a time series and not a state space. In order to bring to bear our tools and intuitions concerning deterministic systems, we require a representation of the time series data in the form of a state space. This is the problem of state space reconstruction and it is solved by the method of delays.

Let us refer to the "true" continuous time state vector as z_R. The time series is a sequence of scalar measurements of $z_R(t)$, taken at multiples of some fixed sampling time,

$$s_n = s(z_R(n\Delta t)) + \zeta_n \tag{2.6}$$

where s is some measurement function, n is an integer and ζ_n is the measurement noise. A delay reconstruction in m dimensions may be constructed as a set of vectors s_n given as

$$s_n = (s_{n-(m-1)\nu}, s_{n-(m-2)\nu}, \cdots, s_{n-\nu}, s_n) \tag{2.7}$$

where ν is the *delay time* between adjacent components of the delay vectors. The dimension m is often referred to as the embedding dimension.

Taken's theorem of embedding [3] confirms the equivalency between the vector reconstruction and the original trajectory $z_R(t)$ in the sense that there exists a mapping onto each other by a uniquely invertible smooth map. The theorem are primarily concerned with the situation where the dimension of the original system is unknown. In this work, we will be dealing with a system of known dimension. The embedding dimension will simply be made equal to the known system dimension.

8

Embedding of interspike intervals: In certain types of time series, the measured signal is relatively uninteresting and the information is encoded in the time between characteristic events within the time series. The measured transmembrane voltage of a neuron is such a time series, where the information is contained in the time between action potentials. Thus, a new series series is defined as the time between action potential [4]. This time series is peculiar in that the "time" becomes the event (or action potential) number and no longer corresponds to a true measure of time.

The question of whether such a transformation of the measured time series preserves the equivalence between the reconstructed phase space and the original phase space topologies was addressed by Sauer in 1994 and 1995 [5] [6]. Sauer showed that if a) the spikes are generated by an *integrate-and-fire* process and b) the underlying signal is deterministic, then the embedding is valid and the time delay interspike interval embedding yields a faithful reconstruction of the state space. It is generally supposed that the integrate-and-fire process holds for the creation of action potentials in the neuron [4].

2.4.2 Maximal Lyapunov Exponents

In section 2.2 we introduced the concept of the Lyapunov exponent. Here we shall discuss how one might measure Lyapunov exponents from time series. Measuring the full spectrum of Lyapunov exponents is an extremely difficult task without a good model of the system. Fortunately, we can calculate the largest Lyapunov exponent relatively easily from the time series. The largest Lyapunov exponent represents a measure of the average exponential divergence of nearby trajectories, and is given by the slope of the linear portion of the plot of $S(\Delta n)$, where

$$S(\Delta n) = \frac{1}{N_o} \sum_{n_0=1}^{N^o} \ln \left(\frac{1}{|\mathcal{U}(s_{n_0})|} \sum_{s_n \in \mathcal{U}(s_{n_0})} |s_{n_0+\Delta n} - s_{n+\Delta n}| \right). \tag{2.8}$$

The embedding vectors s_{n_0} are reference points; N_o is the number of points in the time series; $\mathcal{U}(s_{n_0})$ is the neighbourhood of s_{n_0} with diameter ϵ. The term s_{n_0} is the last element of s_{n_0}, thus $s_{n_0+\Delta n}$ is outside the time span covered by the delay vector s_{n_0} [4], [7].

In the calculation of $S(\Delta n)$, one has to choose a vector s_{n_0} in the reconstructed state space and select all neighbours within a distance ϵ and compute the average over the

9

distances of all neighbours to the reference part of the trajectory as a function of the relative time (Δn). The maximal Lyapunov exponent is estimated by the slope of the linear region. The curve saturates at the mean distance between two arbitrary embedding vectors on the attractor.

2.4.3   Correlation Dimension

The correlation dimension measurement is a nonlinear analysis tool that measures the complexity of the attractor in state space. In Chapter 3 we use the correlation dimension measurements of neuronal activity published over the last 15 years to support our assumptions regarding the presence of deterministic chaos in the brain and in epilepsy.

Following the algorithm introduced by Grassberger and Procaccia [8], one constructs m-dimensional spheres of radius r centered on each point of the m-dimensional embedded attractor. The radius is decreased while the number of points inside each sphere is counted. A log-log plot is made of the number of points inside the spheres as a function of radius size for various embedding dimensions. If one observes no change in the slope of the log number of points over a region of radius values or with increasing embedding dimension, then the slope is an estimate of the correlation dimension, D_2.

The correlation dimension measures the degree to which the state space is filled for a given embedding dimension, m. In this way, it provides a measure of the complexity of the dynamics by measuring the degrees of freedom available to the system. If, for a given embedding dimension, the embedded attractor fills the space then the dynamics have equal or greater degrees of freedom than are represented by the embedding dimension. In this way, we can potentially separate deterministic signals from noise by searching for a saturation of the correlation dimension with increasing m. For noise, the slope of the log number of points inside each sphere will always continue to change as m increases.

2.5   Subject System I: The Henon Map

The Henon map is a classic example of a two dimensional map with a strange attractor. Originally devised by Michel Henon (1976) to explore the microstructure of strange attractors, we shall use it as our first subject system [2]. We apply the detection and control

algorithms th the subject systems, $\mathcal{F}$, in an effort to promote chaotic activity through periods of rhythmic activity. In both subject systems, the rhythmic dynamics arise from small parameter changes away from the chaotic regime.

The Henon map is typically described by the two dimensional difference equation:

$$x_{n+1} \;=\; 1 + y_n - ax_n^2, \tag{2.9}$$

$$y_{n+1} \;=\; bx_n, \tag{2.10}$$

where a and b are parameters. As a two dimensional system the Henon map has two variables: x and y. As we discussed in section 2.4, time series are in scalar form which must be converted to vectors through the method of delays. If we imagine placing an observer on only one variable of the Henon map, say x, then we can re-express the Henon map in a form compatible with the method of delays,

$$x_{n+1} = 1 - ax_n^2 + bx_{n-1}. \tag{2.11}$$

In this form, we see that the state is represented by a vector of delays: $[\; x_{n-1} \quad x_n \;]$. Throughout this thesis, when we refer to the Henon map, we are referring to the delayed variable form given in equation 2.11.

2.5.1 The Chaotic Henon Map

If we choose the parameter values $a = 1.4$ and $b = 0.3$, the resulting dynamics are chaotic. These are the classical values of a and b which Henon chose to study. Figure 2.1 illustrates the strange attractor of the chaotic Henon map with $a = 1.4$ and $b = 0.3$.

The time series of the chaotic Henon map, given in Figure 2.2, illustrates the aperiodic character of chaotic systems. There is never an exact repeat of a previous pattern. A slightly different representation of the chaotic Henon map time series is shown in Figure 2.3. In this form, the discrete nature of the Henon map is accurately illustrated as disconnected dots. Both time series representations are used interchangeably throughout the thesis to better illustrate the various aspects of interest.

Figure 2.4 illustrates the sensitive dependence on initial conditions (SDIC) characteristic of chaotic systems in the Henon map. The figure shows the time series that corresponds to two nearby trajectories. Initially, the two time series seem to follow each other closely,

11
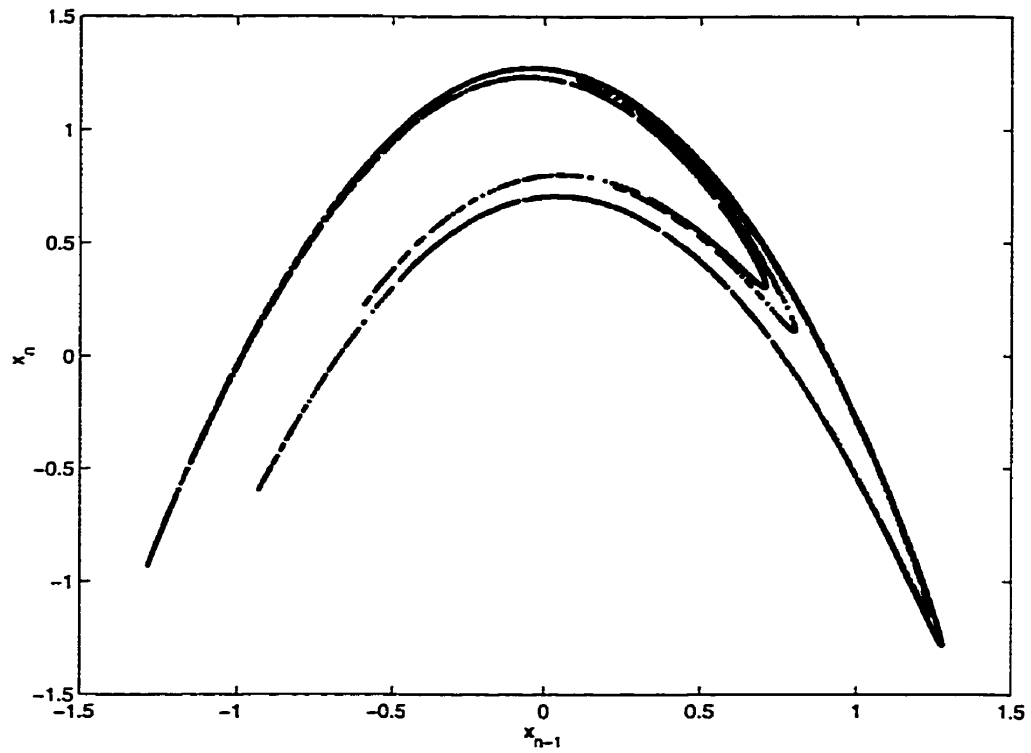
Figure 2.1: *The strange attractor of the Henon map with $a = 1.4$ and $b = 0.3$. The attractor is formed by 5000 iteration of the Henon map.*
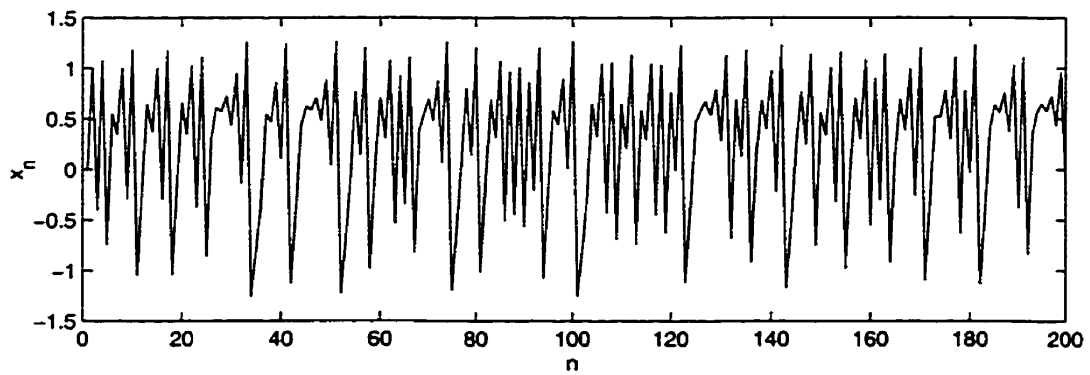
Figure 2.2: *The times series of the Henon map with $a = 1.4$ and $b = 0.3$.*
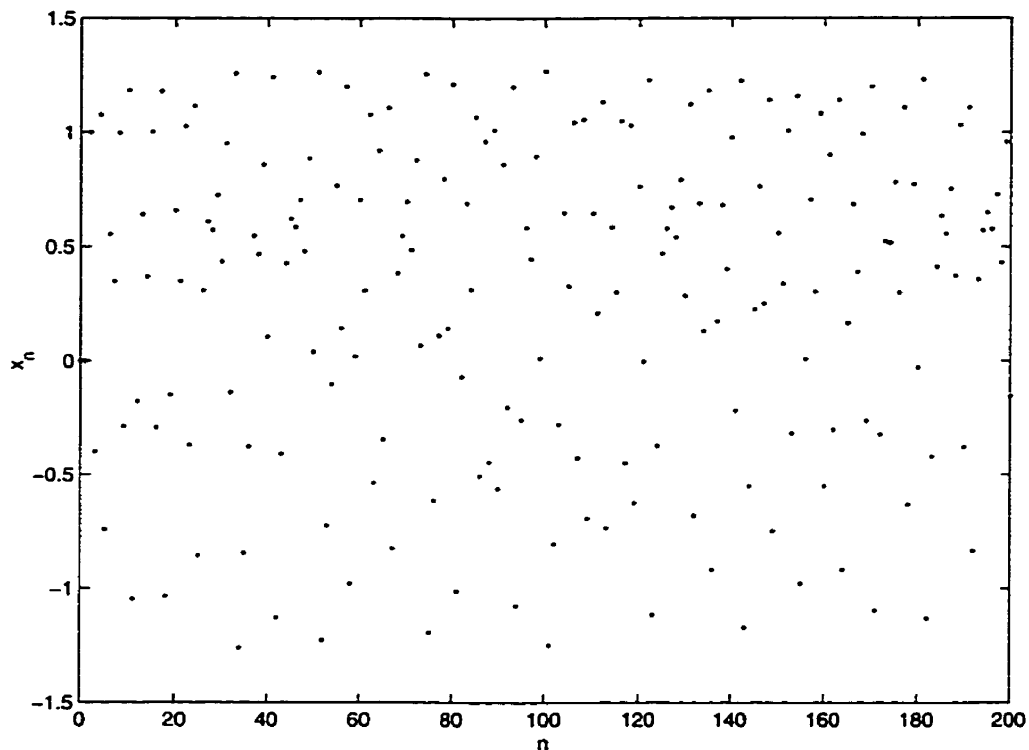
Figure 2.3: A Discrete time representation of the chaotic Henon map time series.

then quickly diverge. The pattern of divergence represented in Figure 2.4 is indicative of local exponential divergence. As discussed previously in this chapter, the local mean divergence is measured by the Lyapunov exponents. The result of the calculation of $S(\Delta n)$, of equation 2.8, from the time series of the Henon map is given in Figure 2.5. The straight line at the beginning of the curve reflects the exponential divergence of nearby trajectories within chaotic systems. The slope of the line is an estimate of the maximal Lyapunov exponent, which in the case of the Henon map is 0.4169 [7]. The curve eventually saturates as the originally nearby trajectories separate to the average distance between points on the attractor.
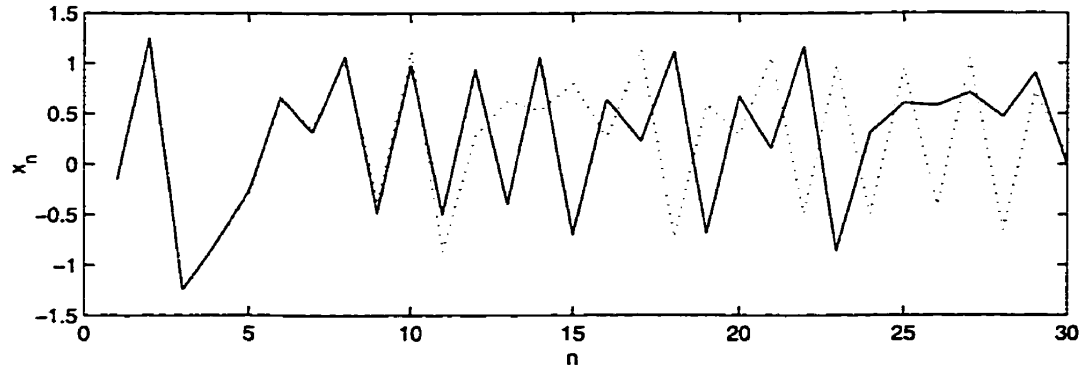
Figure 2.4: *The time series of the evolution of two nearby trajectories of the Henon map with a = 1.4 and b = 0.3. SDIC is evident in the divergence of these signals.*
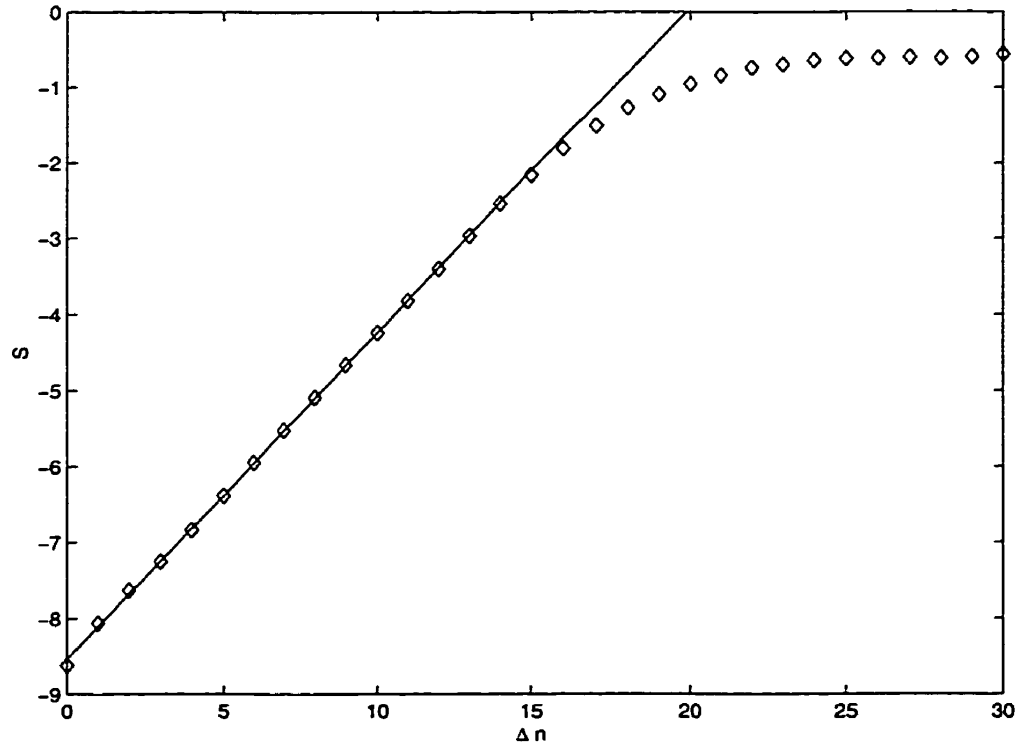
Figure 2.5: *The results from the computation of $S(\Delta n)$ from a time series of the Henon map with a = 1.4 and b = 0.3. The slope of the fitted line represents an estimate of the maximal Lyapunov exponent of 0.4169.*
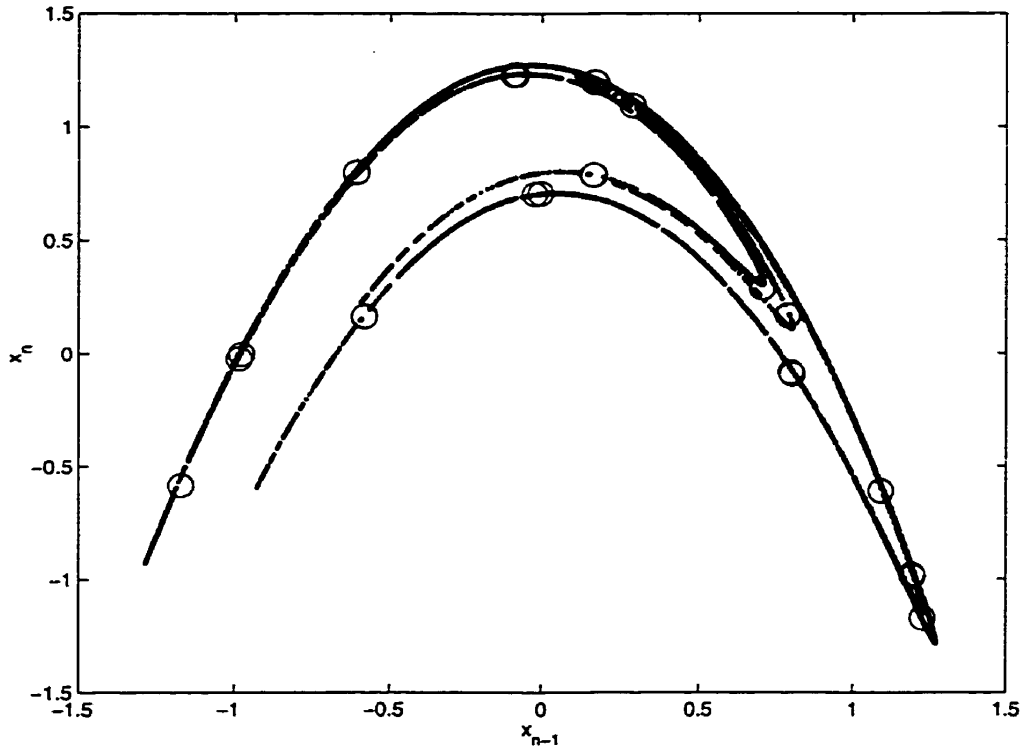
Figure 2.6: *The periodic orbit of the Henon map with* $a = 1.42207$ *and* $b = 0.3$ *(open circles) superimposed on the strange attractor of the Henon map with* $a = 1.4$ *and* $b = 0.3$ *(solid dots).*

2.5.2 The Periodic Henon map and Chaotic Transients

If we change parameter a slightly to a value of $a = 1.42207$ while keeping $b = 0.3$, the Henon map enters a narrow region of periodic activity. The dynamics are period-30, meaning that the periodic cycle repeats exactly after every 30 time steps. As illustrated in Figure 2.6, the period-30 orbit appears directly on the strange attractor which exists for $a = 1.4$, suggesting that the small change in a has stabilized one of the unstable periodic orbits of the chaotic Henon map. This brings to mind our perspective that epilepsy arises from the stabilization of the higher complexity activity present in normal brain activity.

Figures 2.7 and 2.8 show the time series of the Henon map with $a = 1.42207$ and, as always, $b = 0.3$. The time series begins with a nonperiodic signal that is qualitatively different from the period-30 pattern that follows. This aperiodic segment of the time series is termed a chaotic transient because it demonstrates the properties of aperiodicity and SDIC;
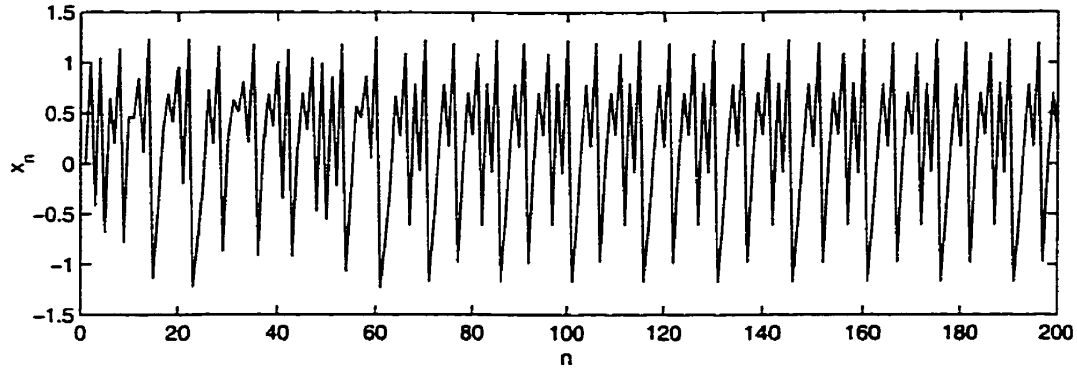
Figure 2.7: *The times series of the Henon map with* a = 1.42207 *and* b = 0.3. *Note the chaotic transient present in the early stages of the time series*

however its temporary nature excludes it from being considered true chaos.

Chaotic transient behaviour is ubiquitous in systems near the transition from chaos to periodicity. From a state space perspective, the transient arises from the influence of the invariant manifolds which, outside the immediate neighbourhood of the stable periodic orbit, resemble their structure in the chaotic regime. Trajectories evolve along the "shadow" of the chaotic attractor until they enter the region in state space for which the periodic orbit is the attractor. Once inside the attracting region of the periodic orbit, the unperturbed trajectories will remain indefinitely. In general, a larger attracting region of the periodic orbit increases the likelihood that each trajectory iteration will appear inside the attracting region. Once inside, the chaotic transient ends.

The presence of chaotic transients is an important characteristic to those attempting to revive chaos in chaotic systems that have drifted into periodic activity. We will use chaotic transients to our advantage in our control strategy developed in Chapter 7.
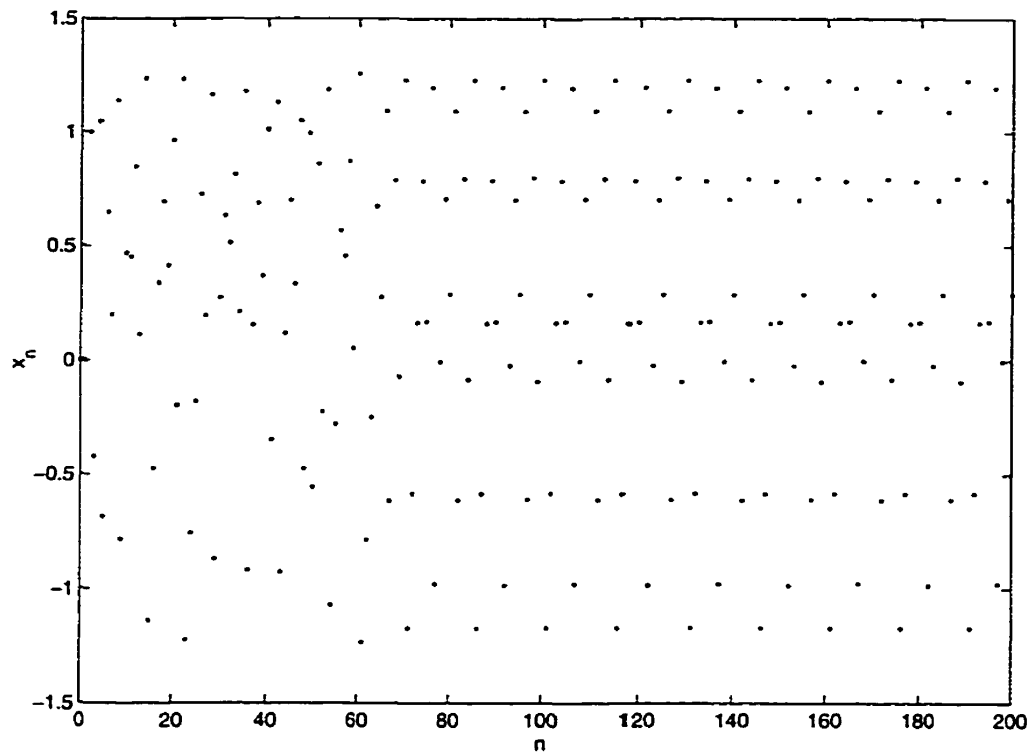
Figure 2.8: *A Discrete time representation of the periodic Henon map time series. Note the chaotic transient (represented by the disordered array of dots) before the periodic steady state (represented by the bands of dots) is reached.*

2.6 Subject System II: The Mapped Clock Oscillator

The second system to which we apply our detection and control strategies is the coupled mapped clock oscillator (MCO) model [9] [10]. The MCO model was developed by Berj L. Bardakjian, with his students and colleagues, to describe phenomena observed in the transmembrane voltage activity of excitable cells. The model describes cellular transmembrane voltage arising from a mapping of an intracellular clock. In the form applied in this thesis, the MCO model describes the transmembrane voltages of interacting cells in the CA3 region of the rat hippocampal slice preparation. Given the attempt by Schiff et al. to implement control chaos in the rat hippocampal slice [1], this seems an appropriate model with which to apply our chaos making strategy.

In the MCO model, a cell is represented by two components: the clock and the transformer. The clock is described by a system of two first order nonlinear differential equations. Within the clock are all the dynamics elements of the model. The transformer is a static nonlinearity that maps the state variables of the clock onto the observed output that represents the transmembrane voltage of the cell. In this thesis, we use an arrangement of two symmetrically coupled MCO model cells, previously explored in our lab by Richard Aschenbrenner-Scheibe [9]. MCO model cells are coupled together through portals emulating various forms of physical interactions. Figure 2.9 shows a schematic representation of the symmetrically coupled, two cell MCO model.

The Clock: The system of nonlinear differential equations describing the clock of the nth coupled cell is given by [9],

$$\dot{u}_{1n} = \omega_n[u_{2n}(1 + S_{\phi n}) + u_{1n}(1 + S_{\alpha n} - u_{1n}^2 - u_{2n}^2)] + S_{\gamma 1n} \qquad (2.12)$$

$$\dot{u}_{2n} = \omega_n[-u_{1n}(1 + S_{\phi n}) + u_{2n}(1 + S_{\alpha n} - u_{1n}^2 - u_{2n}^2)] + S_{\gamma 2n} \qquad (2.13)$$

where u_{1n} and u_{2n} are the state variables of the nth coupled cell and ω_n is its intrinsic frequency. The quantity $S_{\alpha n}$ represents a stimulus that changes the amplitude of the nth cell. The stimulus $S_{\alpha n}$ is applied to the cell through the so called portal P_α. Similarly, the frequency stimulus $S_{\phi n}$ is applied through the portal P_ϕ. The quantities $S_{\gamma 1n}$ and $S_{\gamma 2n}$ are stimuli applied through the gamma portal P_γ. The portals are the entry points into the

18
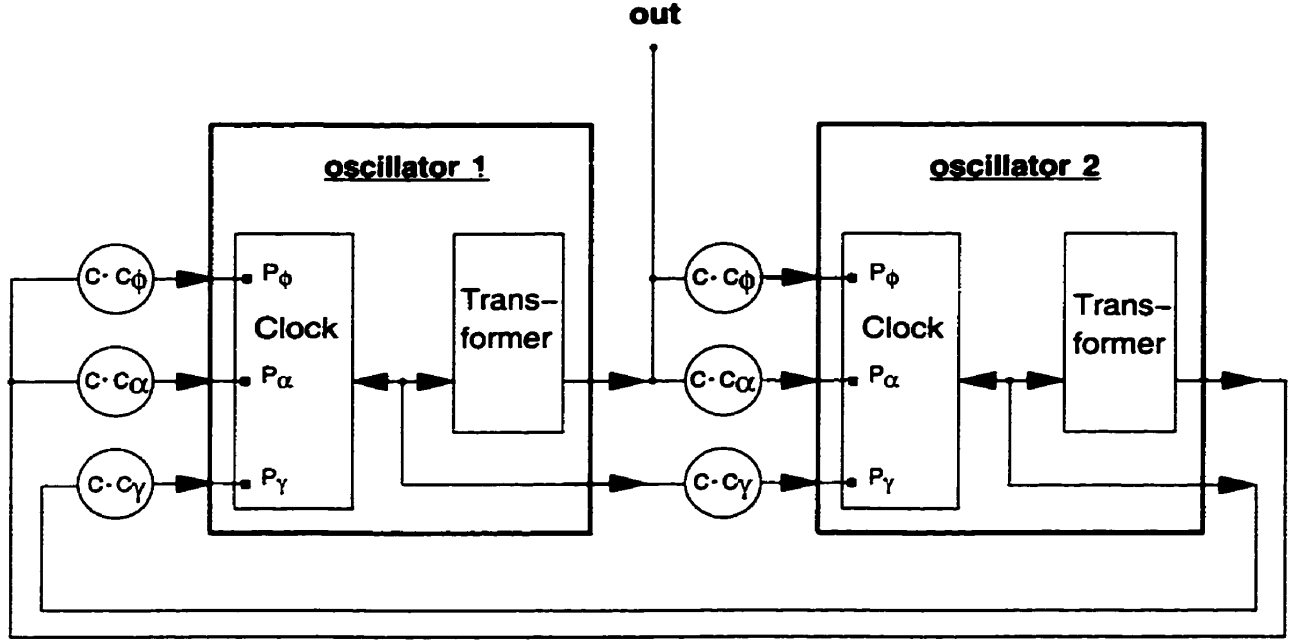
Figure 2.9: *Schematic representation of the MCO model. Input portals,P_ϕ, P_α and P_γ receive the stimuli portions defined by the coupling factors c_ϕ, c_α and c_γ. c is the common coupling factor [9].*

dynamics of the MCO cell model representing electric field and electronic (gap junctional) coupling pathways.

In the case of two symmetrically coupled oscillators, the input stimuli for the nth cell originate from the mth cell and are given by

$$S_{\phi n} = cc_\phi y_m / \psi_n,$$ (2.14)

$$S_{\alpha n} = cc_\alpha y_m / \psi_n,$$ (2.15)

$$S_{\gamma 1 n} = cc_\gamma u_{1m} / \delta_n,$$ (2.16)

$$S_{\gamma 2 n} = cc_\gamma u_{2m} / \delta_n,$$ (2.17)

$$(2.18)$$

where c_ϕ, c_α and c_γ are the symmetric coupling factors and c is the common coupling factor and is set as $c = 1$ for this thesis. The parameters ψ_n and δ_n are normalization factors with values of 6.5881 and 0.1 respectively [9]. The variable y_m represents the transformer of the mth cell.

19

Parameter	Value
ω_1	20π
ω_2	1.5π
c_ϕ	0.1175
c_α	0.0996
c_γ	0.0996
a_{01}	-54.5226
a_{02}	-54.5226

Table 2.1: *The parameter values for the MCO model with chaotic dynamics.*

The Transformer: The transformer is a mapping of the state variables of the clock onto the observable output which represents the transmembrane voltage of a CA3 neuron shown in Figure 2.10. For the nth cell, the transformer is given by the equation [9],

$$y_n = a_{0n} + \sum_{k=1}^{K}[a_{kn}\rho_n T_k(u_{2n}/\rho_n) + b_{kn}u_{1n}U_{k-1}(u_{2n}/\rho_n)], \tag{2.19}$$

where $\rho_n = \sqrt{u_{1n}^2 + u_{2n}^2}$, k is the harmonic index, a_{0n} is the average intrinsic level of the waveform of the nth cell, a_{kn} and b_{kn} are the Fourier coefficients of the time series representing intrinsic oscillation of the transmembrane voltage. The terms $T_k(\cdot)$ and $U_k(\cdot)$ represent the kth Tchebychev polynomials of the first and second types respectively.

2.6.1 The Chaotic MCO model

For the values of the parameters shown in Table 2.1, the symmetrically coupled two cell MCO model displays chaotic dynamics. The values presented in Table 2.1 were taken from [9]. As indicated in the schematic of the MCO model (Figure 2.9), we measure the output of the transformer of Oscillator 1. Figure 2.11 illustrates the output of Oscillator 1, y_1, that represents the transmembrane voltage. The plot of y_1 clearly shows the aperiodic characteristic of chaotic systems. A closer view of the evolution of y_1 with time, t, is shown in Figure 2.12.

Following the interspike interval embedding technique described in section 2.4.1, we convert the continuous time dynamics from the differential equations 2.12 and 2.13 into a
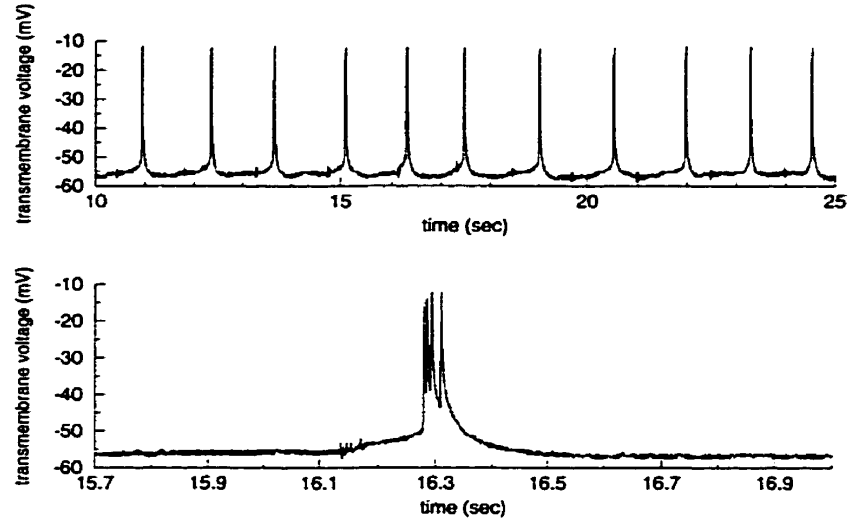
(a) Intracellular recording form CA3 puramidal cell.
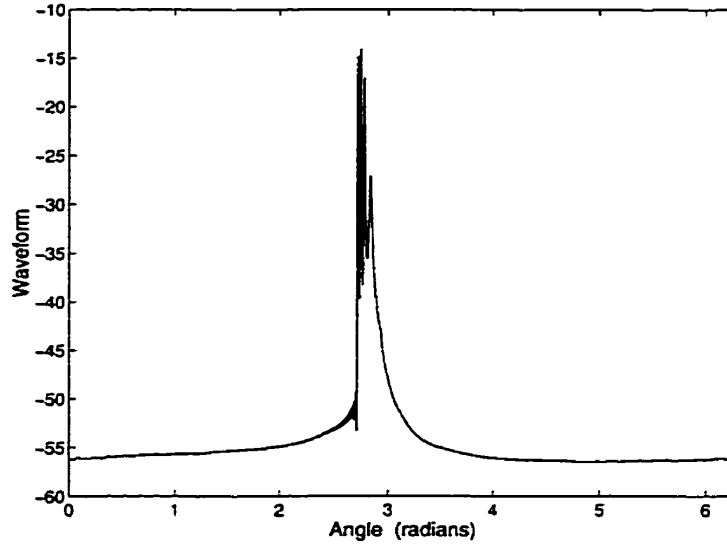
(b) The waveform of the transformer.

Figure 2.10: The intrinsic waveform (b) to which the state variables are mapped through the transformer. The waveform is derived from an ensemble of action potentials from a recording of the transmembrane voltage of a CA3 neuron in the rat hippocampal slice, as shown in (a) [9]. The bottom trace of (a) is a typical burst from the transmembrane recording.
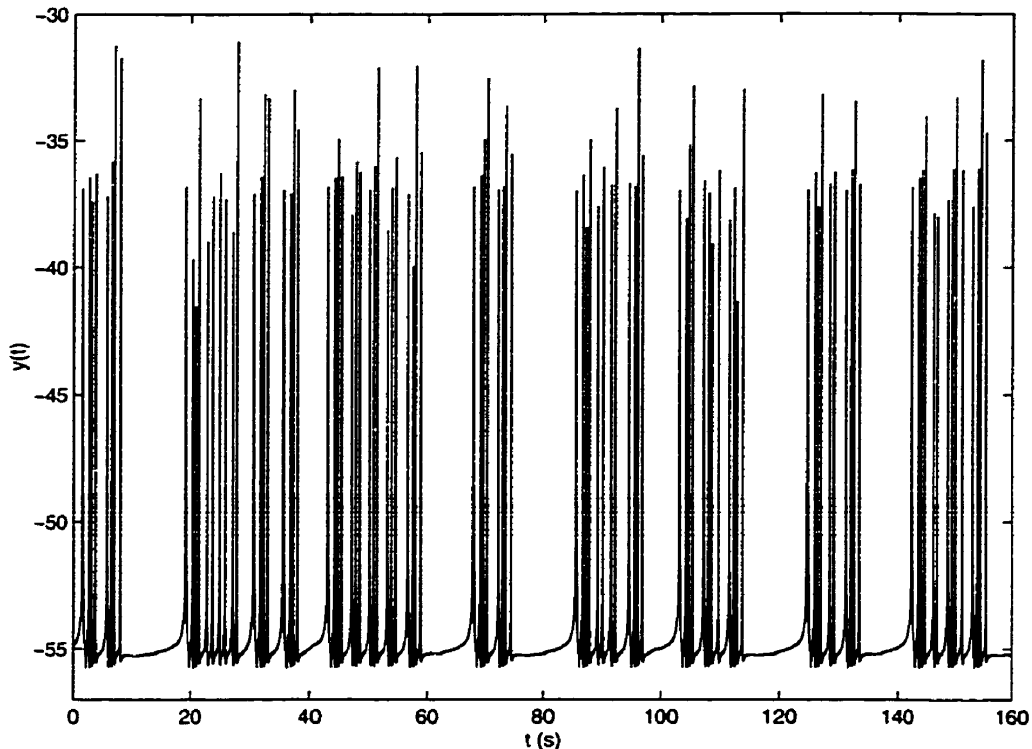
Figure 2.11: *The chaotic output of the MCO model with the parameters given in Table 2.1.*

time series with discrete time dynamics. Figure 2.13 shows the interspike interval (I) time series taken from the MCO model output shown in Figure 2.11.

The two oscillator MCO model has two sets of the clock variables, making it a four dimensional dynamic system. Therefore, we must embed the interspike interval time series in a four dimensional state space in order to fully unfold the dynamics. Four dimensional systems do not lend themselves easily to visual representations; however, a plot of the first return map, given in Figure 2.14, reveals a two dimensional projection of the four dimensional strange attractor.

Finally, to confirm that the interspike interval time series taken from the MCO model reflects the chaotic nature of the original output variable y_n (which itself was confirmed to be chaotic in [9]), we calculate the maximal Lyapunov exponent. Figure 2.15 shows that $S(\Delta n)$ has a linear region, with a positive slope at the beginning of the curve confirming that the interspike interval time series is chaotic. The maximal Lyapunov exponent was estimated from the slope to be 0.48.

22
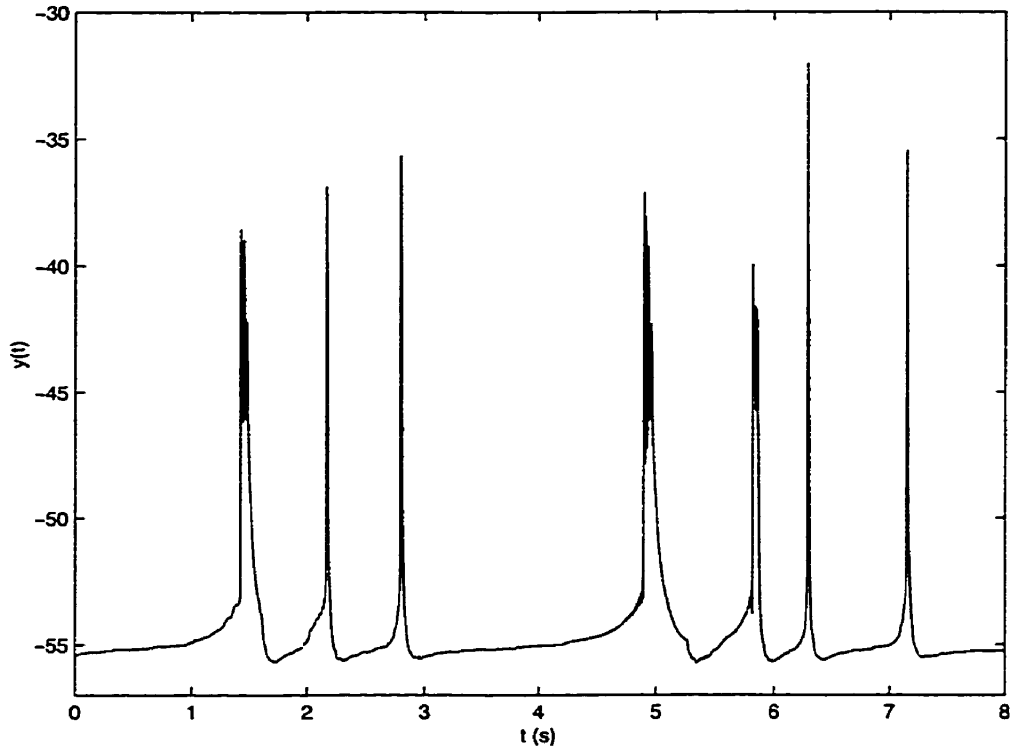
Figure 2.12: A closer view of the evolution of y_1 for the chaotic MCO model.
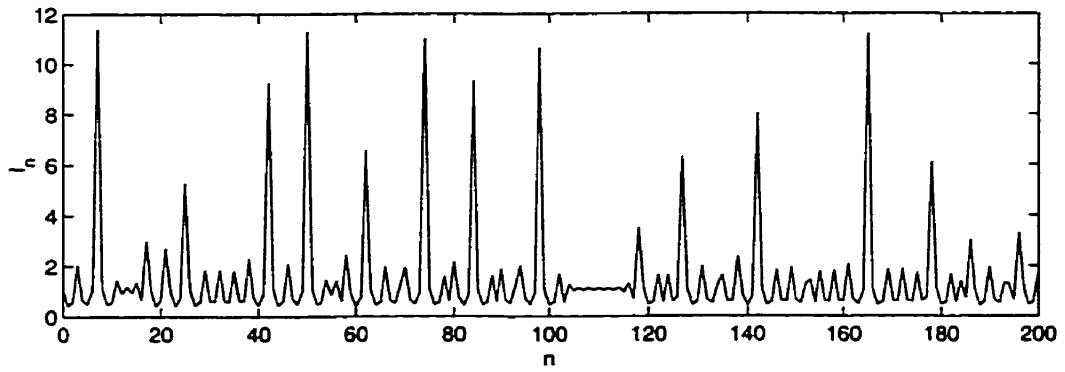
Figure 2.13: Interspike interval time series for the MCO model, taken from the MCO model output shown in Figure 2.11.

23
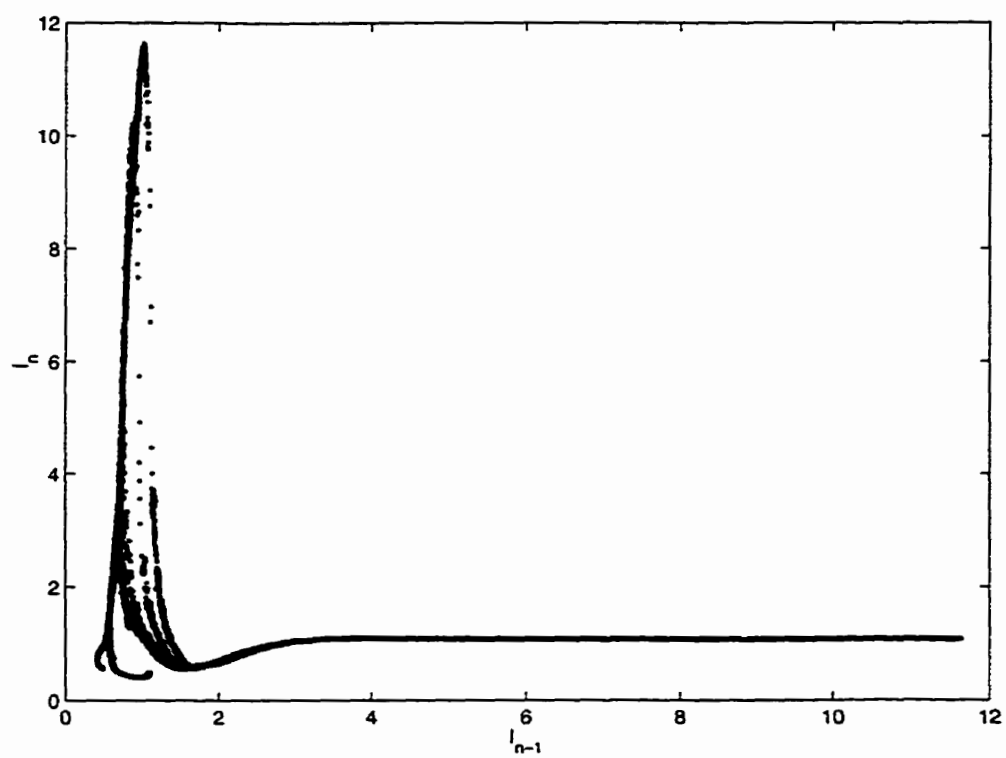
Figure 2.14: *The First return map of a MCO interspike interval time series with 25000 points.*
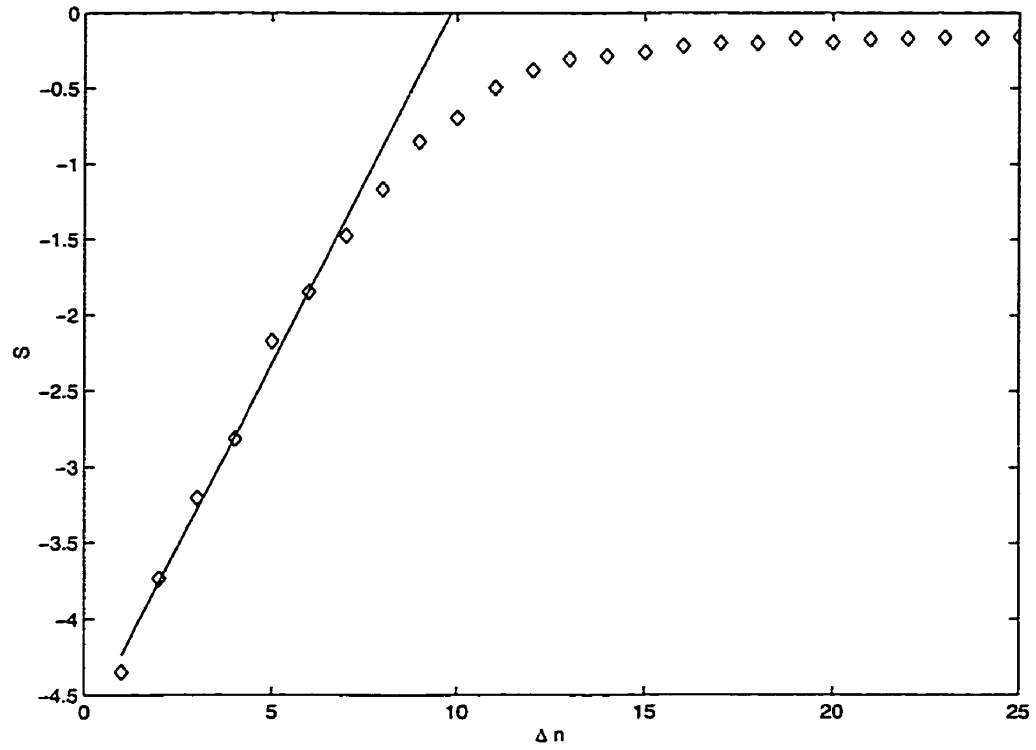
Figure 2.15: The plot of $S(\Delta n)$ for the interspike interval of the MCO model. The slope estimates the maximal Lyapunov exponent at 0.48.
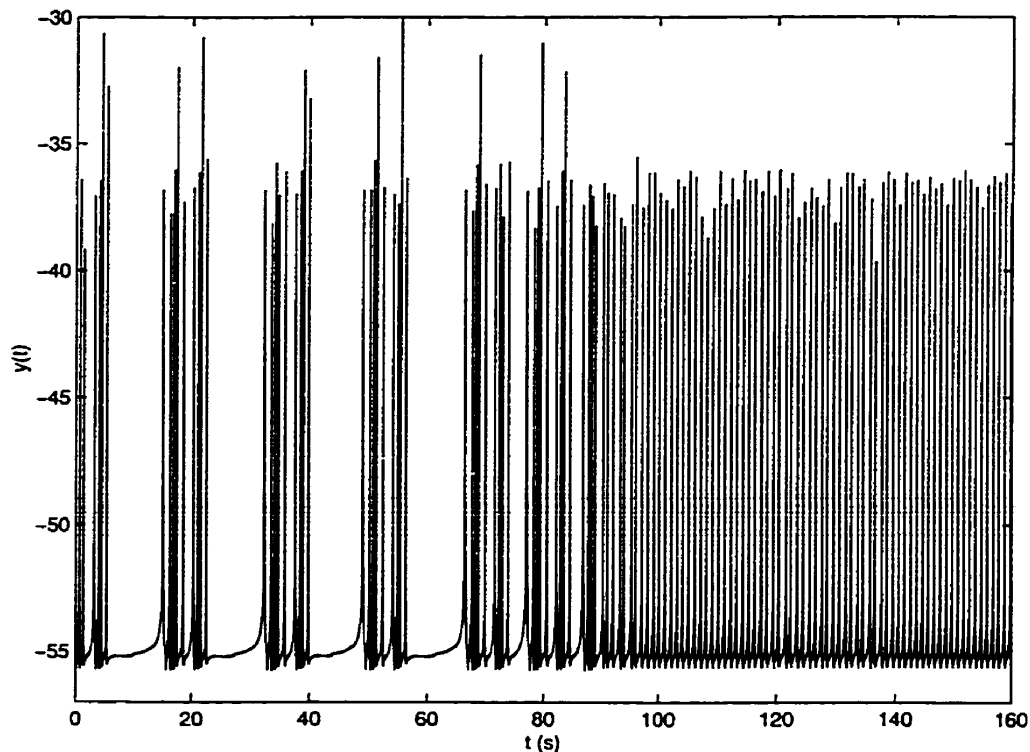
Figure 2.16: *The transition to rhythmic activity of the intermittent MCO model* $(a_{01} = -54.7726)$.

2.6.2 The Intermittent MCO Model

Just as in the case of the Henon map, we seek a region of rhythmic dynamics in the MCO, present within a small change in a parameter value from the chaotic system. Maintaining parameters values as shown in Table 2.1, with the exception of a_{01} which we decrease by 0.46% to -54.7726 results in rhythmic behaviour intermittent with bursts of chaos of variable duration. As is the case with chaotic transients, intermittency is common in systems near a transition from periodic to chaotic activity.

Figure 2.16 illustrates the transition to the rhythmic dynamics of the MCO output, $y_1(t)$. At time $t = 0$ seconds, the value of a_{01} is changed from $a_{01} = -54.5226$ (the value corresponding to the chaotic MCO model) to $a_{01} = -54.7726$. After some time, the time series shows the MCO model slipping into rhythmic activity close to a period-1 orbit. In recording of rat hippocampal neurons in the slice, a similar pattern of intermittent stabilization of a near period-1 cycle was observed (private communication with J. L. Perez Velazquez).

26
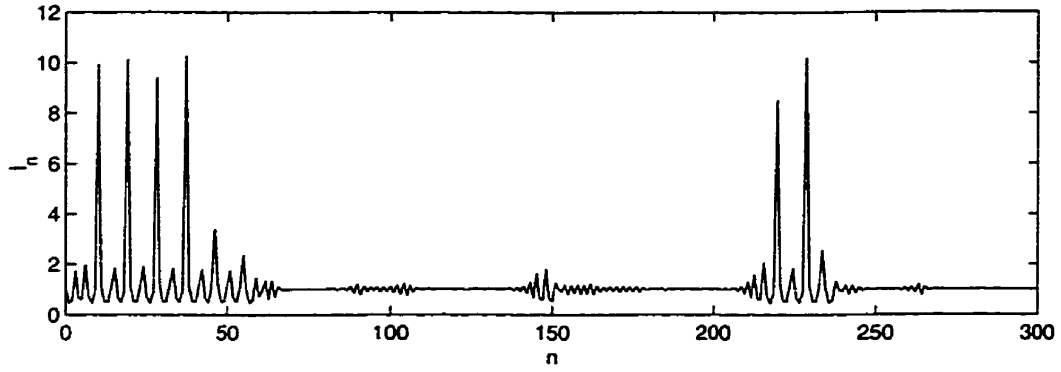
Figure 2.17: *The interspike interval time series of the intermittent MCO model.*

Applying the interspike interval encoding of y_1 from the intermittent MCO model results in the discrete time series shown in Figure 2.17. In this time series, the intermittent character of the model is reflected in the brief burst between $n = 200$ and $n = 250$.

Similar to the periodic orbit in the Henon map, Figure 2.18 shows that the rhythmic orbit of the interspike interval of the intermittent MCO model (with $a_{01} = -54.7726$) appears to land directly on the image of the chaotic attractor which exists for $a_{01} = -54.5226$.

From the perspective of a control strategy, the intermittent behaviour of the MCO model is not substantially different from the chaotic transient activity of the Henon map. In both systems, there exists a region of state space where, once inside, the trajectories enter into rhythmic orbits. In the case of the intermittent MCO model, the trajectory will repeatedly escape to temporary chaotic activity between periods of rhythmicity.
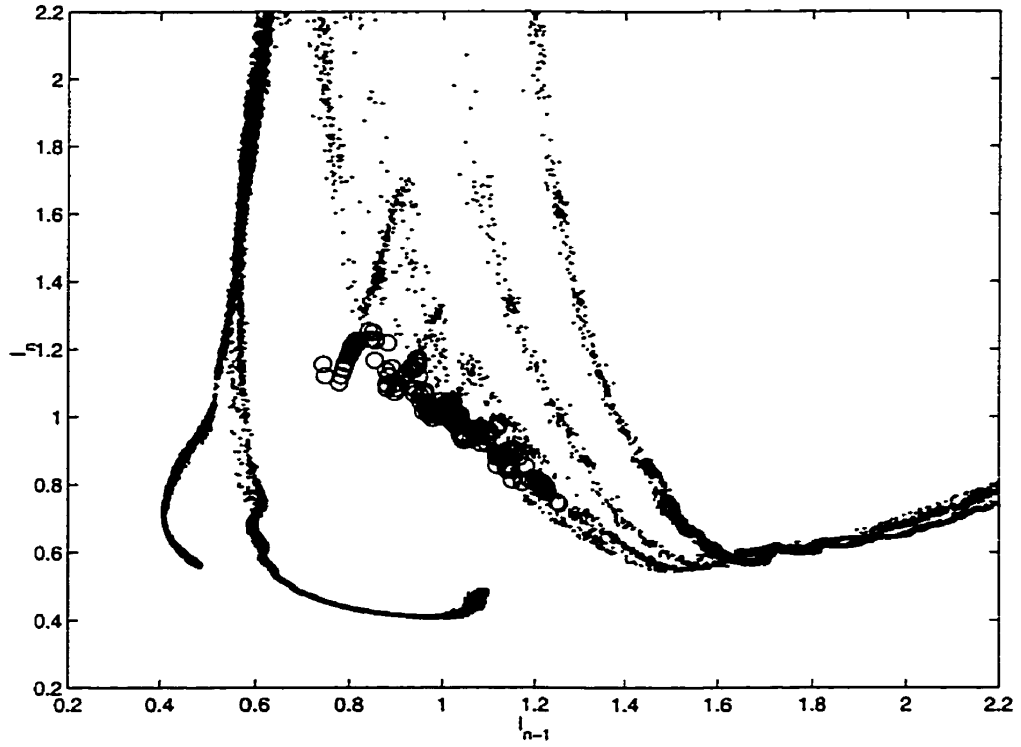
Figure 2.18: *The first return map of the rhythmic region of the time series of the intermittent MCO model (open circles), superimposed on the first return map of the chaotic MCO model (solid dots).*

Chapter 3

Literature Review I: Chaos, Brain and Epilepsy

In this chapter we review the literature addressing the possibility of chaos and deterministic dynamics in the electrical activity of the brain and neurons. We will also present a review of the experimental evidence in support of our claim that epileptic seizures correspond to instances of increased rhythmicity and lowered complexity in comparison with healthy brain activity. In addition, we will offer evidence in support of our assumption that the dynamics associated with epileptic seizures are accurately described as periodic orbits embedded within the highly complex, chaotic attractor of the nonepileptic brain activity.

3.1 Chaotic Neurodynamics

Before we review the literature pertaining to chaos in whole brain activity, we provide a summary of the body of knowledge regarding the characterization of chaos from time series taken from transmembrane voltage recordings.

The search for deterministic nonlinear dynamics in neuronal system became popular in the mid-80s with the development of an effective algorithm to compute the pointwise correlation dimension [8]. In 1985, Rapp et al. [11] used the correlation dimension algorithm of Grassberger and Procaccia to analyze the spontaneous activity of neurons in the precentral and postcentral gyri of an anesthetized squirrel monkey. Single cell action potentials were recorded extracellularly and encoded in an interspike interval time series from which the

correlation dimension was computed. Of the 10 cells from which they report measuring the correlation dimension, 3 cells demonstrated resolvable correlation dimensions (postcentral: 3.5 ± 0.1, 2.2 ± 0.1 and precentral: 2.9 ± 0.1). The remaining 7 cells did not produce inter-spike interval time series with resolvable correlation dimensions. The fractional correlation dimension recorded from those 3 cells provides evidence for the presence of deterministic dynamics forming a strange attractor in a reconstructed state space, a common characteristic of chaotic systems.

Since the first studies that indicated low dimensional neurodynamics as measured by the correlation dimension algorithm, several researchers have reported spurious detections of low-dimensional deterministic dynamics from the correlation dimension algorithms applied to simple coloured noise [12] [13]. In reaction to these findings, many researchers have turned to the method of *surrogate data* [14] [15] where the analysis of the time series is compared with that of a fabricated random time series having identical statistical properties as the original data. If the correlation dimension of the original time series is indistinguishable from the correlation dimension computed from the fabricated time series then the system does not exhibit determinism.

In 1994, Schiff et al. used several methods to evaluate whether there was a statistically significant degree of determinism both in the dynamics of the monosynaptic spinal cord reflexes of the cat [16] and in the dynamics of the rat hippocampal slice recorded from the CA1 region [17]. The methods used to investigate determinism included a nonlinear prediction method and a method of evaluating the local divergence of trajectories within the reconstructed state space. They found that, although most samples failed to produce statistically significant evidence for determinism, there were instances of significant determinism in both the monosynaptic spinal cord reflex (2/4 samples in the decerebrate state) and in the rat hippocampal slice (1/6 samples in the autonomously bursting high [K^+] state).

In recent years new techniques for the characterization of deterministic dynamics have been developed which center on the existence of an infinite number of unstable periodic orbits (UPOs) embedded within chaotic attractors [18]. These techniques generally search the time series for rare events characteristic of UPO dynamics, such as certain nearby trajectories having predictable short term behavior. The statistical significance of the frequency of these rare event may be tested by comparison with a surrogate time series. The technique was

applied by Pei et al. [19] who used it to find evidence for determinism in the dynamics of the crayfish caudal photoreceptor subject to stimuli representative of the animals natural habitat. Pei et al. found statistically significant ($p < 0.05$) evidence for UPOs over a range of stimulus frequency and intensity. Their results suggest the existence of deterministic chaos.

So et al. [20] have recently applied a UPO detection technique to the recording of the CA1 region of transversely and longitudinally cut in vitro rat hippocampal slices. Their UPO detection technique employs a periodic orbit transform which acts to concentrate the transformed data about distinct UPOs [21] [22]. So et al. report statistically significant evidence for the presence of UPOs [1] from the interspike interval time series obtained from both extracellular recordings of ensemble burst firing and intracellular patch-clamp recording of single cells in the CA1 region. Every intracellular experiment revealed at least one instance of a detectable UPO. Roughly half of the extracellular experiments revealed significant UPOs.

3.2 Brain dynamics

The electroencephalograph (EEG) measures the temporal and spatial fluctuations in the electric field arising from the electrical activity of large populations of neurons in the brain. The EEG has been in use for decades and yet remains the tool of choice for most neuroscientists seeking to study brain activity. Thus it should come as no surprise that the EEG is favoured by neuroscientists interested in the possibility of nonlinear deterministic dynamics in the electrical activity of the brain.

One of the earlier attempts to search for deterministic dynamics in the EEG was made by Babloyantz et al. (1985) [23]. They investigated the dynamics of brain activity during the sleep cycle by calculating the pointwise correlation dimension for time series taken from EEG recordings of sleep stages two and four (deep sleep) as well as during REM sleep. They report measuring correlation dimensions for both stage two sleep ($D_2 = 5.03 \pm 0.07$ and $D_2 = 4.99 \pm 0.11$) and stage four sleep ($D_2 = 4.05 \pm 0.5$, $D_2 = 4.08 \pm 0.05$ and $D_2 = 4.37 \pm 0.1$). They conclude that they have provided convincing evidence for chaotic, deterministic dynamics in the brain during sleep.

More recently, Cerf et al. (1997) [24] applied the method of *surrogate data* to the

---

[1]UPOs are an indication of deterministic dynamics

calculation of the correlation dimension during EEG recordings of unusually long episodes of cortical α-rhythms. They found that while EEG recording of more than a minute did not yield evidence for low-dimensional dynamics, there was evidence for low-dimensional α-dynamics lasting for up to 10 seconds. Cerf et al. suggest that their results indicate that the model of an autonomous dynamic system in steady state is an inappropriate description of brain dynamics as recorded from the EEG. They hypothesize that the dynamics are ruled by a *shadow-attractor* where episodes of attractor-ruled dynamics fade smoothly in and out with time. They also propose that enslaving and escaping a time-dependent number of neural sub-systems could be the the mechanism behind the appearance of the *shadow-attractor*.

Freeman and his colleagues are investigating the dynamics of the activity present in the rabbit olfactory system [25] [26]. He has developed a rather complex computer model which closely emulates the EEG recording from the olfactory bulb and the prepyriform cortex of the rabbit, both in autonomous activity and under the influence of certain stimuli. Mathematical analysis of the model reveals that it is chaotic in the true sense described in section 2.1. Through his research, Freeman has accumulated evidence in support of a theory regarding the function of chaotic dynamics. He reports that when the rabbit is stimulated with a familiar odour, the normally high-dimensional chaotic activity suddenly bursts in a regularized pattern. The transition is abrupt, akin to a phase transition in a physical system. Under the same conditions. the computer model also experiences an abrupt transition into a regularized mode of the chaotic dynamics reflected in a lower correlation dimension than that measured in the nonstimulated system.

Several researchers, including Kelso et al. [27], have chosen to use superconducting quantum interference devices (SQUIDs). Like the EEG, SQUIDs use a collection of sensors distributed over the surface of the brain or scalp; however, unlike the EEG which measures electric fields, SQUID sensors measure the small magnetic fields generated by neuronal activity. Kelso et al. used 37 SQUIDs to record the neuronally generated magnetic fields over the left parieto-temporal cortex of a human subject while the subject performed cognitive tasks. They found that there was a clear chaotic attractor visible in the state space reconstruction of the SQUID recordings and similar to the results of Freeman, Kelso et al. noticed that the dynamics changed suddenly in response to changes in the environment. Kelso et al. suggest that the changes in brain dynamics resemble those present in Šil'nikov chaos [27] where a

change in a system parameter qualitatively changes the shape of the chaotic attractor.

The literature regarding the dynamics of brain activity presented in this section point to a couple of intriguing possibilities. First, there is substantial evidence for chaotic dynamics in the normal operations of the mammalian brain. Second, the research, particularly that of Freeman and Kelso et al., points to the possibility that the natural state of brain dynamics exists as a critically unstable system capable of both spontaneous and provoked transitions to qualitatively different behaviours such as regularization.

3.3   Brain Chaos and Epilepsy

A central assumption of this thesis, stated in the introductory chapter, section 1.5, is that epileptic seizures correspond to instances of increased rhythmicity and reduced complexity in neuronal activity [28] [29]. In this section we present a brief summary of the experimental evidence in support of this theory of epilepsy.

One of the earliest and best known investigations into the dynamics of epileptic activity was done by Babloyantz et al. (1986) [30]. Studying EEG recordings of a human *petit mal* epileptic seizure, They found that the there was an attractor apparent in the state space reconstruction of the time series. In addition, they measured a correlation dimension of $D_2 = 2.05 \pm 0.09$, significantly lower than what the same group measured during the sleep cycle of healthy brain activity[23].

The correlation dimension reflects the complexity of the system producing the time series by measuring the degrees of freedom inherent in the system. The more degrees of freedom available to the dynamics of a system, the greater will be the system complexity. Thus the result of Babloyantz et al. [30] provides evidence in favour of the theory that epilepsy corresponds to system activity of lowered complexity in comparison with healthy neuronal activity.

In 1991, Pijn et al. [14] were among the first to apply the method of *surrogate data* in the investigation of epileptic seizure dynamics as measured from the EEG. They computed the correlation dimension of EEG signals recorded from different sites of the limbic cortex of the rat during a number of different states. These states consisted of wakeful rest, locomotion and an epileptic seizure state induced by kindling. They used the method of *surrogate data*

33

to determine whether the EEG signals are deterministic in the sense of being distinguishable from noise with the same power spectra. Pijn et al. [14] found that the correlation dimension during wakeful rest and locomotion were high and could not be distinguished from random noise. In contrast, the EEG signal corresponding to the epileptic seizure were of significantly lower dimension ($D_2 = 2$ to $D_2 = 4$) than the other two states and were distinguishable from the surrogate version of the signals.

Casdagli et al. (1997) [31] searched for evidence of nonlinear dynamics in the EEG recordings from two patients with temporal lobe epilepsy. EEG recordings of seizure activity were taken from bilateral depth and subdural electrodes and analyzed with the method of *surrogate data* to compute the correlation integral. The correlation integral represents the probability that two vectors chosen at random lie within a small distance of each other. Generally, a less random time series will have a larger correlation integral. For regions of the brain known to be involved in the epileptic seizure, Casdagli et al. computed correlation integrals which were distinguishable from the surrogate data. This result indicates the presence of deterministic "nonlinearities" present in the epileptic activity. Regarding regions of the brain which were not thought to be involved in the epileptic activity, They reported that "less prominent nonlinearities were present". They arrived at this conclusion by noting that there was less of a distinction between the correlation integral computed from these signals and their respective surrogate signals.

Also in 1997, Le Van Quyen et al. [32] published an article on their analysis of a subdural EEG signal from a patient with an epileptic focal seizure. The focal seizure was unusual in the ongoing nature of the discharges and in the absence of cognitive impairment. Using the method of false nearest neighbours [2], they established that the EEG signal is well represented in a state space of four dimensions. Le Van Quyen et al. implemented the periodic orbit transform, developed by So et al. [22] and [21], and the method of *surrogate data* to establish the presence of unstable periodic orbits (UPOs).

Le Van Quyen et al. [32] also used the EEG to record the electrical activity of the subject while performing visual and audio discrimination tasks during the ongoing epileptic focal

---

[2]The method of false nearest neighbours involves increasing the dimension of the reconstructed attractor until there is no longer any large changes in the distances between nearest neighbours of the trajectory vectors.

seizure. In agreement with the results of Freeman [26], Le Van Quyen et al. observed that the reconstructed EEG signal trajectories approached particular periodic orbits immediately following the perceptual tasks.

The analysis of Le Van Quyen regarding the presence of UPOs in epileptiform activity is supported by So et al. [20] who used the same transformation technique to demonstrate the presence of UPOs in human cortical EEG recordings taken in the hour before the onset of the seizure. So et al. found that 2 of the 4 epileptic patients' interictal spike sequences showed statistically significant period-1 UPOs.

Velazquez et al. [33] have recently found evidence for intermittency in human partial epilepsy. They constructed a histogram of the duration of the rhythmic phases and found the shape of the distribution to be characteristic of type III intermittency. Intermittency arises in system with one or more UPOs which are nearly stable.

Chapter 4

Literature Review II:
Chaos Control Techniques

In this chapter, we present a review of the literature regarding the application of chaos theory to controlling systems. We begin by describing the techniques which have been developed over the past ten years. Then we discuss the recent attempts to apply the chaos control strategies to biological systems and finally to the neuronal tissue.

4.1 Controlling Chaos

In 1990, Ott, Grebogi and Yorke (OGY) introduced the concept of controlling chaos [34]. They noted that a chaotic attractor can be thought of as being made up of an infinite number of unstable periodic orbits (UPOs). From this perspective a trajectory moving on the chaotic attractor would slip from one UPO to another. The amount of time spent near a UPO is inversely related to its degree of instability. The movement of trajectories between the UPOs manifests itself in the output as the observed aperiodicity characteristic of chaos.

Following the example of Ott et al., we introduce the concept of controlling chaos through an application to a general 2-dimensional system. Consider the map,

$$x_{n+1} = f(x_n, p_n),$$ (4.1)

where $x^T = [\ x_1 \quad x_2\ ]$ forms a two dimensional state space and p_n is a system parameter which may be adjusted at each time step. This map has a fixed point at x_F which, at each

36

time step, is dependent on the value of p_n. The dependence of x on p_n may be estimated for small perturbations to p_n away from some nominal value of the parameter, p_0 by the linearized equation,

$$\hat{x}_F(p_n) = x_F(p_0) + (p_n - p_0)s^h, \tag{4.2}$$

where s^h is the *shift vector*, [35], and is defined as,

$$s^h \equiv \frac{d}{dp} x_F(p)\,|_{p=p_0} \tag{4.3}$$

Linearizing the map in 4.1 in the neighbourhood of x_F, we get

$$\hat{x}_{n+1} = x_F + M(\hat{x}_n - x_F). \tag{4.4}$$

In chaotic systems, there always exists a saddle point. If we assume x_F to be such a saddle point then the matrix M has one stable eigenvector, e_s, and one unstable eigenvector, e_u. The eigenvectors e_s and e_u have eigenvalues λ_s and λ_u respectively. Let us define a new basis vector set $\{f_s, f_u\}$ such that $f_s^T e_s = f_u^T e_u = 1$ and $f_u^T e_s = f_s^T e_u = 0$.

If we shift the fixed point, $x_F(p_0) \mapsto x_F(p_n)$, just before applying the mapping, $x_n \mapsto x_{n+1}$, then we may approximate the mapping close to the fixed point as

$$(\hat{x}_{n+1} - \hat{x}_F(p_n)) = M(\hat{x}_n - \hat{x}_F(p_n)). \tag{4.5}$$

Combining equations 4.2 and 4.5, we get

$$\hat{x}_{n+1} - x_F(p_0) - (p_n - p_0)s^h = M(\hat{x}_n - x_F(p_0) - (p_n - p_0)s^h). \tag{4.6}$$

We are interested in the component of 4.6 in the direction, f_u, orthogonal to the stable eigenvector of M. Taking the projection of 4.6 on f_u results in

$$f_u^T(\hat{x}_{n+1} - x_F(p_0) - (p_n - p_0)s^h) = \lambda_u f_u^T(\hat{x}_n - x_F(p_0) - (p_n - p_0)s^h). \tag{4.7}$$

Let $\delta p_n \equiv p_n - p_0$ and $\delta x_n \equiv \hat{x} - x_F(p_n)$. Now we are ready to determine what δp_n should be to ensure that we stay close to x_F. If we force $\hat{x}_{n+1} = x_F(p_0)$ along the f_u direction, then we get the formula of Ott, Grebogi and Yorke [34]:

$$\delta p_n = \frac{\lambda_u}{\lambda_u - 1} \frac{f_u^T \delta x_n}{f_u^T s^h}. \tag{4.8}$$

37

The development of this equation was based on a two dimensional discrete-time system with a saddle point. This is not as restrictive as it may appear. The map $x_n \mapsto x_{n+1}$ could be the evolution of a continuous time chaotic system as observed from a Poincaré section. If we take every second or third Poincaré section, then the corresponding period-2 or period-3 UPOs would appear as saddle points. From this perspective, there is a great variety of UPOs which may be stabilized by the OGY method.

Subsequent to the original work of Ott, Grebogi and Yorke [34], there has been numerous extensions of the OGY method to higher dimensions, [36], [37], [38] and [39]. Grebogi et al. [39] generalized the OGY method to any size system and demonstrated that it is a particular case of the pole placement technique known to system control experts. They argue that it is optimal in the sense that it is the pole placement with the fastest decay of the transient.

Ditto et al. [40] gave the first experimental demonstration of the OGY control of chaos technique. They were able to stabilize period-1 and period-2 orbits in the chaotically oscillating magnetoelastic ribbon through small changes to the vertical direct current (dc) magnetic field. An impressive result of this work was that control was achieved without the need for explicit equations of motion. The linearized mapping M and shift vector s^h were estimated from the time series before the control action was applied. Hunt [41] showed that through a modification of the OGY method high-period orbits in experimental systems were able to be stabilized. In a diode resonator, he was able to stabilize as high as a period-87 orbit [35].

4.2 Targeting

Concurrent to the development of the OGY control of chaos technique to stabilize UPOs, Shinbrot et al. [42] [43] [44] explored the possibility of using the sensitive dependence on initial conditions (SDIC) characteristic of chaos to allow one to target specific regions of a chaotic attractor in state space. They demonstrated that, by making small changes to a system parameter, they were able to deliberately steer trajectories of chaotic systems to desired target regions [44]. The targeting strategy of Shinbrot et al. is heavily dependent on having an equation representing the system under control.

Targeting is performed by a numerical algorithm which iterates the equations of the chaotic system both forwards from the starting point and backwards from the target region. Intersections of these two iterates determine the parameter adjustments required to send the chaotic system to the target region of state space.

Similar to our development of the OGY control of chaos technique, we shall begin with the map,

$$x_{n+1} = f(x_n, p), \qquad (4.9)$$

where $x^T = [\ x_1 \quad x_2 \quad \dots \quad x_N\ ]$ forms an N-dimensional vector and p is an adjustable system parameter.

Let the parameter p be nominally at some value p_0 and it can be perturbed away from p_0 by an amount $\delta p = p - p_0$ where we restrict δp to the range $-\Delta p \leq \delta p \leq \Delta p$. The quantity Δp is the maximum allowed size of the perturbation.

The equations of motion are iterated once from the starting point of the targeting algorithm, x_S, for a population of values for δp distributed throughout the range $-\Delta p \leq \delta p \leq \Delta p$. A variation in the the state vector, x_1, results from the mapping $x_S \mapsto x_1$ though the various values of δp. If the parameter perturbations are small the variation in x_1 is given by.

$$\delta x_1 = \left. \frac{\partial f}{\partial p} \right|_{(p_0, x_S)} \delta p. \qquad (4.10)$$

After the initial parameter perturbation, the parameter is typically returned to its nominal value of p_0. The population of iterations x_1 form an interval, Δx defined by equation 4.10 and the limiting values of δp, $\pm \Delta p$. In a chaotic system, this interval will typically grow exponentially with each successive iteration. For example, in the subsequent mapping $x_1 \mapsto x_2$, the interval $\Delta x_2 = e^{\bar{\lambda}_u} \Delta x_1$, where on average $\bar{\lambda}_u > 0$. These iterations continue until the interval Δx_n is about the size of the attractor.

The next step in the targeting algorithm is similar to the first, though done in reverse. A second population of points is placed within an ϵ-neighbourhood of the target vector, x_T. The value of ϵ is determined by the tolerance on how close one must come to the target vector. These points are iterated backwards in time at the nominal parameter value, p_0 [44]. Just as forward iterations evolve along the unstable manifold, backwards iterations evolve along

39

the stable manifold. Thus the second population of points evolve along the stable manifold of the target point, x_T. The length of the surface or curve, formed by the population of points evolving backwards in time, grows exponentially in time at a rate proportional to the most negative Lyapunov exponent measured in forward time. Once again, the population of points is evolved until the size of the surface they form is on the order of the size of the attractor.

Finally, the two populations of points are compared and searched for intersections. Typically the manifolds formed by the two population of points do intersect, meaning that points from the two populations will lie within some ϵ-neighbourhood of each other. When an intersection is found, the values of the parameter perturbations which correspond to the points intersecting with the stable manifold, δp^* are determined. Perturbing the paramenter by δp^* at x_S steers the trajectory onto the stable manifold of the target point x_T. Once on the stable manifold, the trajectory is drawn to the x_T through the dynamics of the system and without any further control energy.

There are a number of limitations of the targeting technique of Shinbrot *et al.* which are of relevance to us. By steering the trajectory on the stable manifold of x_T we are relying on the system to take the trajectory to the target region through the action of the stable manifold. If the trajectory is not exactly on the stable manifold then the action of the unstable manifold will tend to force the trajectory away from the stable manifold. The attempt is analogous to trying to roll a ball down from the top of a saddle to reach the middle. If the ball is a little off of the center line then the slope will tend to lead the ball away from the middle and down one side. The presence of noise and the finite accuracy of any measure ensures that we can never steer the trajectory exactly on the stable manifold. Therefore, it becomes an issue of how fast the trajectory is diverging from the stable manifold. If the trajectory reaches the target region before significant exponential growth of any discrepancy between the trajectory path and the stable manifold, then the technique is feasible. Otherwise, an improvement suggested by Kostelich *et al.* [45] to provide multiple parameter perturbations may be able to act against the instability of the stable manifold of the target region.

The limited applicability to higher dimensions constitutes a second limitation of targeting. In higher dimensions the target region becomes an increasingly smaller area of the

searchable space. The number of iterations between the starting point and the final target region may be prohibitive. Kostelich *et al.* [45] have proposed increasing the effective area of the target region by pre-computing a tree of paths to the target. The tree could be constructed using reverse time iterations or, in the case of an experimental system, by observing the system and noting which areas of the attractor tend to evolve to the target region. Once the tree is constructed, the targeting problem is reduced to targeting any of the branches of the tree of regions leading to the target, effectively increasing the target area.

The final limitation of targeting which we shall consider is the large computational burden of iterating a large number of vectors required to cover an attractor in higher dimensions. The suggestions proposed by Kostelich *et al.* provide a streamlined procedure for targeting in higher dimensions. Precomputing a tree of paths to the target region and allowing multiple parameter perturbations reduces the number of iterations required to find a path to the target.

4.3   Control of Chaos in Biological Systems

The control of chaos technique of Ott, Grebogi and Yorke [34] only requires that the local dynamics to some fixed point be known. When these local dynamics are able to be modeled by linear eigenvectors, the dynamics may be easily estimated from the time series alone. The removal of the requirement for an accurate model of the system opens the door to controlling biological systems.

In 1992, an early attempt to control chaos in a biological system was made by Garfinkel *et al.* [46]. They applied the OGY method to stabilized periodic orbits in an in vitro model of cardiac arrhythmia. As a model they used the interventricular septum of a rabbit heart exposed to a toxic concentration of the cardiac glycoside ouabain to induce intracellular Calcium (Ca^{2+}) overload. Rather than perturbing a system parameter to change the position of the fixed point, they perturbed the system variable to position it on the stable manifold of the fixed point. The system variable they chose was the interspike interval between cardiac action potentials. Perturbations of the variable consisted of eliciting an action potential, through stimulation, at the appropriate time. Chaos control of the ouabain-induced ventricular tachycardia was successful in stabilizing period-2, period-3 and period-4 patterns in the

41

interspike interval (I) time series [47].

Hall *et al.* [48] also made efforts to control the dynamics of cardiac tissue. They applied their control algorithm to control cardiac alternans rhythm in the rabbit heart. Their control algorithm is a much simplified form of the modified OGY method implemented by Garfinkel *et al.* [48]. They assume the dynamics are governed by a flip-saddle fixed point. The simplification eliminates the need for the learning phase required by the method implemented by Garfinkel *et al.* The algorithm of Hall *et al.* adaptively estimates the fixed point as

$$x_F = \frac{1}{2}(x_n + x_{n-1}).$$ (4.11)

The algorithm is able to adapt to nonstationarities of the location of the fixed point location. This feature makes the algorithm potentially well suited to controlling physiological systems which are known to change over time.

In 1997, Christini *et al.* [49] introduced an alternative to the OGY method to control chaos in excitable physiological systems. In the development of their stable manifold placement (SMP) algorithm, they recognized that in the first return map, plotted as x_n versus x_{n-1}, the stable eigenvector is entirely given by the location of the fixed point, x_F, and by the stable eigenvalue, λ_s. The SMP algorithm determines the intervention time as

$$x_{n+1} = \lambda_s(x_n - x_F) + x_F.$$ (4.12)

The SMP technique is limited to the local linear region of fixed points in systems which can be described in two dimensions [1]. The advantage of the SMP technique is the reduced number of estimations required for successful control. The OGY method requires that the complete local linear dynamics in the region of the fixed point be known, whereas the SMP algorithm requires knowledge of only the stable eigenvector.

In addition to the presentation of the SMP algorithm, Christini *et al.* raise some important issues regarding the application of dynamic control strategies to excitable physiological systems [49]. The first question is whether excitable physiological systems are actually characterized by UPOs with one stable manifold and one unstable manifold, as has been assumed in the physiological applications of the variants on the OGY method including the

---

[1]Physiological systems have been controlled from similar two dimensional representations, [46] and [1]

SMP technique [46], [48], [49] and [1]. A second issue raised by Christini *et al.* is whether the control stimulus significantly modifies the UPO dynamics rather than simply placing the state point onto the stable manifold. A pervasive assumption in this area of research is that stimulation has no residual effects and that the state point responds as if it arrived on the stable manifold naturally. Although a suprathreshold stimulus may be a small perturbation to the interspike interval variable I, the stimulus is a large perturbation to the physiological system dynamics. Christini *et al.* suggest that further investigation is necessary to clarify whether or not the system dynamics will return to those of the autonomous system immediately after the stimulation.

Christini *et al.* also suggest that from a physiological perspective a desirable goal is the minimization of intervention by the control algorithm. They suggest that since the perturbation size is fixed by the requirement to be suprathreshold, the emphasis should be placed on reducing the frequency of stimulation [49].

All of the applications of dynamic control in physiological systems described above use an interspike interval, I_n, state space reconstruction. The control action attempts to force the state point toward the UPO by placing it directly onto the stable manifold. This goal is accomplished by inducing premature action potentials through suprathreshold electrical stimulation. As a result of the type of stimulation commonly employed in these systems, the control stimuli cannot lengthen I_n it can only shorten it.

The dynamic control strategies described above have the goal of stabilizing a particular UPO within a naturally chaotic system. Yang *et al.* [50] offer a different perspective on the subject of chaos and biology. They suggest, as we do, that in a wide variety of biological systems, chaos is the natural and preferred system behaviour. In [50], Yang *et al.* present a control strategy to preserve chaotic dynamics in systems which, in the absence of intervention, would become periodic as a result of a drift of a system parameter. Their strategy is to perturb the system back to a chaotic mode when a system parameter, p, drifts into periodicity, for $p > p_c$. The perturbation is designed to steer the trajectory out of the path to the loss region, L, defined such that after the system falls in L, it is rapidly drawn to the periodic orbit. The approach is to compute successive preiterates of L,

$$L_m = f^{-1}(L_{m-1}, p) = f^{-m}(L, p), \tag{4.13}$$

43

such that L_m is the set of points that map to the loss region, L in m iterates. As m increases, the width of L_m in the unstable direction will typically shrink exponentially and consequently the size of the control perturbation to place the system outside the path to L shrinks. Yang *et al.* demonstrated the preservation of chaos in low dimensional numerical models. They used the dynamic equations to compute the preiterates and the size of the appropriate control action.

4.4 Control of Chaos in the Brain

In 1994, Schiff *et al.* applied a modified OGY control of chaos technique to a high $[K^+]$ model of epilepsy in a rat hippocampus slice preparation [1]. It is believed to be the first attempt to employ such a technique to control the electrical activity of brain tissue. Their approach was similar to the technique employed by Garfinkel *et al.* [46] to control chaos in rabbit heart tissue. Glass microelectrodes in the CA1 and CA3 regions of the hippocampus were used to record neuronal electrical activity. A computer algorithm received the electrical activity time series and performed an action potential detection in real time. The algorithm reconstructs a two dimensional interspike interval state space, then searches for candidate unstable fixed points to be stabilized. The candidates were required to meet four criteria: 1) A sequence of points must approach the unstable fixed point candidate along the stable direction and diverge from it along an unstable direction. 2) The departing trajectory must be linear within some neighbourhood of the fixed point candidate. 3) Multiple approaches along the same stable direction with corresponding departures along the same unstable direction must be detected. 4) The departing trajectory must diverge exponentially from the the fixed point candidate. This final criteria exists to ensure that the trajectories exhibit SDIC, a hallmark of chaos as was previously discussed.

The chaos control strategy of Schiff *et al.* begins with a learning phase in which the unstable fixed points are identified and linear approximations of the local stable and unstable manifolds are determined by least-square linear regression of the approaching and departing trajectories. The control phase consists of waiting until a trajectory approaches the identified unstable fixed point (within a small radius ϵ) along the stable direction. At which time an intervention stimulus is given which modifies the timing of the next action

44

potential in order to place x_n back onto the stable manifold. As is the common strategy of all OGY-type chaos control techniques in two dimensions, Schiff *et al.* use saddle point dynamics to hold the system close to the unstable fixed point.

In an effort to decrease the periodicity of the neuronal electrical activity, Schiff *et al.* implemented what they term *anticontrol*. This was achieved by chosing an intervention stimuli which placed I_{n+1} on a line completely off the manifolds. They somewhat arbitrarily chose to place the trajectories on the mirror image of the unstable manifold about the line of identity, $I_{n-1} = I_n$.

Schiff *et al.* achieved moderate success at controlling and anticontrolling the neuronal electrical activity. They report roughly half of their attempts at stabilizing an unstable fixed point as being successful. *Anticontrol* achieved less success with approximately a quarter of the attempts resulting in what they determine to be a success.

In their discussion, they state:

> "The observation of small-scale structure and the identification of stable and unstable manifolds near unstable fixed points for many of these burst-firing slices demonstrated the presence of deterministic chaos in this simple neuronal system [1]."

With regard to the application of chaos control techniques to epilepsy therapies, they suggest that since the neuronal preparation used in their experiment shares similar characteristics with epileptic interictal spike foci, that perhaps these methods may be applied to such foci. They also offer,

> "Although it is impossible to predict what effect increasing the periodicity of epileptic foci will have, the opposite effect of breaking up fixed-point periodic behaviour with anticontrol could be a more useful intervention.[1]."

Since the 1994 publication of [1] in Nature, the effort to apply chaos control techniques to brain tissue has focused on developing more robust methods to identify unstable periodic orbits [22].

In response to the claims of Schiff *et al.* [1], with respect to their demonstration of deterministic chaos, Christini *et al.* [51] applied the modified-OGY chaos control method to

a nonchaotic neuronal model. The neuronal model was a stochastically driven version of the FitzHugh-Nagumo model as given by,

$$\epsilon \dot{v} = v(v - 0.5)(1 - v) - w + V_A + \xi(t),$$ (4.14)

$$\dot{w} = v - w - 0.15,$$ (4.15)

where $v(t)$ is the voltage variable, $w(t)$ is the recovery variable, V_A represents a tonic activation of 0.2 V, $\xi(t)$ is a Gaussian random variable with zero mean and standard deviation $= 6.325 \times 10^{-4}$ V and $\epsilon = 0.005$.

Christini *et al.* constructed an interspike interval first return map and applied the same criteria as Schiff *et al.* for the identification of unstable fixed points. They found that occasionally there existed sequences of points which satisfied all four criteria of Schiff *et al.* and a location of an *apparent* unstable fixed point could be found, when, in fact, there are no unstable fixed points in the equations 4.14 and 4.15. Furthermore, They demonstrated that the application of the modified OGY chaos control strategy to the stochastic system resulted in stablizations of the *apparent* fixed points.

Chapter 5

Modelling Chaos with RBFs

This chapter is concerned with the problem of capturing the dynamics of a chaotic system from the time series. We begin with a discussion of the available time series models and argue that Radial Basis Function (RBF) models are well suited for modelling chaotic dynamics. Next, the details of the RBF model and the learning algorithms are presented. We conclude with the application of the RBF model to learning the chaotic dynamics of the two subject systems, the Henon map and the MCO model.

5.1 Time Series Modelling

In our attempt to maintain chaotic activity in a system which drifts into rhythmicity, we must begin by developing some sort of model of the system behaviour. The function of the model is twofold. First, we require some quantification of the healthy behaviour of the chaotic system to facilitate detection of a transition to a more rhythmic activity. Second, the model is to provide a description of the attractor of the chaotic system to facilitate the action of a control strategy to reintroduce the chaotic activity. Whatever model is used, the model parameters must be able to be completely determined from a time series of a measured system variable. In the case of the neuronal network, the system variable could be the the interspike interval of the transmembrane voltage of one of the neurons in the network.

The requirement that the model should be identified from a time series rests on two important observations:

1. Neuronal networks are dynamic and highly plastic in nature. The dynamics of these networks will change significantly over time. The time series would reflect the changing dynamics, thus the possibility exists to incorporate the plasticity of the network in the time series based model.

2. The observed dynamics will be a function of the position of the points of measurement and the connections between the large number of neurons in the population. If we were to attempt to construct a detailed model of the neural organization, we would require knowledge of all the interactions between neurons as well as where the electrode would be placed. The complexity of such a model is beyond the horizon of current modelling techniques. Nevertheless the time series measured from complex neuronal networks often displays deterministic characteristics at relatively low dimensions of the state space reconstruction [23]. Herein lies the potential of time series modelling techniques. If the multitude of neurons in the neuronal assembly work together to support activity of relatively low dimension, then the possibility exists that a model, of relatively few degrees of freedom, would be able to capture the dynamics.

Once we have decided on the use of a time series based model, we must consider which of the multitude of models is best for our application. Our goal is to develop a model of chaotic dynamics capturing both the local instability and global boundedness of the chaotic attractor. The type of model we choose must be capable of capturing these fundamentally nonlinear characteristics of the system without requiring excessive amounts of data in the learning process. Kantz *et al.* [4] reviewed a number of time series based models on their ability to capture chaotic dynamics. The models they reviewed include artificial neural networks, RBF models, locally linear models, locally constant models, polynomial models, and autoregressive (AR) models. They trained each on a time series and evaluated the performance of each model by comparing the one step prediction errors on a test set which was not included in the training set. Kantz *et al.* found that the locally linear, polynomial and RBF models gave the best performance of one step prediction.

The locally linear model fits a nonlinear attractor through a collection of linear neighbourhoods. If a neighbourhood is large compared to the inverse curvature of the true surface, then the approximation will be poor [4]. it follows that, in order to ensure a good fit with

a locally linear model, we require many small neighbourhoods in regions of significant curvature. This requires a large amount of data. Thus the locally linear model does not seem appropriate for our application.

The polynomial model may be regarded as a effort to fit the parameters of a truncated Taylor series expansion to the time series. The polynomial model is capable of capturing nonlinearities without excessive numbers of data points. A problem arises, however, when we consider that polynomial basis functions diverge for large arguments [4]. Our control strategy will require recurrent iterations of the time series model. With polynomial basis functions, small errors in the recurrent iterations would tend to compound and result in unbounded outputs. In these situations, the polynomial model would cease to be an adequate model of the chaotic dynamics.

The RBF model is capable of modelling nonlinear dynamics with a reasonable number of points. The form of the model we will be considering is guaranteed to be bounded for all finite values of its parameters [52]. RBF models have been demonstrated to be endowed with the universal approximation capability [53] implying the possibility of approximating a function to any degree of accuracy. A final aspect of RBF models that make them appealing for modelling dynamical systems is that, unlike other artificial neural networks they are naturally representable in the state space of the system being modelled. Model visualization aids in their development by allowing for the correlation of model characteristics with performance.

The RBF model has been applied to model the dynamics of well known chaotic systems such as the Lorenz differential equations [54] and the Mackey-Glass delay-differential equations [55]. It has also been applied to chaotic NMR laser data [4].

5.2   The RBF Model

The radial basis function model (RBF) expresses an output, y_n, as a linear expansion along radial functions of an input vector x_n, as given by

$$y_n = \sum_{i=0}^{N} w_i \phi_i(x_n),$$

(5.1)

49

where $\phi_i(x_n)$ is the activity of the ith radial basis function given the input, x_n. The term w_i represents the expansion coefficient of the ith RBF. There are a number of different radial basis functions used in RBF models, we have chosen the Gaussian functions as our radial basis functions because of extensive literature regarding the Gaussian functions as RBFs. The Gaussian RBFs are expressed as,

$$\phi_i(x_n) = \exp\left(-\frac{\|x_n - \mu_i\|^2}{2\sigma_i^2}\right),$$ (5.2)

where $\mu_i = [\ \mu_{i1}\ \ \mu_{i2}\ \cdots\ \mu_{im}\ ]$ is a vector representing the mean or center of the ith Gaussian function in an m dimensional state space. The variance of the ith Gaussian function is given by σ_i^2. The $i = 0$ basis function is given by a vector of ones and together with the coefficient, w_0 represents the mean of the time series.

In our application, we are interested in predicting x_{n+1}, the next iterate of the dynamic system, based on a vector of previous iterates, x_n. In an m-dimensional subject system, $\mathcal{F}$, x_n is an m-dimensional delay coordinate vector, $x_n = [\ x_{n-(m-1)}\ \cdots\ x_{n-1}\ x_n\ ]$. Thus our RBF model is given by the equation,

$$\hat{x}_{n+1} = \sum_{i=0}^{N} w_i \phi_i(x_n),$$ (5.3)

where $\hat{x}_{n+1}$ is the output of the RBF model at time n and represents the estimate of the x_{n+1}, the next iterate of $\mathcal{F}$.

5.3 Parameter Estimation

In order for the RBF model to predict the activity of the subject system, $\mathcal{F}$, we must first estimate appropriate values for the model parameters, μ_i, σ_i and the coefficients, w_i. Parameter estimation is accomplished through an iterative process where the parameters are chosen to minimize an error function reflecting the difference between the RBF model prediction, $\hat{x}_{n+1}$ and the next iterate of $\mathcal{F}$, x_{n+1}, over a training set of data formed from a time series of duration D. The typical error function is the sum-of-squares error function given by

$$E = \frac{1}{2} \sum_{n=m}^{D-1} \{\hat{x}_{n+1} - x_{n+1}\}^2$$ (5.4)

50

One of the aspects of RBF models which makes them more desirable than models such as the multilayered perceptron network is that RBF models are linear in the expansion coefficients, w_i. Thus we may employ fast linear optimization techniques to determine their values. The result is a two step learning process where the parameters w_i are determined by linear optimization, followed by a iteration of a nonlinear gradient descent algorithm to update the values of μ_i and σ_i. The process is re–iterated for a number of epochs, with the parameters w_i evolving at a fast time scale (within a single epoch), and the parameters μ_i and σ_i evolving at a slow time scale (over a number of epochs).

5.3.1 Estimating w_i

If we substitute equation 5.3 into equation 5.4 and set the derivative with respect to w_i to zero we get an expression describing the minimum of the error function, E, with respect to w_i.

$$\frac{\partial E}{\partial w_i} = \sum_{n=m}^{D-1} \left(\sum_{j=0}^{N} w_j \phi_j(\boldsymbol{x}_n) - x_{n+1} \right) \phi_i(\boldsymbol{x}_n) = 0. \tag{5.5}$$

Converting equation 5.5 to matrix notation we get,

$$\boldsymbol{\Phi}^T \boldsymbol{\Phi} \boldsymbol{w}^T = \boldsymbol{\Phi}^T \boldsymbol{x}_T, \tag{5.6}$$

where $\boldsymbol{w} = \left[\begin{array}{cccc} w_0 & w_1 & \cdots & w_N \end{array} \right]$ and $\boldsymbol{x}_T = \left[\begin{array}{cccc} x_{m+1} & x_{m+2} & \cdots & x_D \end{array} \right]^T$ is the vector of target values of the prediction on the data set. The matrix $\boldsymbol{\Phi}$ is give by

$$\boldsymbol{\Phi} = \begin{bmatrix} 1 & \phi_1(\boldsymbol{x}_m) & \phi_2(\boldsymbol{x}_m) & \cdots & \phi_N(\boldsymbol{x}_m) \\ 1 & \phi_1(\boldsymbol{x}_{m+1}) & \phi_2(\boldsymbol{x}_{m+1}) & \cdots & \phi_N(\boldsymbol{x}_{m+1}) \\ \vdots & \vdots & \vdots & \ddots & \vdots \\ 1 & \phi_1(\boldsymbol{x}_{D-1}) & \phi_2(\boldsymbol{x}_{D-1}) & \cdots & \phi_N(\boldsymbol{x}_{D-1}) \end{bmatrix} \tag{5.7}$$

We are interested in solving this linear system of equations, 5.6, for the unknown $\boldsymbol{w}$. Taking the inverse we arrive at,

$$\boldsymbol{w} = (\boldsymbol{\Phi}^T \boldsymbol{\Phi})^{-1} \boldsymbol{\Phi}^T \boldsymbol{x}_{n+1}. \tag{5.8}$$

The inverse, $(\boldsymbol{\Phi}^T \boldsymbol{\Phi})^{-1}$, is taken using singular value decomposition (SVD) to avoid problems due to potential ill-conditioning of the matrix [56]. [1]

---

[1]In SVD, we use an allowable range of 1×10^6 for the singular values.

5.3.2 Determining μ_i and σ_i

The parameters μ_i and σ_i are optimized by a gradient descent method. Differentiating the error function, E, given in equation 5.4 with respect to the basis function parameters, μ_i and σ_i, we obtain

$$\frac{\partial E}{\partial \sigma_i} = \sum_{n=1}^{D} \{\hat{x}_{n+1} - x_{n+1}\} w_j \exp\left(-\frac{\|\boldsymbol{x}_n - \boldsymbol{\mu}_i\|^2}{2\sigma_i^2}\right) \frac{\|\boldsymbol{x}_n - \boldsymbol{\mu}_i\|^2}{\sigma_i^3}, \tag{5.9}$$

$$\frac{\partial E}{\partial \mu_{ij}} = \sum_{n=1}^{D} \{\hat{x}_{n+1} - x_{n+1}\} w_j \exp\left(-\frac{\|\boldsymbol{x}_n - \boldsymbol{\mu}_i\|^2}{2\sigma_i^2}\right) \frac{(x_{n-(m-j)} - \mu_{ij})}{\sigma_i^3}, \tag{5.10}$$

where μ_{ij} denotes the jth component of $\boldsymbol{\mu}_i$.

The path down the error surface in the directions indicated by the gradients of E with respect to σ_i and μ_{ij} proceeds in discrete steps. These steps are given by the equations,

$$\Delta \sigma_i(t) = -\epsilon \epsilon_{\sigma_i}(t) \frac{\partial E}{\partial \sigma_i}(t) + \alpha \Delta \sigma_i(t-1), \tag{5.11}$$

$$\Delta \mu_{ij}(t) = -\epsilon \epsilon_{\mu_{ij}}(t) \frac{\partial E}{\partial \mu_{ij}}(t) + \alpha \Delta \mu_{ij}(t-1), \tag{5.12}$$

where ϵ is the learning rate constant, t represents time in epochs and $\epsilon_q(t)$ is an adaptive gain on the learning rate for either q $= \sigma_i$ or q $= \mu_{ij}$. The terms $\alpha \Delta \sigma_i(t-1)$ and $\alpha \Delta \mu_{ij}(t-1)$ represent momentum, where α indicates the amount of acceleration. Momentum has the effect of increasing the speed of learning by increasing the size of steps in directions where the gradient is small but constant in sign.

The adaptive gains, $\epsilon_q(t)$, are increased arithmetically if the gradients remain in the same direction and decreased geometrically if they change direction. More precisely,

$$\epsilon_q(t+1) = \begin{cases} \epsilon_q(t) + \kappa & \text{if } \bar{g}_q(t-1) g_q(t) > 0 \\ (1-\rho)\epsilon_q(t) & \text{if } \bar{g}_q(t-1) g_q(t) \leq 0 \end{cases} \tag{5.13}$$

where

$$g_q(t) = \frac{\partial E}{\partial q}(t), \tag{5.14}$$

and

$$\bar{g}_q(t) = g_q(t) + \alpha \bar{g}_q(t-1). \tag{5.15}$$

The current gradient with respect to q, $g_q(t)$, is compared to a series of previous gradients, $\alpha g_q(t-1) + \alpha^2 g_q(t-2) + \ldots$. The incorporation of the momentum in the adaptation of the learning rate gains, $\epsilon_q(t)$ is known as the *delta-bar-delta* rule. Momentum and adaptive gain are *ad hoc* methods used to increase the speed of learning. They have been shown to work well in practice on a number of problems [57].

5.3.3 Initializing the Optimization Algorithm

Gradient descent methods require an initial selection of parameters before the optimization may begin. In this application, we require initial values of μ_i and σ_i. Typically, these initial values are chosen at random from a reasonable set of possibilities. For example, the variance parameters, σ_i, are often selected to be identical at a value such that there is some overlap between neighbouring Gaussians. The centers are typically chosen to be a subset of input vectors. This is often a satisfactory choice of initial parameter values resulting in suitable solutions for the final parameter values by gradient descent. However, in instances where the error surface is particularly convoluted, simple gradient descent methods can have difficulty finding good local optima. The problem is, in part, due to the initial conditioning of the gradient descent problem. If we were able to find a better starting position for the gradient descent algorithm, with better local minima nearby and a smoother error surface, then we would be able to use gradient descent more effectively. Using an algorithm developed by Chen *et al.* [58], known as the orthogonal least squares (OLS) learning algorithm, we are able to find a set of initial Gaussian centers, μ_i, which are optimal with respect to a set of candidates.

The OLS method involves the formation of a set of orthogonal basis vectors which span the set of $\{\phi_i\}$, where

$$\phi_i = \begin{bmatrix} \phi_i(x_m) \\ \phi_i(x_{m+1}) \\ \vdots \\ \phi_i(x_{D_{OLS}-1}) \end{bmatrix}, 1 \leq i \leq (D_{OLS} - m - 1) \tag{5.16}$$

The parameter D_{OLS} denotes the size of the time series used to construct the vectors which form the set of candidate Gaussian centers. Taking the set of ϕ_i^c as the set of candidate

53

centers, we have $i = 1$ to $i = (D_i - m - 1)$. The orthogonalization procedure permits the calculation of the individual contribution to the reduction of the prediction error, E from 5.4, from each candidate Gaussian basis function. The OLS method allows one to find an optimal set of basis functions to minimize the error.

Following the classical Gram–Schmidt method of orthogonalization, we begin by choosing an initial basis vector, with respect to which, all other basis vectors will be orthogonal. We must choose the initial basis vector from the set of candidates for the initial vector, the set of input vectors $\{x_m, x_{m+1}, \ldots, x_{D_{OLS}-1}\}$ form the centers of the candidate basis functions.

$$p_1^{(i)} = \phi_i. \tag{5.17}$$

For each candidate basis vector, the expansion coefficient is determined by

$$w_1^{(i)} = \frac{(p_1^{(i)})^T d}{(p_1^{(i)})^T p_1^{(i)}}, \tag{5.18}$$

where the vector d is the target output vector after its mean has been removed,

$$d = x_{n+1} - \bar{x}_{n+1}. \tag{5.19}$$

For each candidate basis vector, we compute an error reduction ratio, $[err]_i$, which provides a measure of the extent to which the prediction error of x_{n+1} is decreased by adding candidate basis function i. The error reduction ratio is given by

$$[err]_1^{(i)} = \frac{(w_1^{(i)})^2 (p_1^{(i)})^T p_1^{(i)}}{d^T d}. \tag{5.20}$$

From the set of $[err]_1^{(i)}$ for all the candidate basis functions, for $i = 1$ to $i = (D_i - m - 1)$, we find

$$[err]_1^{(i_1)} = \max\left\{ [err]_1^{(i)}, \quad \text{for } 1 \le i \le (D_i - m - 1) \right\}. \tag{5.21}$$

We choose the corresponding candidate basis function as the initial basis function,

$$p_1 = p_1^{(i_1)} = \phi_{i_1}. \tag{5.22}$$

Once we have determined which of the candidate vectors will become the initial basis function, we repeat the OLS procedure to evaluate each set of candidate set of basis vectors

54

until the best N basis function centers are determined. Using the Gram–Schmidt method, we orthogonalize the candidates for basis function k with respect to the previous $k-1$ best basis functions. Thus, to evaluate the candidates for basis function k we compute, for $1 \leq i \leq (D_i - m - 1)$, $i \neq i_1, \ldots, i \neq i_{k-1}$,

$$p_k^{(i)} = \phi_i - \sum_{j=1}^{k-1} \alpha_{jk}^{(i)} p_j, \tag{5.23}$$

where

$$\alpha_{jk}^{(i)} = \frac{p_j^T \phi_i}{p_j^T p_j}. \tag{5.24}$$

Just as for the initial vector candidate set, the RBF expansion coefficient is determined from the equation

$$w_k^{(i)} = \frac{(p_k^{(i)})^T d}{(p_k^{(i)})^T p_k^{(i)}}. \tag{5.25}$$

Once again we compute the error reduction ratio of each candidate basis vector at each step k in the model building process,

$$[\mathrm{err}]_k^{(i)} = \frac{(w_k^{(i)})^2 (p_k^{(i)})^T p_1^{(i)}}{d^T d}. \tag{5.26}$$

From each set of candidate vectors, we determine the greatest reduction in the error,

$$[\mathrm{err}]_1^{(i_1)} = \max\left\{ [\mathrm{err}]_1^{(i)}, \quad \text{for } 1 \leq i \leq (D_i - m - 1), i \neq i_1, \ldots, i \neq i_{k-1} \right\}, \tag{5.27}$$

and select the corresponding basis vector,

$$p_k = p_k^{(i_k)} = \phi_{i_k} - \sum_{j=1}^{k-1} \alpha_{jk}^{(i)} p_j. \tag{5.28}$$

At the completion of the determination of the N Gaussian basis functions, the 2 step gradient descent optimization strategy described in sections 5.3.1 and 5.3.2 is implemented to improve on the solution obtained through the OLS learning strategy. The gradient descent has the potential to seek a better solution by removing the restriction that the basis functions must be positioned on an input vector, x_n, and by allowing the Gaussian variance to change.

5.4 The Recurrent RBF Model

Once the RBF parameters are estimated, the RBF model is recurrently connected such that the output at time n becomes the model input at time $n+1$. Thus the recurrent RBF Model (rRBF model) is given by,

$$\hat{x}_{n+1} = \sum_{i=0}^{N} w_i \phi_i(\hat{\boldsymbol{x}}_n),$$ (5.29)

where $\hat{\boldsymbol{x}}_n = [\ \hat{x}_{n-(m-1)} \quad \hat{x}_{n-(m-2)} \quad \cdots \quad \hat{x}_n \ ]^T$ is a vector of the RBF model output from times $n - m$ to $n - 1$.

5.5 Application to the Henon Map

In this section, we demonstrate the ability of the RBF network to capture the dynamics of the 2 dimensional Henon map. Introduced in section 2.5, the Henon map has a squared term as the solitary nonlinear element and thus constitutes a relatively simple, though nontrivial, application of the RBF model.

5.5.1 Learning the Henon Map

As a relatively simple difference equation, adequate results are obtained without the use of the OLS method to initialize the gradient descent algorithm. Instead, we choose a sequence of input vectors as the initial values for the Gaussian centers. The variances of the Gaussian basis functions being identical and large enough to allow overlap of one standard deviate between neighbouring RBFs. Table 5.1 provides the values of the parameters used in the learning procedure for the Henon map investigation. The missing parameters are the number of Gaussian basis functions, N; the number of data points used for training, D; and the number of iterations or epochs of the 2 step learning algorithm. These three parameters will be specified for each investigation.

5.5.2 Investigation 1: RBF model of Henon map

The first investigation into the ability of the RBF network to learn and reproduce the dynamics of the Henon map is straight forward. We seek to learn how well the RBF model

Parameter	Symbol	Value
initial value of the Gaussian variance	$(\sigma_i(0))^2$	0.25
initial value of the Gaussian centers	$\mu_i(0)$	x_i for $1 \leq i \leq N$
learning rate	ϵ	0.002
momentum	α	0.0 for $t < 10$ 0.8 for $t \geq 10$
adaptive learning rate increase (additive)	κ	0.1
adaptive learning rate decrease (multiplicative)	ρ	0.5

Table 5.1: *The parameter values for the RBF learning of the Henon map. Listed here are the parameters which remain constant throughout the investigations of the RBF network application to the Henon map.*

performs under ideal circumstances.

We form an RBF model with 20 Gaussian basis functions and train the network for 100 epochs of the 2 step learning procedure. A time series of 5000 points of the chaotic Henon map ($b = 0.3$, $a = 1.4$) was used as the training set. Figure 5.1 illustrates the normalized training error, $E/(D - m - 1)$ over the 100 epochs. The plot reveals that the training error, normalized with respect to the number of training vectors, before the beginning of the gradient descent algorithm (epoch $= 0$), is remarkably low at 4.295×10^{-4}. This is the result of the least-squares optimization of the expansion coefficients, w_i. It is very common for users of RBF models to stop at the fast linear optimization of the coefficients and to do without the slower nonlinear optimization of the basis function parameters. Despite the effectiveness of the linear optimization of the coefficients, the gradient descent 2–step optimization which estimates both the basis function parameters, μ_i and σ_i, and the expansion coefficients, w_i, is able to improve upon the initial error by over a factor of 100 to a final error at epoch 100 of $E/(D - m - 1) = 2.6 \times 10^{-6}$. The RBF model of the Henon map, after 100 training epochs, is represented in Figure 5.2.

The most severe test of a model's ability to capture the dynamics of the learned system is to continually iterate the model from a starting point from the time series [4]. Figure 5.3 illustrates the attractor formed by the output of the rRBF model, iterated 5000
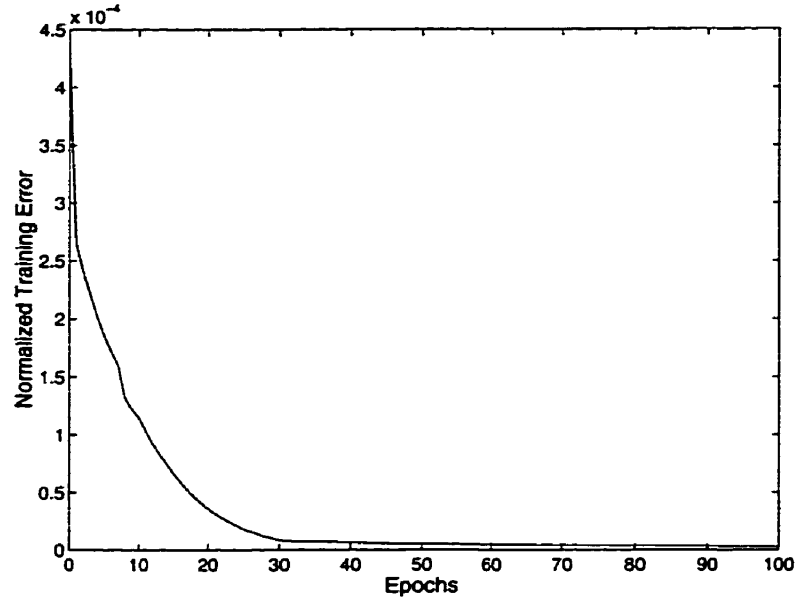
Figure 5.1: Training Error evolution through 100 epochs. The Training Error is normalized with respect to the number of training vectors.
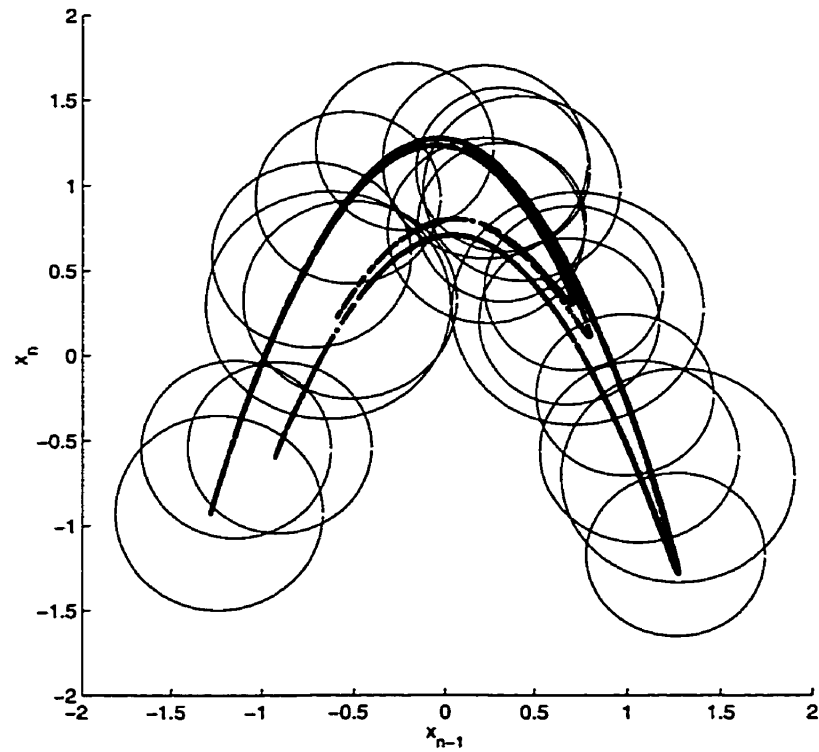
Figure 5.2: Henon attractor (points) and the RBF model (circles). The circles represent one standard deviation, σ_i, about the center, μ_i.
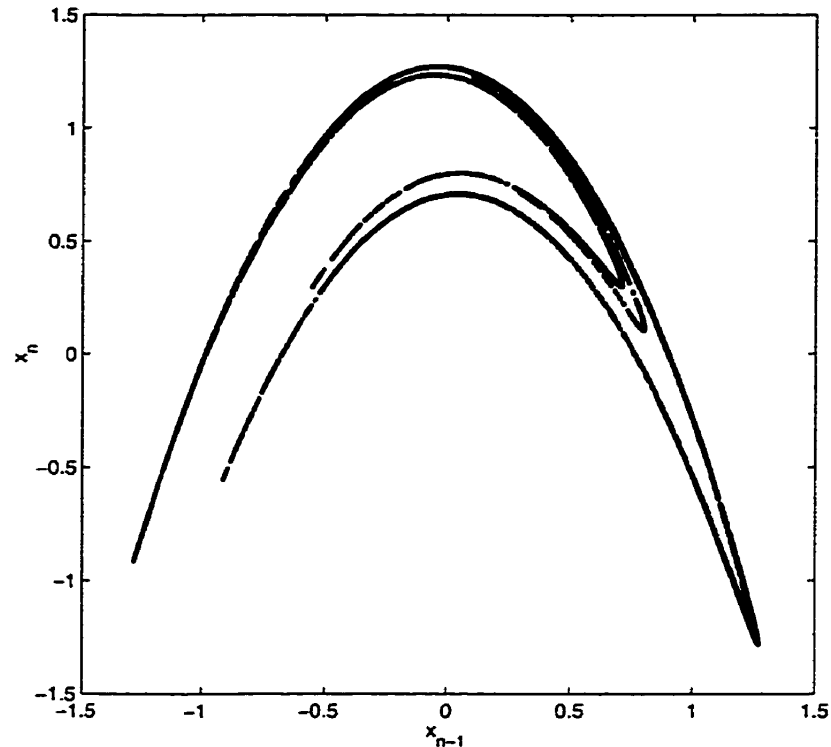
Figure 5.3: *The attractor formed by 5000 iterations of the the rRBF model of the Henon map.*

times. Comparing Figures 5.3 and 2.1, we see that the rRBF model attractor is almost identical to that of the Henon map. The corresponding rRBF model time series, shown in Figure 5.4 is, once more, virtually indistinguishable from the Henon map time series.

Depicted in Figure 5.5 is a comparison between the short term evolution of the rRBF model from its initial condition and that of the Henon map from the same starting point. We see good initial agreement between the rRBF and Henon time series, after some time the two series diverge until they appear unrelated. The rate of divergence between the rRBF model time series and the Henon map time series is similar to that observed between two nearby trajectories of the Henon map itself (shown in Figure 2.4). It is evident that any detection and control strategies we wish to employ cannot be critically dependent on the long–term prediction capabilities of the model. No model of chaos will ever achieve success in this regard.

Based on the results of the rRBF model performance in reproducing the Henon attractor, we suggest that the RBF model is successful in capturing the dynamics of the Henon
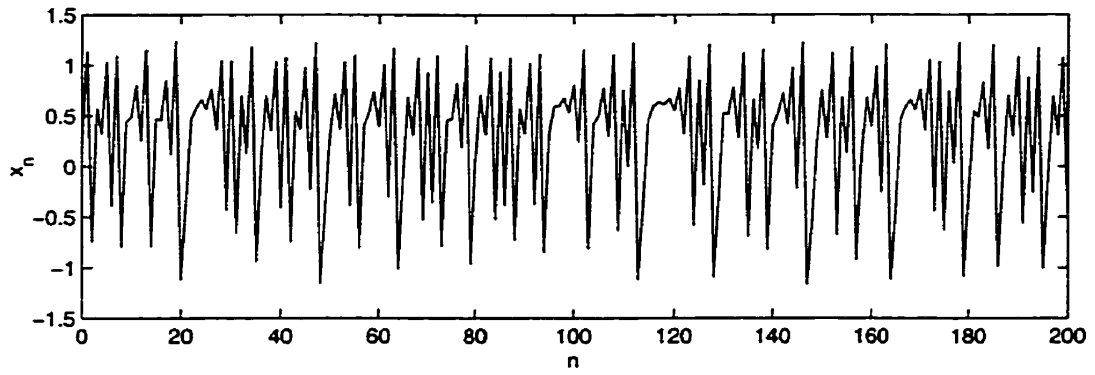
Figure 5.4: *The time series of the rRBF model of the Henon map.*

rRBF model
Henon map
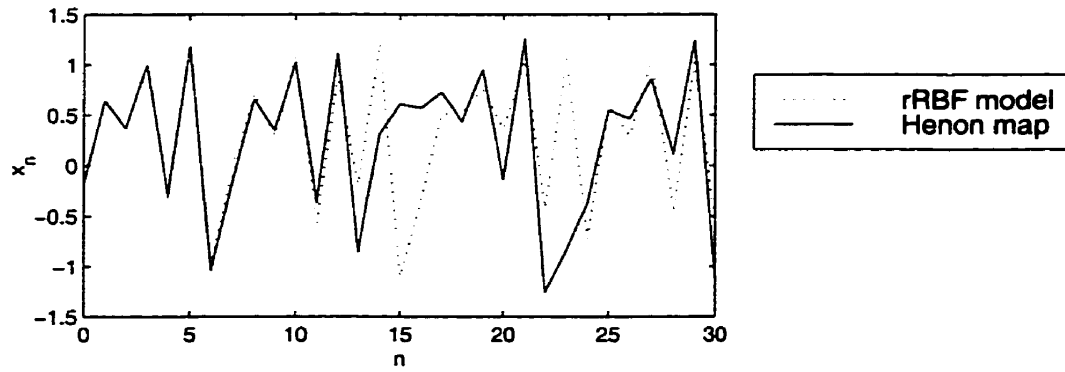
Figure 5.5: *The time series of both the rRBF model and the Henon map originating from the same initial conditions.*

map.
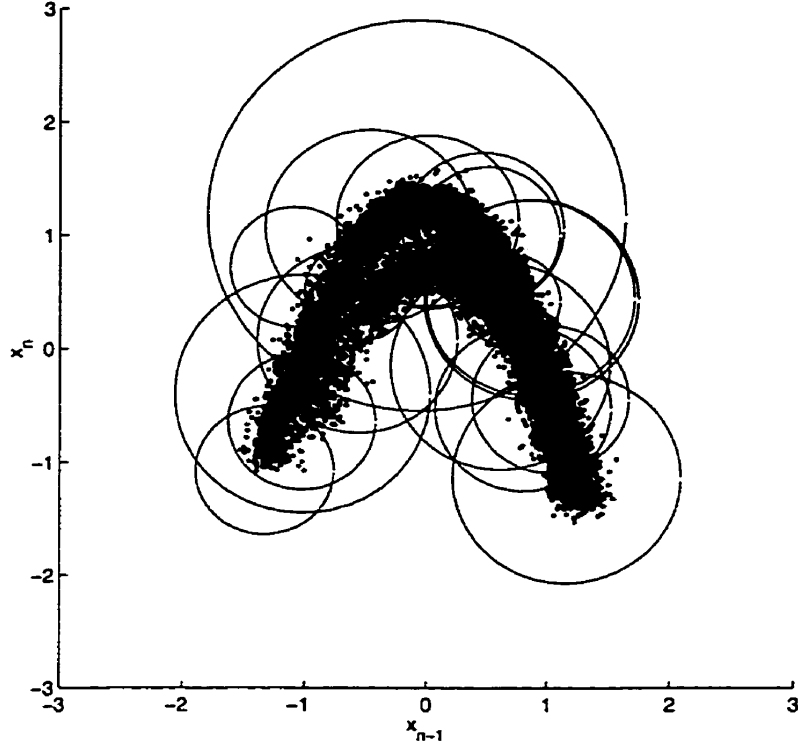
Figure 5.6: *Henon attractor corrupted with Gaussian noise at* SNR = 17.7dB *(points) and the trained RBF model (circles). The circles represent one standard deviation, σ_i, about the center, μ_i.*

5.5.3 Investigation 2: RBF learning on noisy Henon time series

The previous investigation illustrated the potential of the RBF model under ideal conditions. In real world applications, the circumstances are often suboptimal, measurement noise often corrupts real time series data. In this investigation, we explore the capabilities of the RBF model to learn dynamics in the presence of additive noise. The RBF model learns from a time series of the Henon map corrupted with Gaussian white noise to a signal to noise ratio (SNR) of 17.7dB.

As before we use an RBF model with 20 Gaussian basis ($N = 20$), trained for 100 epochs. The training set consists of 10000 input/output vector pairs ($D = 10002$). Figure 5.6 illustrates the trained RBF model with the noisy Henon map time series. The large difference between the variances of the Gaussian basis functions is a product of gradient descent optimization on the degraded training set.
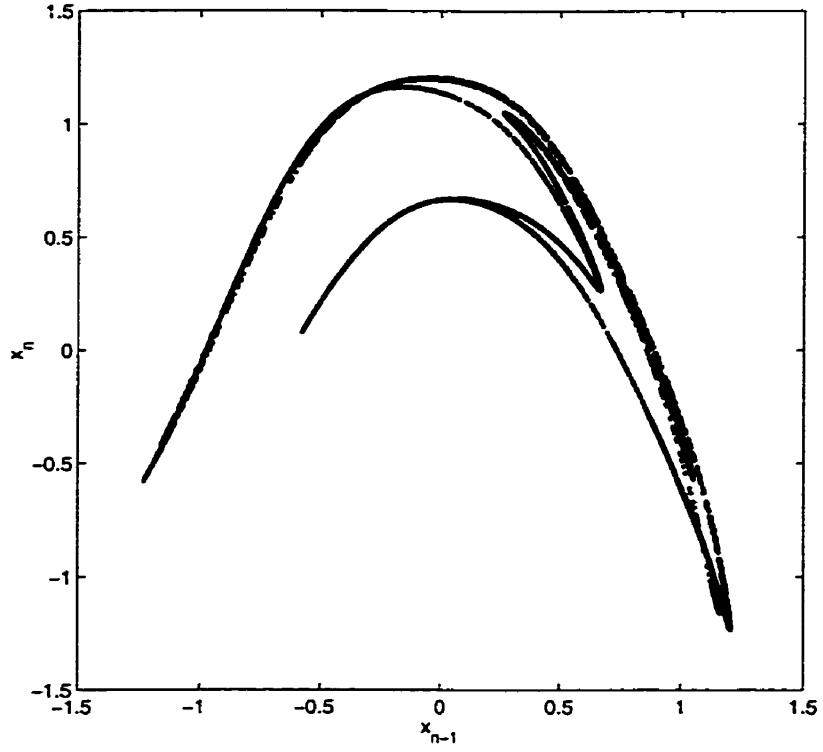
Figure 5.7: The attractor formed by 5000 iterations of the rRBF model trained on the Henon map time series corrupted with noise.

The result of the continual iteration of the rRBF model trained on the noisy time series is revealed in Figure 5.7. Despite the corruption of the training set, the rRBF model is still able to capture the original Henon attractor in some detail. Figure 5.8 illustrates the corresponding time series of this rRBF model.

With this investigation, we demonstrate the ability of the RBF model to extract the underlying dynamics from a time series corrupted with noise. While the rRBF attractor is by no means a perfect recreation of the original Henon attractor, a comparison between the noisy Henon attractor (as shown in Figure 5.6) with the attractor formed by the iteration of the rRBF model reveals a surprising ability of the RBF model to capture details not apparent in the corrupted attractor.
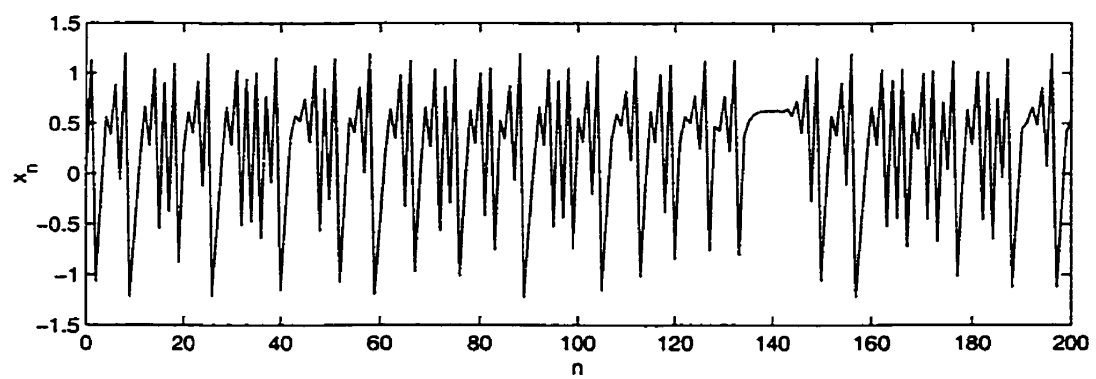
Figure 5.8: The time series of the rRBF model trained on the Henon map time series corrupted with noise.
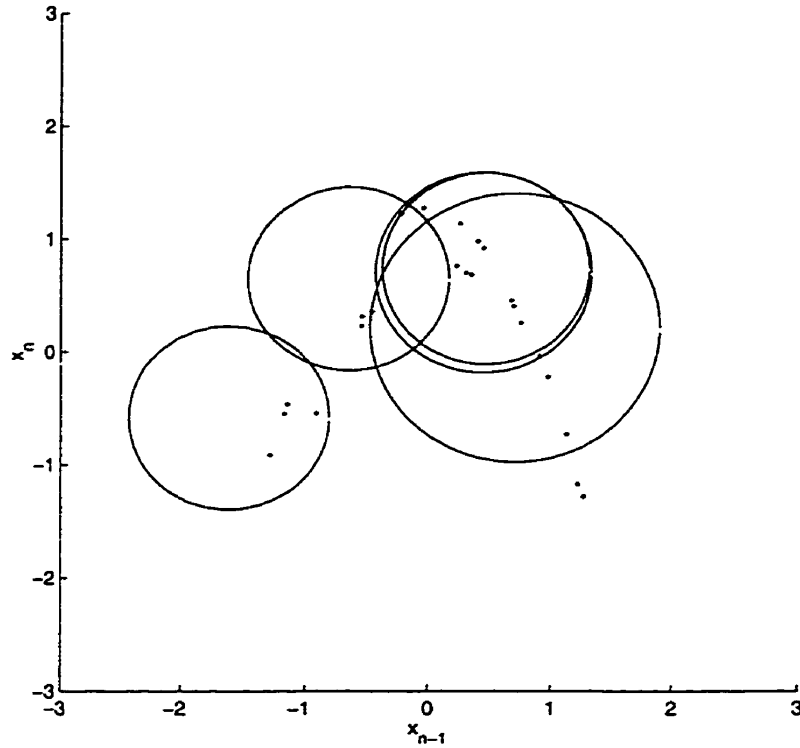
Figure 5.9: *Henon attractor formed by 25 points of the Henon map (points) and the corresponding RBF model (circles). The circles represent one standard deviation, σ_i, about the center, μ_i.*

5.5.4 Investigation 3: RBF learning on a small time series

In addition to noise, another problem commonly faced by individuals dealing with time series modeling and analysis is a deficiency in the amount of data. Often good data (large sets of "clean" experimental data) is very difficult to come by and is usually expensive to obtain. Thus it would be a significant asset if the RBF model was able to learn the subject system dynamics from a limited number of data points.

In this experiment, we limit the number of input/output training pairs to 25 instead of the 5000 used in Investigation 1. The RBF model used in this investigation consists of only 5 Gaussian basis functions, in order to avoid an overdetermined estimation of the model parameters. The 5 Gaussian basis function model is trained for 1000 epochs resulting in the model represented in Figure 5.9.

Once again we iterate the rRBF model starting from an initial condition taken from
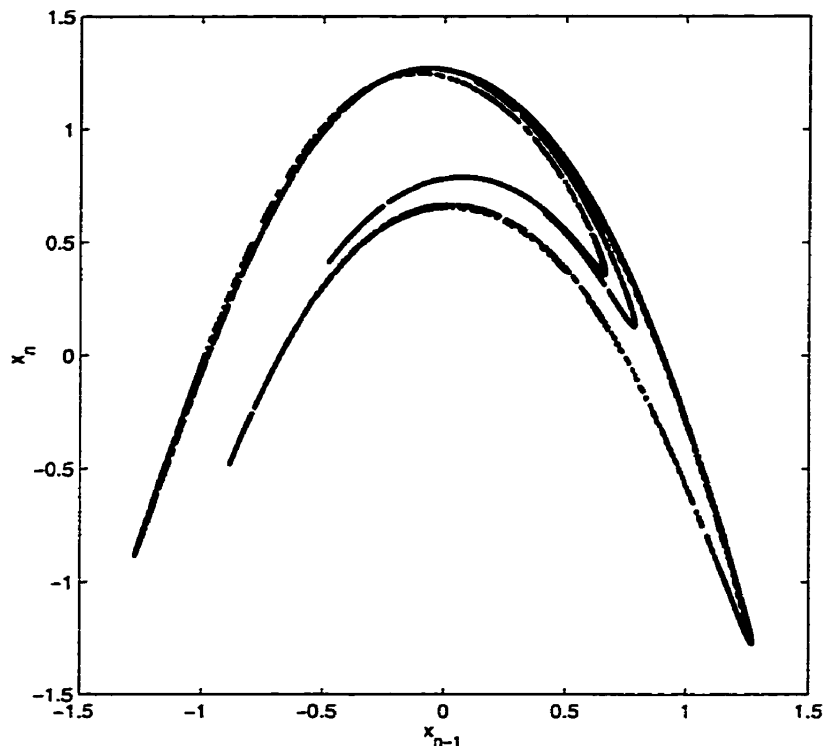
Figure 5.10: *The attractor formed by 5000 iterations of the rRBF model trained on 25 points from the Henon map.*

the training set. The rRBF model attractor formed by the iterations is shown in Figure 5.10. Figure 5.11 depicts the corresponding time series. A remarkable amount of detail in agreement with the original Henon map, is visible in these figures.

Comparing the image of the 25 point attractor (in Figure 5.9) with the attractor formed by the continual iteration of the rRBF model trained on those 25 points (in Figure 5.10) and we see that the RBF model has captured the Henon dynamics which do not appear to be contained within the 25 point training set.

It is not known exactly how the RBF model managed to extract that level of detail from the 25 point time series. We propose that the explanation of this puzzle rests in the relative simplicity of the analytical form of the Henon map. The RBF model may come close to realizing an approximation to the analytical model itself which naturally fits the data and thus is able to capture topological features of the Henon attractor which are simply not represented by the 25 point time series. One looks at the Henon attractor and sees a rather complex shape, on the other hand the equation from which the complexity arises, is itself
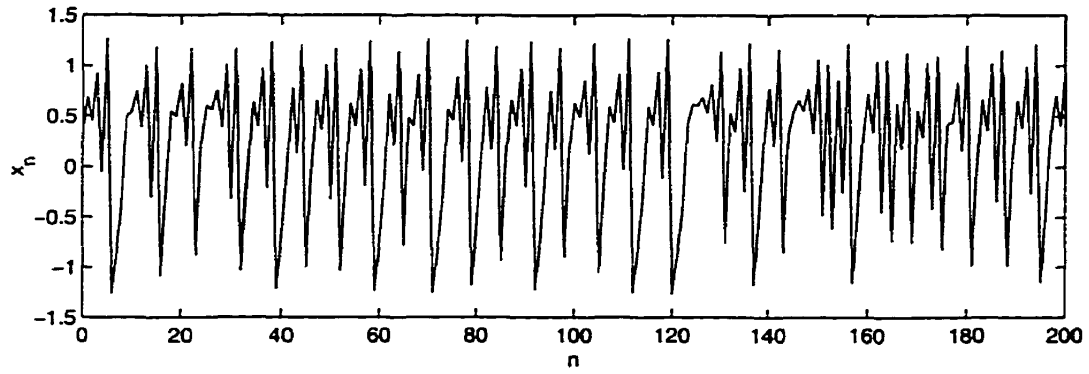
Figure 5.11: *The time series of the rRBF model trained on the small time series of the Henon map.*

quite simple.

From the results presented here, we propose that the RBF model is well suited to situations where a limited amount of data is available. We must bear in mind that before much can be said about the ability of the RBF model to capture dynamics from small data sets, subsequent investigation is required into its performance on other systems with limited training data.

5.6 Application to the MCO model

In this section, we apply the RBF model to the problem of learning the dynamics of the interspike interval (I) dynamics of the chaotic MCO model. The MCO model interspike interval dynamics represents a significantly more challenging task for the RBF model than learning the Henon map. There are a number of reasons why. First, the dynamics must be learned in four dimensions which, when compared to the problem of learning in two dimensions, substantially increases the number of parameters to be estimated and reduces the density of training data in state space. Second, the MCO model, as described in section 2.6, contains considerably more nonlinear elements which tend to make the optimization error surface more convoluted and, as a result, more difficult to navigate. Finally, the interspike interval, while arising from an encoding of a well defined system, lacks explicit description in the form of an equation. The complexity of the dynamics to be modelled is not entirely known.

5.6.1 Learning the MCO model

In order to achieve reasonable learning we require that the OLS learning algorithm be applied to initialize the gradient descent algorithm. Through repeated trials, we found that the best results were obtained when we set the Gaussian variances to be a function of the local density of data vectors in state space. One standard deviation of the Gaussian is set equal to the distance to the 250th closest vector, I^{250}. This allows state space regions of higher vector density to be modelled in greater detail. Table 5.1 provides the values of the parameters used in learning the MCO model.

The Figure 5.12 shows the normalized training error, $E/(D - m - 1)$, as a function of epoch number. The sharp fluctuations visible in the plot correspond to steps taken by the gradient optimization method which have increased the error. The presence of these fluctuations is an indication of a highly convoluted search space for the optimization algorithm. A state space representation of the final version of the RBF model of the MCO interspike interval dynamics is given in Figure 5.13. It is evident that the majority of the Gaussian centers are concentrated around the region close to $I_n = I_{n-1} = 1$. Thus reflecting the concentration of data in that region.

Parameter	Symbol	Value
initial value of the Gaussian centers	$\mu_i(0)$	p_i for $1 \le i \le N$
initial value of the Gaussian standard deviation	$\sigma_i(0)$	$\|\mu_i - I^{250}\|$
learning rate	ϵ	$0.0001\sigma_i(0)$
momentum	α	0.0 for $t < 10$ 0.8 for $t \ge 10$
adaptive learning rate increase (additive)	κ	0.1
adaptive learning rate decrease (multiplicative)	ρ	0.5
number of Gaussian basis functions	N	250
number of candidate RBF centers for OLS	D_{OLS}	5000
number of training vectors	D	25000
number of epochs	-	1600

Table 5.2: *The RBF learning algorithm parameters for the MCO model.*
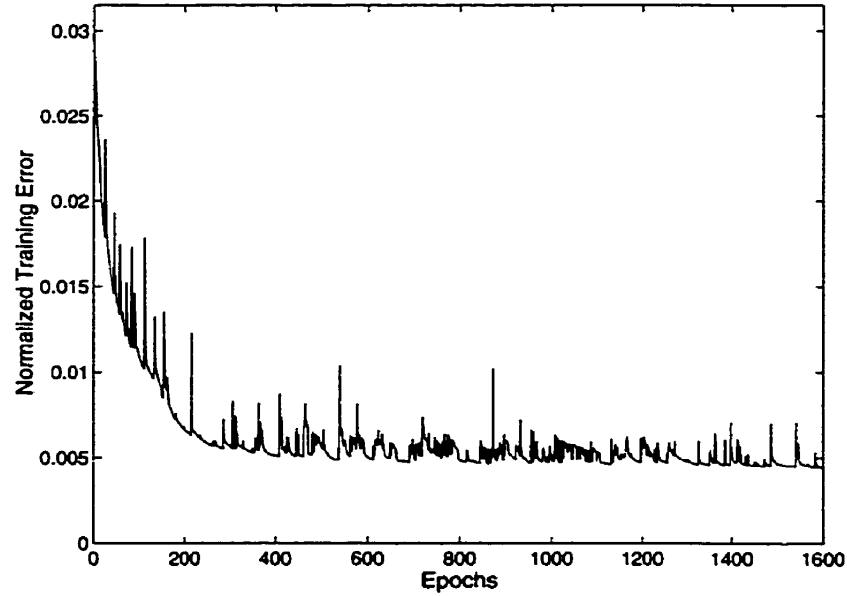
Figure 5.12: *The training error evolution through 1600 epochs while learning the MCO dynamics. The training error is normalized with respect to the number of training vectors, $E/(D - m - 1)$.*
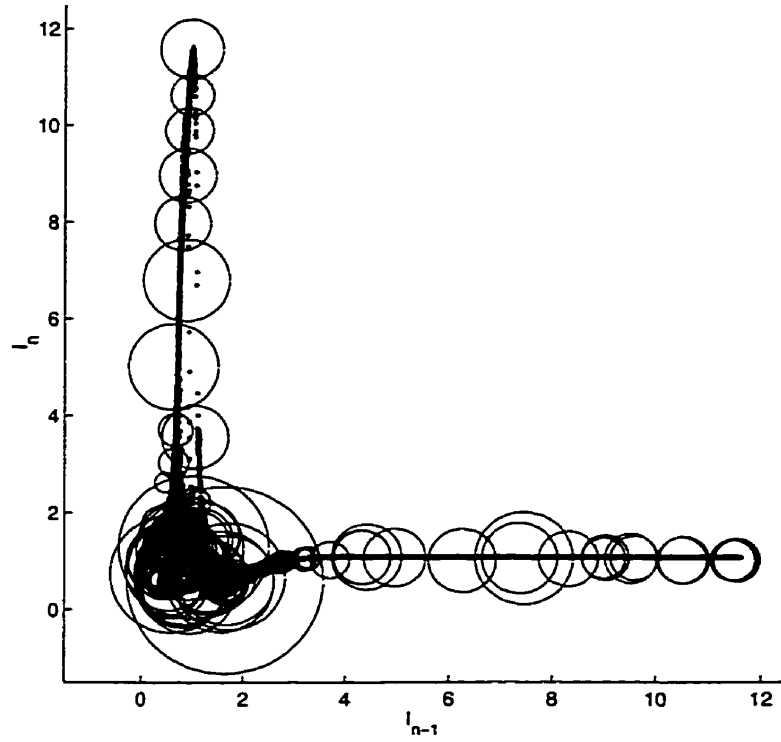
Figure 5.13: MCO *interspike interval data (points) and the trained RBF model (circles). The circles represent one standard deviation,* σ_i, *about the center,* μ_i.
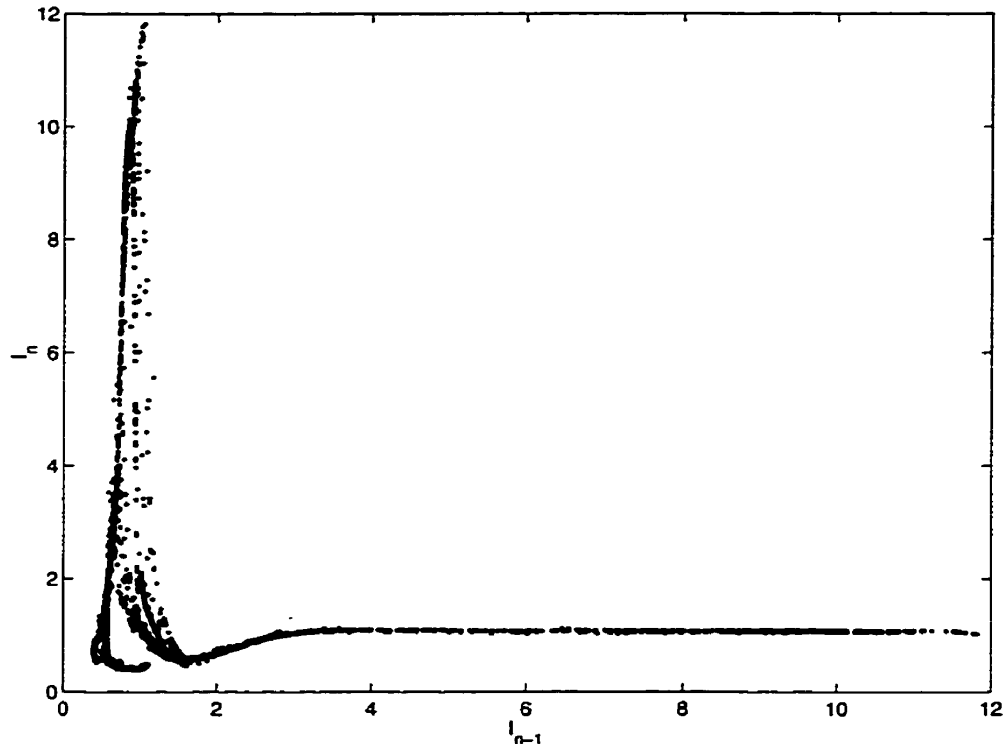
Figure 5.14: *The attractor formed by 5000 iterations of the the rRBF model of the MCO interspike interval dynamics.*

5.6.2 The trained RBF model

Just as was done for the RBF models of the Henon map, we evaluate the learned dynamics of the RBF model by continually iterating the RBF model from a starting point in the training data. Figure 5.14 illustrates the attractor formed by the output of the rRBF model iterated 5000 times. Comparing Figures 5.14 with 2.14, we see that the rRBF model attractor captures many of the features of the MCO interspike interval attractor; however; the attractor of the RBF model of the MCO interspike interval is not as similar to the original attractor, as was the case for the RBF model of the Henon map.

Figure 5.15 shows the time series representation of the rRBF model interspike intervals. Comparison between the rRBF model I_n time series and the MCO model I_n time series (Figure 2.13) reveals many similar characteristics. An example of such a characteristic is the brief near period-1 oscillation in the neighbourhood of $I_n = 1$.

The results show that, despite the difficulties surrounding the learning of the MCO
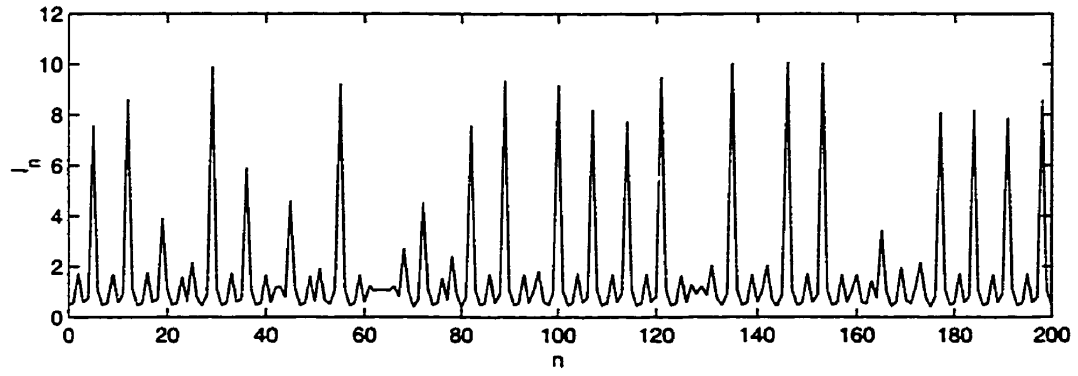
Figure 5.15: *The time series of the rRBF model of the MCO interspike interval dynamics.*

I_n data, the RBF model is capable of capturing the higher dimensional, highly nonlinear dynamics represented in the interspike interval data of the MCO.

Chapter 6

Detection of Rhythmicity

In this chapter we will discuss the development of the algorithm for the detection of rhythmicity in systems which spontaneously switch to rhythmic activity either as a result of intermittent activity or through the action of a parameter drift. The eventual goal is to detect the transition to epileptic seizure through the detection of rhythmic, reduced complexity neurodynamics.

We begin by describing the qualities of the ideal detector . In section 6.2, we describe the detection algorithm in some detail. Then, the algorithm is applied to detecting rhythmicity in the two subject systems, the Henon map and the MCO.

6.1 The Ideal Detector

What do we require in our detection algorithm? We require it to identify sudden increases in rhythmicity as fast as possible. The sooner rhythmic activity is detected, the sooner a control action may be initiated to restore the chaotic activity. Whatever detection algorithm is developed must be capable of fast detection. It must also be sensitive, in the sense that it must be able to repeatedly detect every instance of increased rhythmicity of the subject system dynamics. Undetected rhythmicity would result in untreated seizures, and thus must be minimized. The detection algorithm must be specific, only signaling a positive detection of rhythmicity when the activity has indeed become more rhythmic. False positives of our detection algorithm would result in unwarranted stimulation of the neural tissue. This is in direct opposition of our goal to minimize the amount of stimulation. The final requirement

of the system is that it be capable of detecting any rhythmic pattern of activity, as there may be more than one rhythmic mode of the neural dynamics, or the rhythmic pattern may change over time, therefore the detection algorithm must be flexible.

6.2 Detection Algorithm

Our detection algorithm is structured around a straight forward statistical tool, the *t-test* [4]. We use the rRBF model of the chaotic activity as a model of healthy system behaviour which we compare through the *t-test* to the current state of the subject system, $\mathcal{F}$, which at some point we expect to slip into rhythmic activity.

6.2.1 The Statistic

We require a test statistic, τ, which will differentiate a rhythmic signal from a chaotic signal with relatively few data points. To determine an appropriate statistic we must first review some of the differences between chaotic and periodic signals. On average, nearby trajectories in a chaotic system evolve away from one another at an exponential rate until the distance between them matches the mean distance between pairs of points on the attractor. In the case of rhythmic trajectories, nearby trajectories will tend to stay close to each other. Thus comparing a quantity proportional to the long-term evolution of the distance between initially nearby trajectories would act as a discriminator between chaotic and periodic signals. This concept forms the basis of the test statistic.

Turning briefly to the computation used in the determination of the maximum Lyapunov exponent described in section 2.4.2, we see that the function $S(\Delta n)$ is calculating something very similar to our desired test statistic. After a period of exponential expansion, $S(\Delta n)$ saturates to the log of the mean distance between two arbitrary trajectories on the attractor. Thus we may assign our test statistic to be

$$\tau = S(\delta n) = \frac{1}{\mathcal{N}} \sum_{n_0=(n-\mathcal{N})}^{n_0=n} \ln \left(\frac{1}{|\mathcal{U}(x_{n_0})|} \sum_{x_{n_d} \in \mathcal{U}(x_{n_0})} |x_{n_0+\delta n} - x_{n_d+\delta n}| \right), \qquad (6.1)$$

where δn covers the range of the "flat line" values of $S(\Delta n)$ for which the slope of $S(\Delta n)$ is near zero. Statistical considerations motivate the choice of the "flat line" region of $S(\Delta n)$.
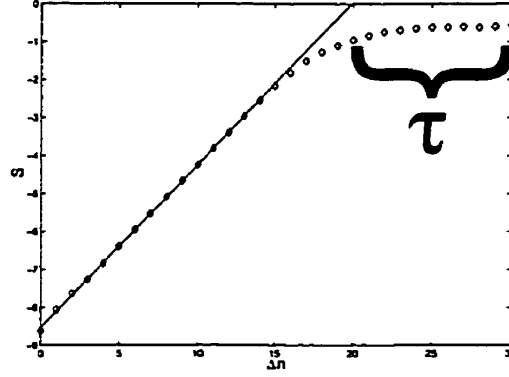
Figure 6.1: $S(\Delta n)$ of the Henon Map. Note that τ is the set of $S(\Delta n)$ over the saturated region of the curve for $20 \leq \Delta n \leq 30$.

Figure 6.1 illustrates $S(\Delta n)$ for the Henon map and shows the set τ.

The function $S(\delta n)$ is computed over a moving window of size $\mathcal{N}$, from $n - \mathcal{N}$, in the past, to the current step,n. Every vector, x_{n_d} is reconstructed from the set $\{n - \mathcal{N}, \ldots, n - \mathcal{M}\}$, where $\mathcal{M}$ is the number of elements in Δn. In order to use this as our test statistic we must interpret the set of points $\{\tau\}$ as independent samples from a population of measurements of the mean of the log separation between pairs of trajectories originally within an ϵ-neighbourhood of each other. In this interpretation the saturated region of $S(\Delta n)$, $\Delta n = \delta n$, constitutes a series of uncorrelated, independent measurements. This is an approximation; often there is a shallow trend toward increasing S with increasing δn.

Now that we have a test statistic, τ, we need to apply the statistic to healthy dynamics of the subject system, $\mathcal{F}$ and to the current state of $\mathcal{F}$. We can gauge the degree of rhythmicity in the current state of $\mathcal{F}$ by comparing it to chaotic dynamics of the system healthy system dynamics are represented by the recurrent RBF (rRBF) model trained on the chaotic dynamics of $\mathcal{F}$. Therefore we compare the population τ_{rRBF} to the population $\tau_{\mathcal{F}}$.

Quantities such as the correlation dimension and the maximal Lyapunov exponent are averaged quantities of measurements made over the entire attractor. There is often considerable variability between the local or instantaneous measures. Our statistic τ is not an exception. In order to ensure that the comparison between $\tau_{\mathcal{F}}$ and τ_{rRBF} is valid, we iterate the rRBF model from the identical ϵ-neighbourhood pairs as identified in the moving

window of size $\mathcal{N}$.

6.2.2 Comparing τ_{rRBF} to $\tau_{\mathcal{F}}$

In comparing the two measurement sets, τ_{rRBF} and $\tau_{\mathcal{F}}$, we make use of a well known statistical methodology, the *t-test* [59]. We are interested in determining if $\tau_{\mathcal{F}}$ is significantly smaller than τ_{rRBF}, indicating that the nearby trajectories are now remaining nearby, in contrast to the healthy chaotic activity, where nearby trajectories diverge. We interpret a significant difference between our two populations as 3 standard deviations, where the standard deviation used in the comparison is pooled from the two populations and is given by,

$$\varsigma_p^2 = \frac{\sum_{\delta n}(\tau_{\mathrm{rRBF}} - \bar{\tau}_{\mathrm{rRBF}})^2 + \sum_{\delta n}(\tau_{\mathcal{F}} - \bar{\tau}_{\mathcal{F}})^2}{2(\mathcal{L} - 1)} \tag{6.2}$$

where $\bar{\tau}$ is the mean of τ and $\mathcal{L}$ the number of elements in each of the sets τ_{rRBF} and $\tau_{\mathcal{F}}$.

We are looking for instances where $\tau_{\mathcal{F}}$ is significantly smaller than τ_{RBF}. An appropriate test for this situation is the one-sided *t-test* with a the null hypothesis that $\bar{\tau}_{\mathrm{rRBF}}$ is not $3\varsigma_p$ larger than $\bar{\tau}_{\mathcal{F}}$, given by,

$$t = \frac{(\bar{\tau}_{\mathrm{rRBF}} - \bar{\tau}_{\mathcal{F}}) - 3\varsigma_p}{\sqrt{\frac{2\varsigma_p^2}{L(\delta n)}}}. \tag{6.3}$$

If we wish to interpret the results of the *t-test* in a statistically significant way there are a number of implicit assumptions regarding the nature of our statistics, τ_{rRBF} and $\tau_{\mathcal{F}}$, which must be considered. The first assumption is that the populations, τ, are assumed to be normally distributed. The populations τ_{rRBF} and $\tau_{\mathcal{F}}$ consist of samples of average distances between trajectories pairs which were initially ϵ-neighbours. If the average was taken over a large number of pairs of trajectories (say, $L(\beta_{n_d} \in \mathcal{U}(\beta_{n_0})) > 20$), then we may apply the Central Limit Theorem to ensure that the populations τ are normally distributed. In this application the length of the observer window needed to satisfy the Central Limit Theorem requirement of a large number of trajectory pairs could result in unnecessary delays in detecting rhythmicity, which the statistic interpretability does not warrant. The second assumption is that the populations τ_{rRBF} and $\tau_{\mathcal{F}}$ have equal variance. It should be obvious that during the chaotic operation of the system, $\mathcal{F}$, the variances of our statistics should be very close, provided the rRBF model faithfully captured the chaotic dynamics of $\mathcal{F}$.

However, when $\mathcal{F}$ slips into rhythmic or periodic activity, the variance in the separation of trajectory pairs reduces dramatically as the trajectories begin to stay close together over long periods of time.

Although the hypothesis testing on our statistics τ does not appear to be statistically interpretable as a true *t-test*, the measure does provide a reliable and flexible method of detecting rhythmicity, as we shall see. The consequence is that relatively little meaning may be attributed to the significance level of the test. The value of t_α simply provides a threshold above which we claim to have detected rhythmicity.

6.3 Application to the Henon Map

To illustrate how our rhythmicity detection strategy works, we apply it to the problem of detecting periodicity in the Henon map. As discussed in section 2.5, the Henon map is chaotic when the parameters have the values $a = 1.4$ and $b = 0.3$; however, when the parameter a is changed slightly to $a = 1.42207$ a period–30 orbit is stabilized in the midst of the chaotic attractor of the Henon map.

6.3.1 Initializing the Detection Algorithm

There are a number of parameters which define the action of the detection algorithm. In order to achieve adequate performance, these parameters must be appropriately selected for the system under observation. Table 6.1 displays the values of the parameters selected for the Henon map. The window size of $\mathcal{N} = 80$ is chosen to ensure that, within the chaotic dynamics, there is always at least one pair of trajectories within a box of side $\epsilon = 0.05$. We use a detection threshold of $t_\alpha = 15$.

6.3.2 Investigation 1: Single Event Detection

The first experiment involves the tracking of the Henon map iterations through a single switch from the chaotic mode ($a = 1.4$) to the periodic mode ($a = 1.42207$). Using the RBF model demonstrated in section 5.5.2 with 20 Gaussian basis functions, we initiate the detection algorithm.

76

Parameter	Symbol	Value
side of small box in state space	ϵ	0.05
size of moving window	$\mathcal{N}$	80
number of elements in δn	$L(\delta n)$	10
number of elements in Δn	$\mathcal{M}$	30
threshold	t_α	15

Table 6.1: The parameter values for the detection algorithm applied to the Henon map.

Figure 6.2: The Henon map time series from $n = 80$ to $n = 320$. The parameter a changes from $a = 1.4$ to $a = 1.42207$ at $n = 70$. The periodic dynamics begin at $n = 165$ and are detected by the detection algorithm at $n = 220$.

Figures 6.2 and 6.3 illustrate the time series from $n = 80$ to $n = 320$. At $n = 70$ the value of a is switched from $a = 1.4$ to $a = 1.42207$. As expected, the Henon map remains in a chaotic transient for some time before it slips into the periodic dynamics at $n = 163$.

The two statistics, τ_{Henon} and τ_{rRBF} are compared in Figure 6.4. Shortly after the Henon dynamics lock into periodic motion, τ_{Henon} drops dramatically as nearby trajectories no longer diverge. Using these two populations in equation 6.3 results in the evolution of t shown in Figure 6.5.

The the evolution of the comparator t is depicted in Figure 6.5. The value of t rises dramatically during the periodic behaviour of the Henon map. This indicates that the measure t provides a reliable method of detecting rhythmicity. In a short number of time steps, t reaches it's maximum of 189.
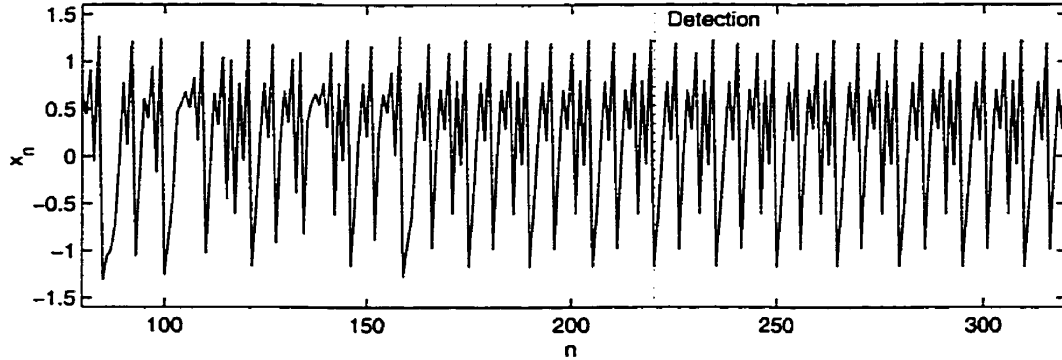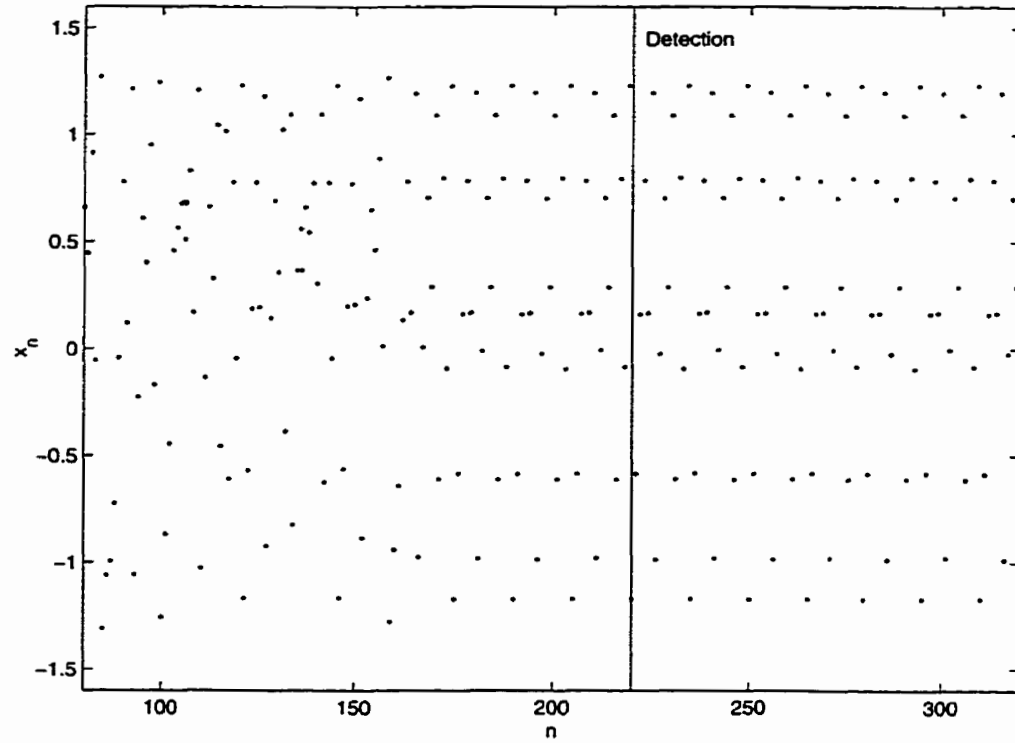
Figure 6.3: *Disconnected plot of the Henon map time series from $n = 80$ to $n = 320$. The parameter a changes from $a = 1.4$ to $a = 1.42207$ at $n = 70$. The periodic dynamics begin at $n = 165$ and are detected by the detection algorithm at $n = 220$.*
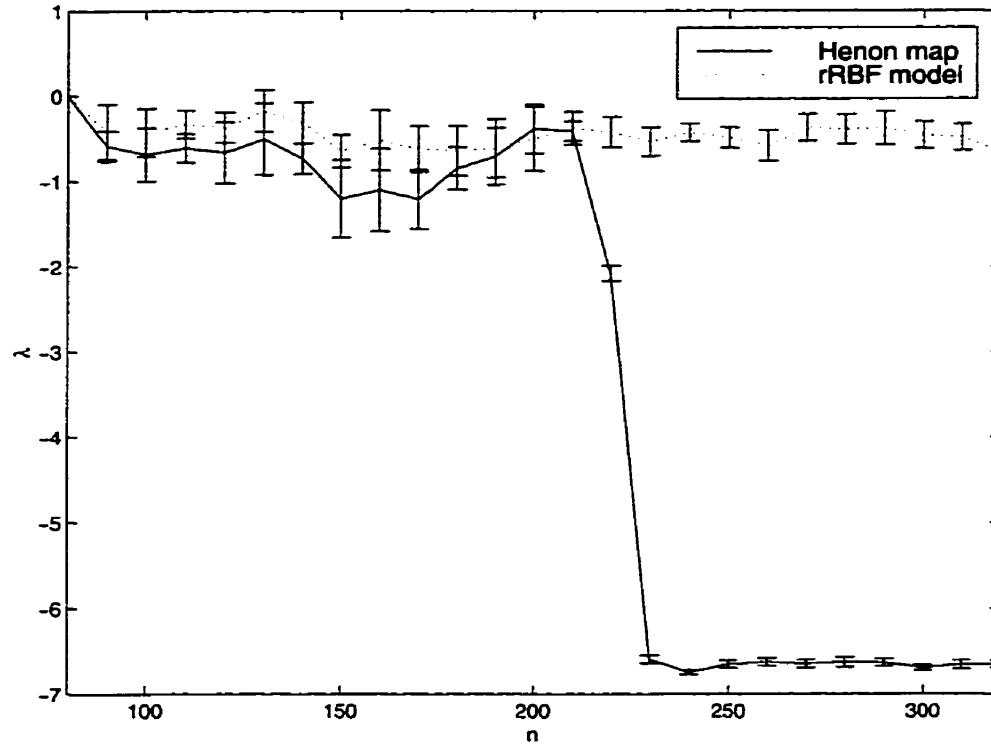
Figure 6.4: *Comparison of the two populations* τ_{Henon} *and* τ_{rRBF} *for the time series shown in Figure 6.2.*
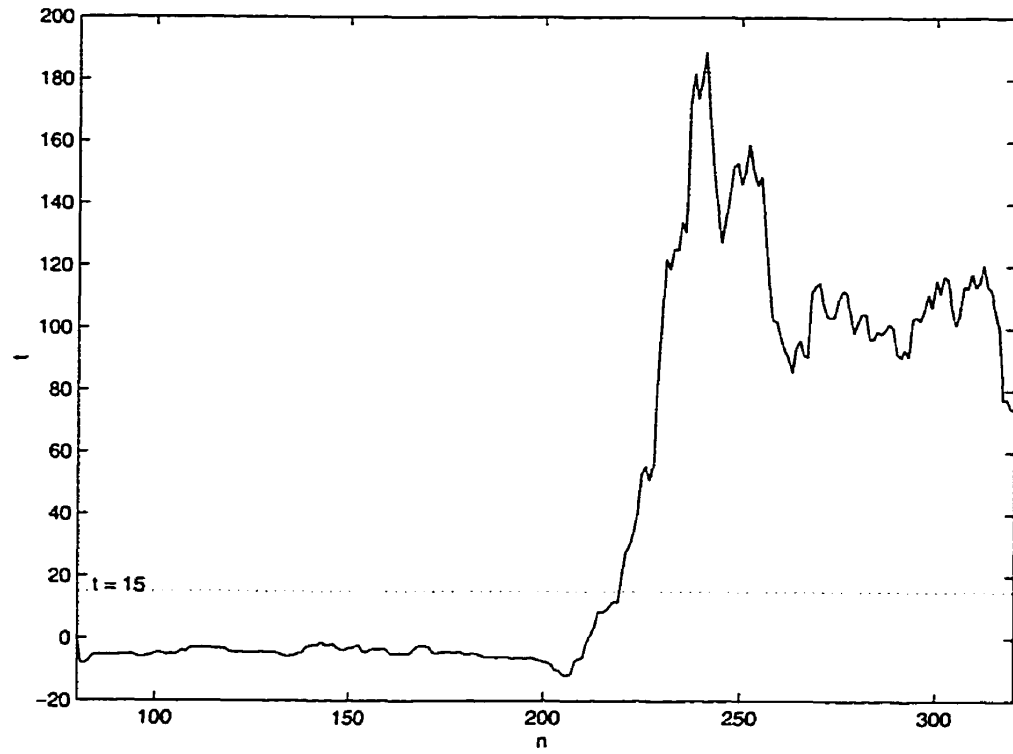
Figure 6.5: *The evolution of t calculated from τ_{Henon} and τ_{rRBF} given in Figure 6.4.*

6.3.3 Frequency Domain Detection

Before we continue with further exploration of the detection strategy, we should compare its performance with that of a more obvious approach: frequency domain detection. Rhythmicity implies the visible distinction of one group of frequencies in the time series. Thus it seems an appropriate method of detection to look for peaks in the Fourier transform of the time series.

Figure 6.6 (a) depicts the discrete Fourier transform (DFT) of a segment of the time series from which our detection algorithm determined a true positive for detection of rhythmicity. The segment of the time series corresponds to the window over which the detection algorithm computes the statistic τ. Figure 6.6 (b) shows the discrete Fourier transforms (DFT) of the chaotic Henon map ($a = 1.4$) over four unrelated segments of the same size as shown in Figure 6.6. Comparing the discrete Fourier transforms presented in the two figures, it is not obvious how one might go about distinguishing the rhythmic signal from the chaotic signals.

The detection algorithm developed as part of this thesis appears able to detect rhythmicity before it becomes apparent in the frequency domain. With a larger window size the chaotic and periodic Henon map time series look noticeably different and detection from the frequency domain would become feasible. However, the larger window size would have the effect of delaying the detection of rhythmicity by requiring more samples of the rhythmic activity.
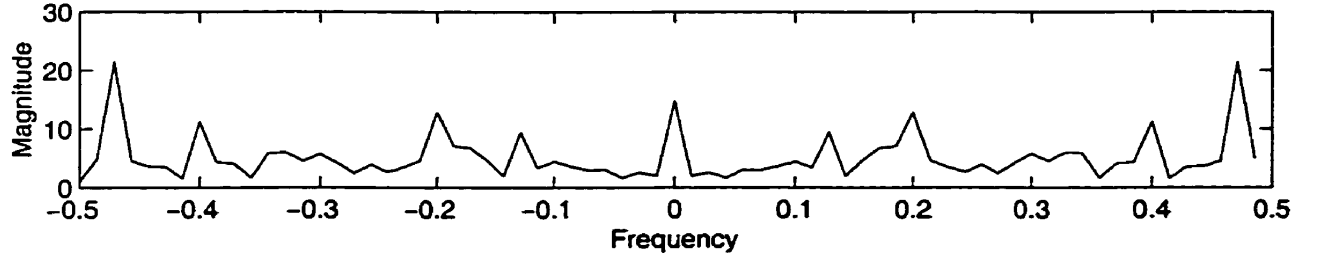
(a) DFT of a segment of the periodic Henon map
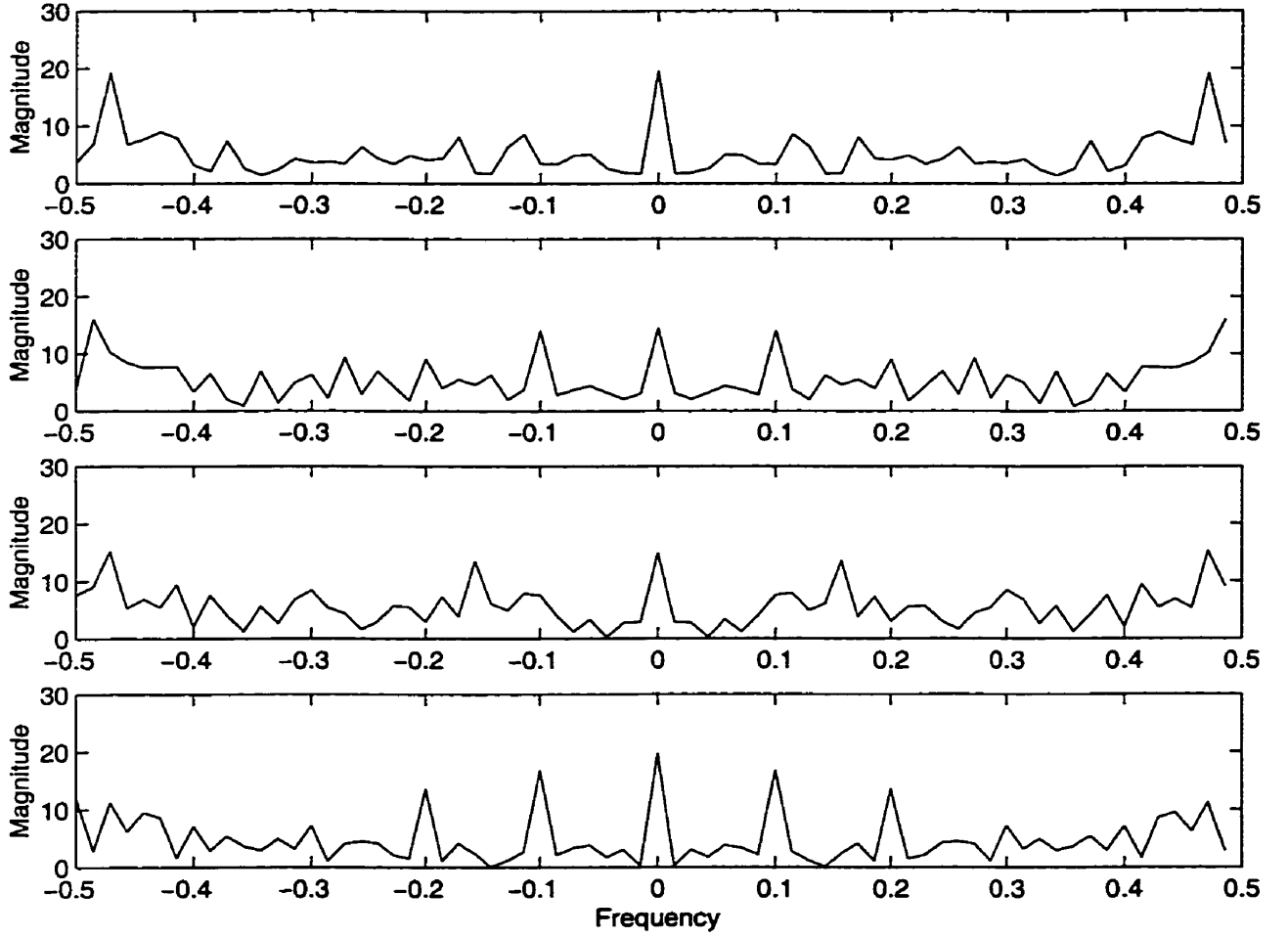
(b) DFT of segments of the chaotic Henon map

Figure 6.6: Comparison of the DFT of a periodic Henon map (a = 1.42207) time series from which the detection algorithm accurately detected periodicity with four chaotic time series DFTs of the Henon map (a = 1.4).

6.3.4 Investigation 2: An extended test of the detection algorithm

We have seen how the detection algorithm works in the detection of a single incidence of rhythmicity in the Henon map. It remains to be shown that this detection strategy is applicable to situations where the system, $\mathcal{F}$ repeatedly slips into and out of periodic activity.

Using the $t = 15$ detection threshold, we run the Henon map with the detection algorithm for 1×10^4 time steps. In that time, the parameter a is alternated between the chaotic value of $a = 1.4$ (120 time steps) and the periodic value of $a = 1.42207$ (360 time steps).

Figure 6.7 illustrates the time series of the extended test of the detection algorithm. It is interesting to note that the Henon map slipped into the periodic activity at irregular intervals from the moment a was switched from $a = 1.4$ to $a = 1.42207$. On occasion, the dynamics remain chaotic throughout the entire $a = 1.42207$ interval.

Figure 6.8 shows the evolution of t with time over the 1×10^4 time steps of the extended test. The peaks of t correspond well with the moments of periodic activity of the Henon map.

The extended test reveals that the detection algorithm is able to detect rhythmicity with a fair amount of reliability. Throughout the course of the 1×10^4 step computation, no false positives and no undetected periodicities are observed.
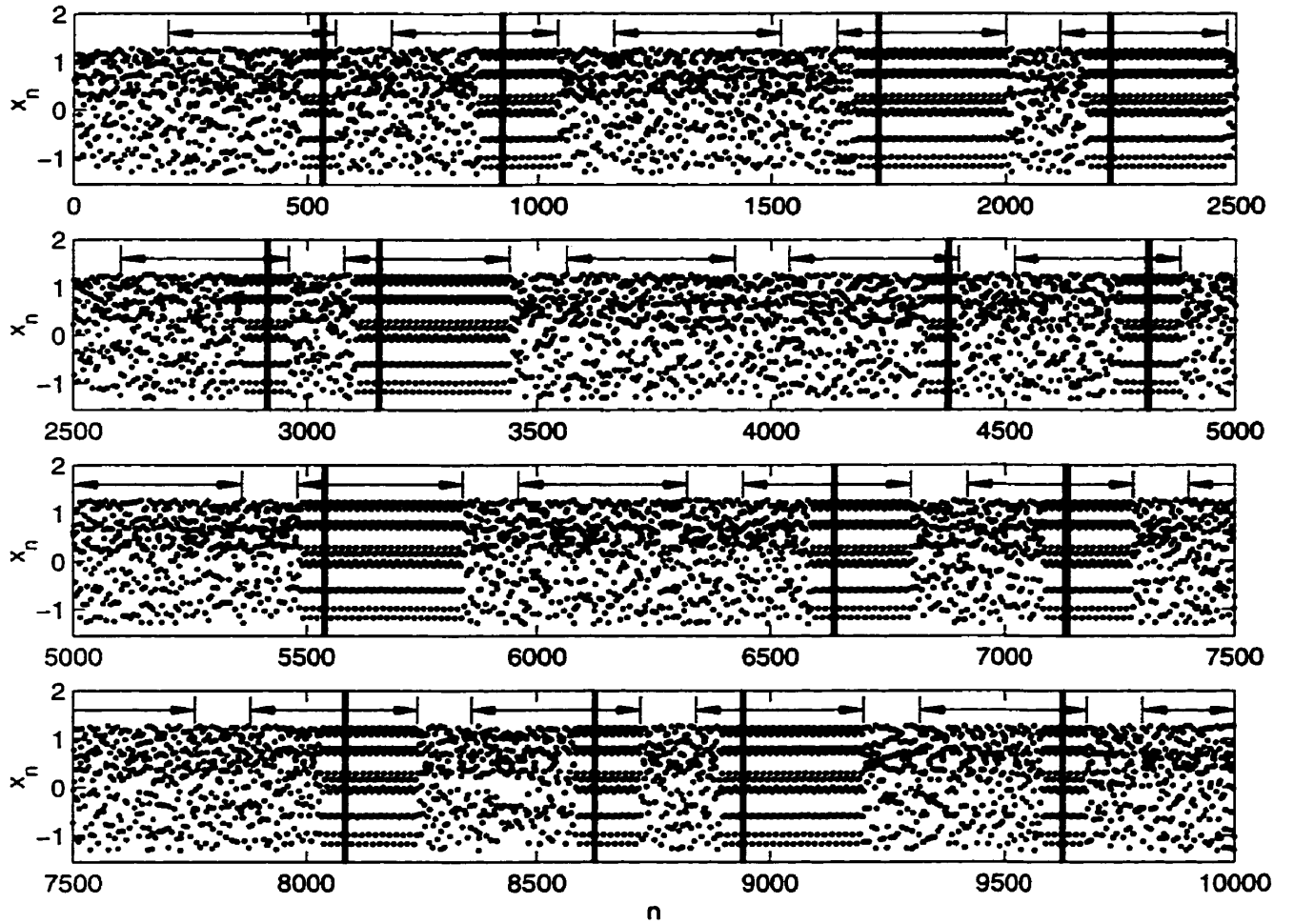
Figure 6.7: *Extended test of the detection algorithm on the Henon map. The parameter a = 1.42207 during segments of time 360 time steps long (*the time between the arrows*) and a = 1.4 at all other times. The* thick vertical lines *indicate the times at which the detection algorithm signals rhythmicity. Note the variability in the time between the switching to the periodic value of a (a = 1.42207) and the periodic behaviour of the Henon map.*

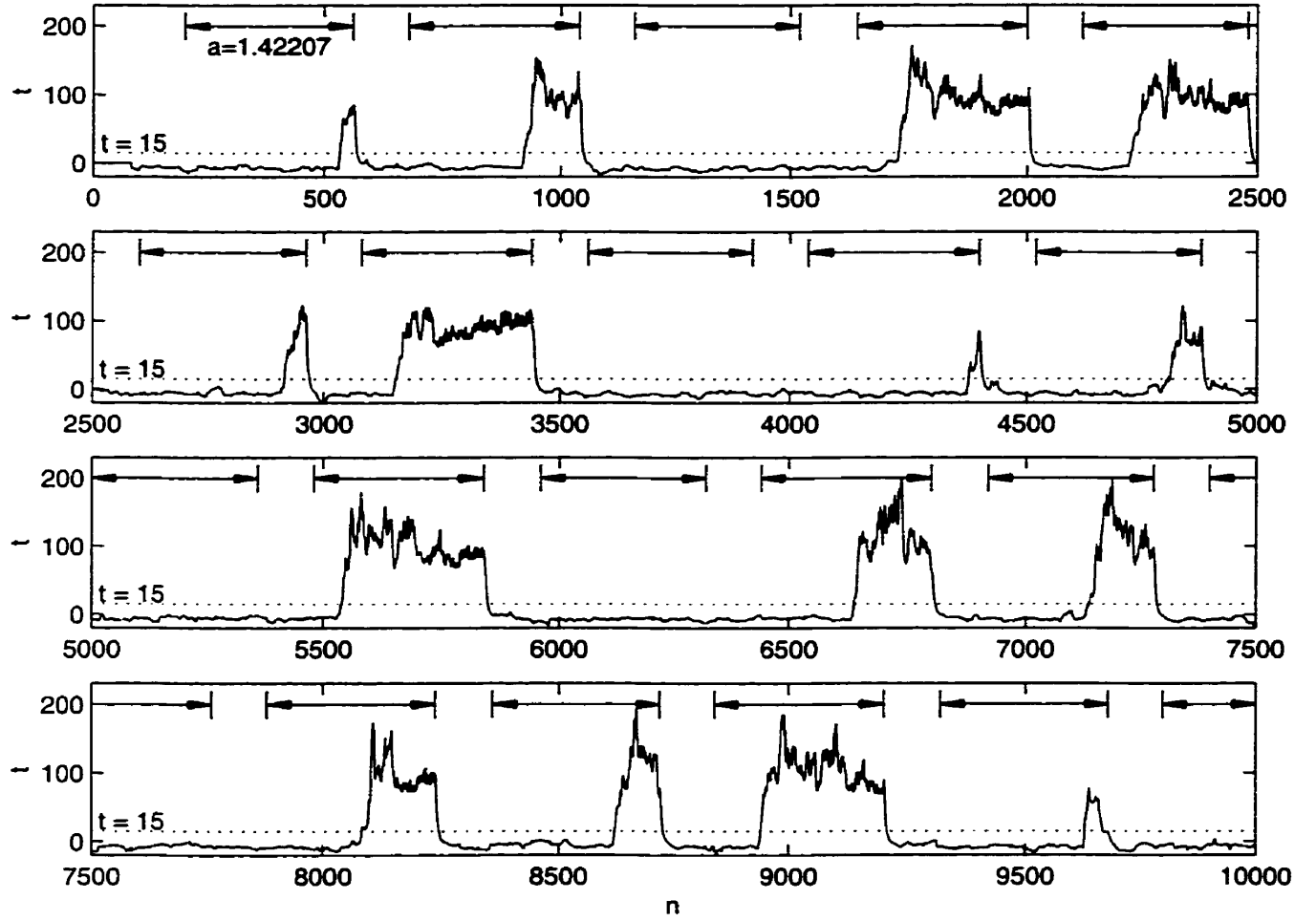**Figure 6.8:** *Plot of t as a function of time for the time series depicted in Figure 6.7. The dotted line illustrates the t = 15 threshold for detection. The parameter a = 1.42207 during segments of time 360 time steps long (the time between the arrows) and a = 1.4 at all other times.*

Parameter	Symbol	Value
side of small box in state space	ϵ	0.1
size of moving window	$\mathcal{N}$	75
number of elements in δn	$L(\delta n)$	10
number of elements in Δn	$\mathcal{M}$	25
theshold	t_α	2.5

Table 6.2: *The detection algorithm parameter values for the application to the MCO model.*

6.4 Application to the MCO model

We demonstrate the application of the detection algorithm to the problem of detecting rhythmicity in the mapped clock oscillator model. We will attempt to detect the rhythmic activity associated with the small parameter change from $a_{01} = -54.5226$ to $a_{01} = -54.7726$.

6.4.1 Initializing the Detection Algorithm

Table 6.2 shows the values of the detection algorithm parameters selected for the application to the MCO model. As with the Henon map, the choice of window size, $\mathcal{N} = 75$, is motivated by a desire to ensure that there is always at least one pair of ϵ-neighbours. For the MCO model, we use a detection threshold of $t_\alpha = 2.5$.

6.4.2 Detecting Rhythmicity in the MCO

Here we investigate the ability of the detection algorithm to resolve instances of rhythmic dynamics in the interspike interval of the intermittent MCO model. We switch to the intermittent dynamic of the MCO model at $n = 66$, when a_{01} is switched to $a_{01} = -54.7726$. The RBF model of section 5.6 trained on the MCO model is used in this application of the detection algorithm.

Figure 6.9 depicts the time series of the intermittent MCO interspike interval. The figure shows that the rhythmic activity dominates the intermittent dynamics of the MCO model. The two large periods of rhythmicity which were both detected. The last brief period of rhythmic dynamics (at $n = 950$) was not detected.
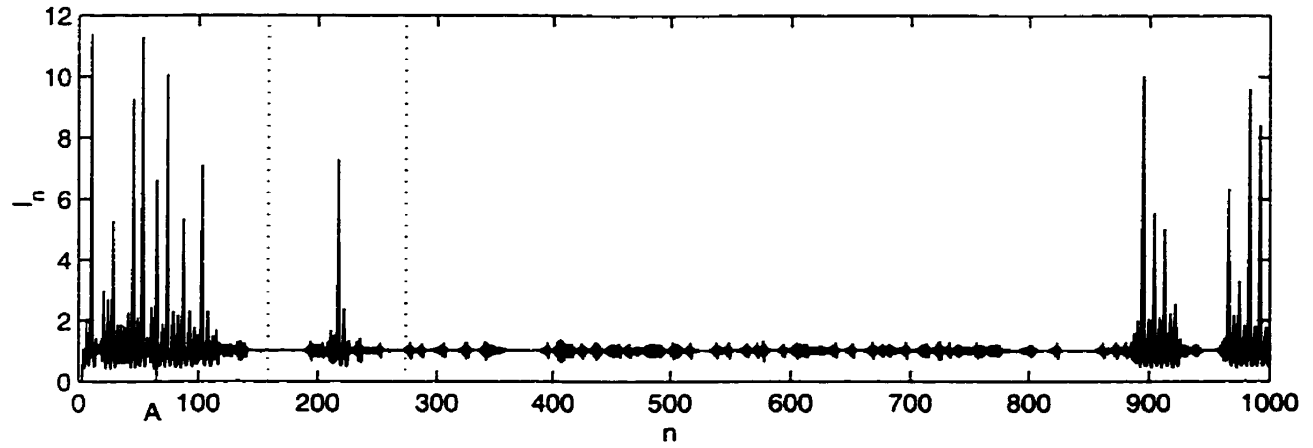
Figure 6.9: *The MCO interspike interval (I) time series. The intermittent dynamics begin at $n = 66$ (denoted: A). There were two detections of rhythmicity (dotted line).*

Corresponding to the the time series of Figure 6.9, Figure 6.10 illustrates the evolution of t with time, n. Rhythmicity detection occurs at the point where t crosses the threshold $t_\alpha = 2.5$.
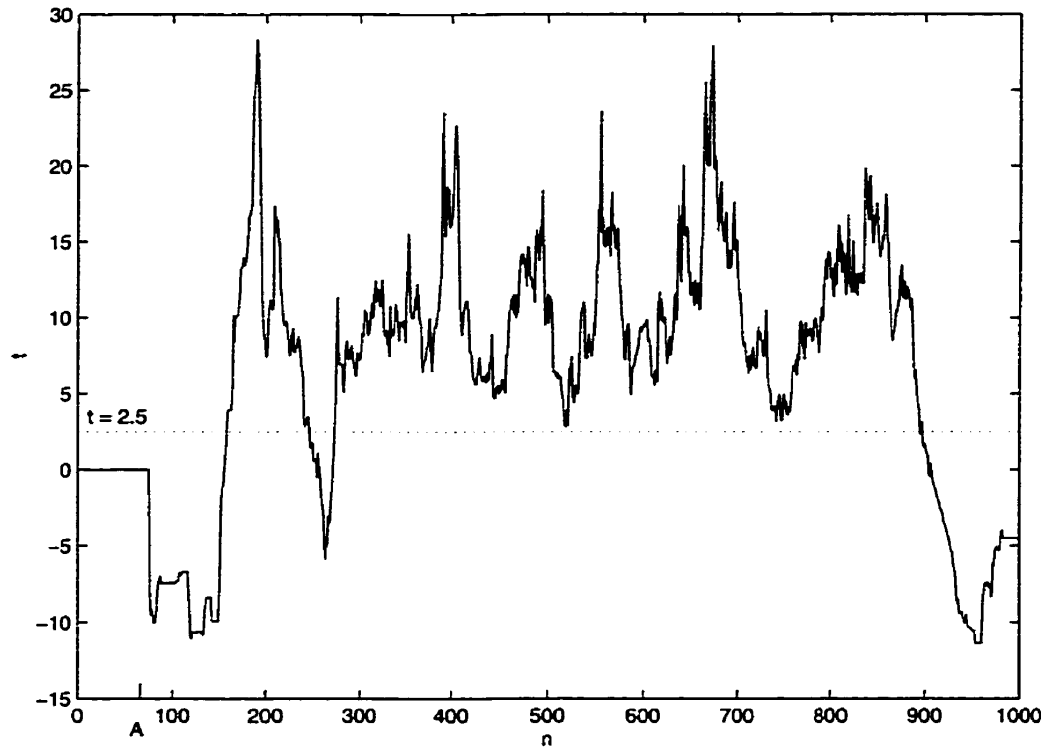
Figure 6.10: *The evolution of t corresponding to the time series of the intermittent MCO model (Figure 6.9). The intermittent dynamics begin at n = 66 (*denoted: A*)*

Chapter 7

Making Chaos

In this chapter we will develop the strategy by which chaotic activity will be restored to the subject system, $\mathcal{F}$ where rhythmic activity has been detected.

We require an algorithm capable of determining the precise timing of a stimulus which will throw the system, $\mathcal{F}$, back to a chaotic mode of operation. Following the arguments of Christini *et al.* [49], our goal is to design a control algorithm to interact with physiological systems with emphasis on reducing the number of stimuli given to the physiological system.

7.1 Control Algorithm

Our control algorithm takes inspiration from the targeting algorithm developed by Shinbrot *et al.* [42]. Their targeting technique perturbs the trajectory of a chaotic system onto the stable manifold of some target position in state space. By placing the trajectory on the stable manifold, the targeting algorithm uses the system's own dynamics to reach the target. Our approach is to do the opposite, we wish to perturb the trajectory of our system, $\mathcal{F}$, on to the unstable manifold of the periodic orbit in which the trajectory is stuck and thereby restore the chaotic activity through the natural autonomous dynamics of the system.

7.1.1 Estimating The Unstable Manifold

We estimate the unstable manifold of the periodic orbit of $\mathcal{F}$ by iterating the rRBF model of $\mathcal{F}$ for a population of trajectories from a region of state space on the periodic orbit of

89

$\mathcal{F}$. In practice, we start the iteration procedure with a population of trajectories positioned within an ϵ-neighbourhood of the point in state space where rhythmicity was detected.

The population of trajectories is iterated through the rRBF model until they from an image of the entire chaotic attractor. Figure 7.1 illustrates the first few iterations of the rRBF model of the unstable manifold of the Henon map. The SDIC property of chaotic systems spreads the population of points until they cover the entire attractor.

Our approximation of the unstable manifold of the periodic orbit of $\mathcal{F}$, is described by a series of vectors whose elements have been individually iterated from the rRBF model of $\mathcal{F}$. The set representing the approximation of the unstable manifold. $\eta_{\mathcal{F}}^u$, is given by

$$\hat{\eta}_{\mathcal{F}}^u = \left\{ \hat{\boldsymbol{y}}_n \in \Re^m, \left| \hat{\boldsymbol{y}}_{m-1} \in \mathcal{U}_{\mathcal{F}_p^\star}, \hat{y}_{n+1} = \sum_{i=0}^{N} w_i \phi_i(\hat{\boldsymbol{y}}_n) \text{ for } m \le n \le N_{\eta_{\mathcal{F}}^u} \right. \right\}, \qquad (7.1)$$

where $\hat{\boldsymbol{y}}_n = [\; \hat{y}_{n-(m-1)} \quad \hat{y}_{n-(m-2)} \quad \cdots \quad \hat{y}_n \;]^T$ corresponds to a vector of the RBF model output from times $n - m$ to $n - 1$. $N_{\nu_{\mathcal{F}}^u} - (m-1)$ is the number of interactions in the unstable manifold estimate and $\mathcal{U}_{\mathcal{F}_p^\star}$ refers to a set of m-dimensional vectors within an ϵ-neighbourhood of the periodic orbit.

7.1.2 Timing The Stimulus

Once the approximation of the unstable manifold, $\hat{\eta}_{\mathcal{F}}^u$, is determined according to equation 7.1, the trajectory of $\mathcal{F}_p$ must be perturbed in order to intercept the manifold. Since we have no access to the system parameters, the perturbation must take the form of placement of the system variable, $\hat{x}_n$. In applications to biological neuronal networks with an interspike interval embedding, the variable placement would correspond to an appropriately timed, stimulus induced, action potential.

In the absence of stimulation, neurons fire action potentials spontaneously. If we assume that we cannot suppress the spontaneous neuronal activity, then we are limited by the time of the next spontaneous action potential. We encorporate this limitation into the control strategy by specifying that the perturbed variable must be less than the predicted value. This restriction corresponds to illiciting an action potential which shortens the interspike interval when compared to that of the predicted spontaneous activity.

The control strategy is to wait until we are able to place the trajectory of $\mathcal{F}$ on $\hat{\eta}_{\mathcal{F}}^u$

with a single variable placement. This opportunity presents itself when two criteria are satisfied. The first criteria is that the current state of $\mathcal{F}_p$, x_n, and all the past values back to $x_{n-(m-2)}$ are all within an ϵ-neighbourhood of the $m-1$ consecutive values of one of the vectors comprising an estimate of the unstable manifold, say $\hat{y}_j$,

$$\left\| \begin{bmatrix} x_{n-(m-2)} \\ \vdots \\ x_n \end{bmatrix} - \begin{bmatrix} \hat{y}_{j-(m-1)} \\ \vdots \\ \hat{y}_{j-1} \end{bmatrix} \right\| < \begin{bmatrix} \epsilon \\ \vdots \\ \epsilon \end{bmatrix} \quad \text{and } \hat{y}_j \in \hat{\eta}_{\mathcal{F}}^u, \tag{7.2}$$

where $\hat{y}_j = [\ y_{j-(m-1)} \quad y_{j-(m-2)} \quad \cdots \quad y_j\ ]^T$. The second criteria is that remaining element of the vector $\hat{y}_j$, i.e. element $\hat{y}_j$, satisfy

$$\hat{y}_j < \sum_{i=0}^{N} w_i \phi_i(x_n) - \epsilon, \text{ where } z_n \in \mathcal{U}_{x_n}. \tag{7.3}$$

The last element in the unstable manifold vector, y_j, must be less than the next step of $\mathcal{F}$ predicted by the RBF model by an amount greater than some ϵ.

When the two criteria are satisfied, the control algorithm enables the placement of the discrete time variable x_{n+1} on the unstable manifold of the periodic orbit of F.

7.2 Application to the Henon Map

In Chapter 6, we saw that the detection algorithm was successful at detecting instances of rhythmicity in the Henon map. Here, we determine if the control strategy is equally effective at eliminating rhythmicity.

7.2.1 Methods

In applying the control algorithm to the Henon map we follow the procedure described in section 7.1 first, to estimate the unstable manifold of the periodic orbit that occurs in the Henon map when $a = 1.42207$, and then to determine the appropriate value for x_{n+1} to ensure that the next state vector, x_n, lands on the unstable manifold.

The unstable manifold estimation of the period-30 orbit is constructed using the 20 Gaussian basis function RBF model described in section 5.5.2. The unstable manifold was
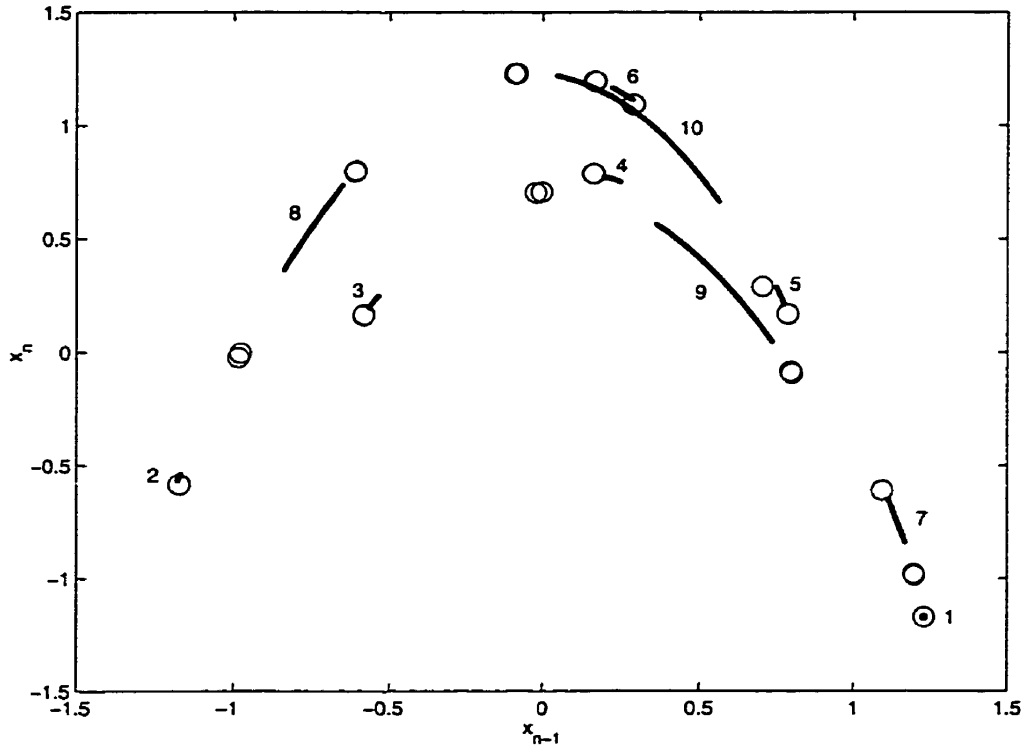
91

Figure 7.1: *The first 10 iterations of the rRBF model approximation of the unstable manifold of the Henon map (points) and the period-30 orbit of the Henon map with a = 1.42207 (open circles). Each iteration of the rRBF model contains 500 vectors. Note the growth of the manifold with each successive iteration, starting at the group of points labeled 1.*

estimated by iterating a population of 500 vectors from an ϵ-neighbourhood, $\epsilon = 0.01$, of the position along the periodic orbit that corresponds to the instant of detection. The population is iterated 25 times, at which point the 500 points are dispersed over the entire Chaotic Henon attractor. Figure 7.1 illustrates the first 10 iterations of the RBF model in estimating the unstable manifold of the Henon map periodic orbit. The iterations start from the position labeled 1, in Figure 7.1, within a box of side 0.01 centered around one iteration of the periodic orbit represented by the circle surrounding the concentrated population of vectors.

Once we obtain an estimate of the unstable manifold, we wait until the placement of the variable x_{n+1} results in the next state vector, x_n, landing on the unstable manifold. When an appropriate moment arises the value of x_{n+1} is simply set to the value corresponding to the unstable manifold placement. After the perturbation of x_{n+1}, the control algorithm enters a

refractory period lasting 20 iterations of the Henon map, in which time the control algorithm does not respond to a positive detection of rhythmicity. The refractory period allows the detection algorithm to respond to the effect of the control action. If the detection algorithm indicates a positive detection of rhythmicity after the refractory period has expired, then the control algorithm begins the process anew, including re-estimating the unstable manifold of the periodic orbit.

7.2.2 Results

We apply the control algorithm to the situation illustrated in Figure 7.2 (a). Figure 7.2 (b) shows the result of the control action which occurred immediately after detection. Until the instant of detection, the time series of Figure 7.2 (a) and (b) are identical. Figure 7.2 clearly shows that the application of the control algorithm successfully restores the chaotic transient. Figure 7.3 offers an alternative representation of the Henon map under control. In this figure, the lines connecting the individual points in the time series are removed, allowing one to more easily see the incidences of periodicity in the Henon map. Not shown in either Figures 7.2 or 7.3 is the time when the chaotic transient ends and the periodic orbit is re-established.

Figure 7.4 shows the evolution of the detection variable t, corresponding to the time series shown in Figures 7.2 and 7.3. The figure illustrates the response of the quantity t to the control action. As expected, once the chaotic transient is re-established, t drops rapidly to values comparable to those before the onset of periodic activity.

We have seen how the control algorithm is effective at restores the chaotic transient in a single execution of the control algorithms. The question remains: how effective are they at reducing the amount of time spent in the periodic orbit of the Henon map with $a = 1.42207$? To address this question, we extend the simulation of the Henon map shown in Figures 7.2 and 7.3, to $n = 1 \times 10^4$.

The results the extended test of the control algorithm are depicted in the time series in Figure 7.5. This figure shows that over the 1×10^4 iterations of the periodic Henon map, the dynamics slipped into periodic activity 20 times. Each time, the control algorithm acted to re-establish the chaotic trasient by placing the next state vector, x_n, on to the unstable
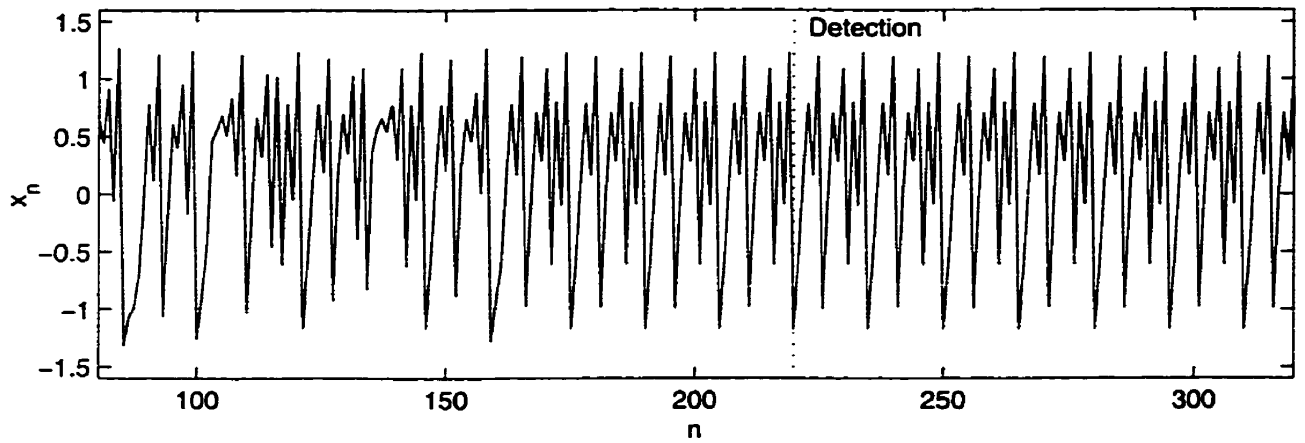
(a) Without control
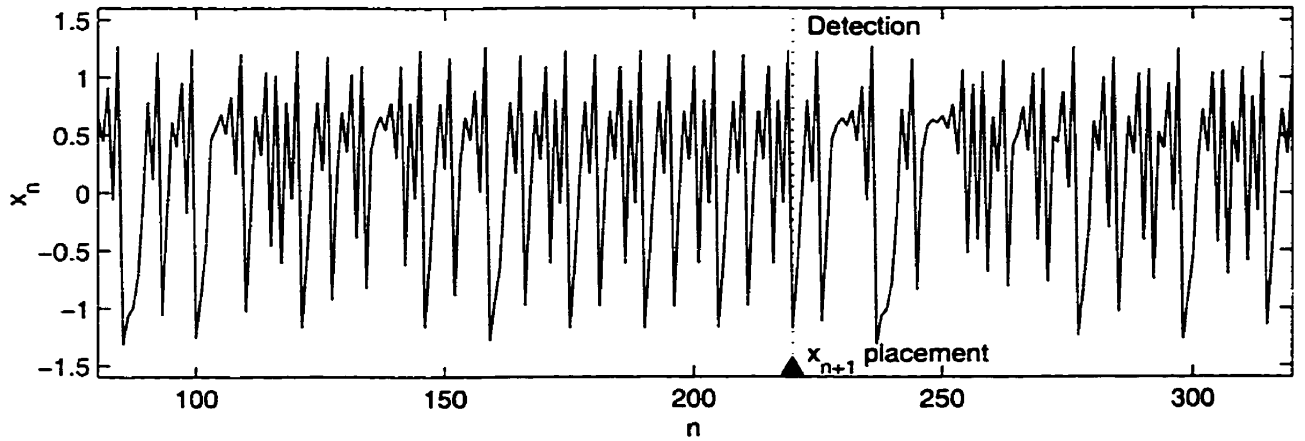
(b) With control

Figure 7.2: *Time series of the Henon map from $n = 80$ to $n = 320$. Rhythmicity was detected at $n = 220$ (dotted line). In (b) x_{n+1} placement was initiated immediately (triangular marker). The parameter a was switched from $a = 1.4$ (chaotic) to $a = 1.42207$ (periodic) at $n = 70$.*
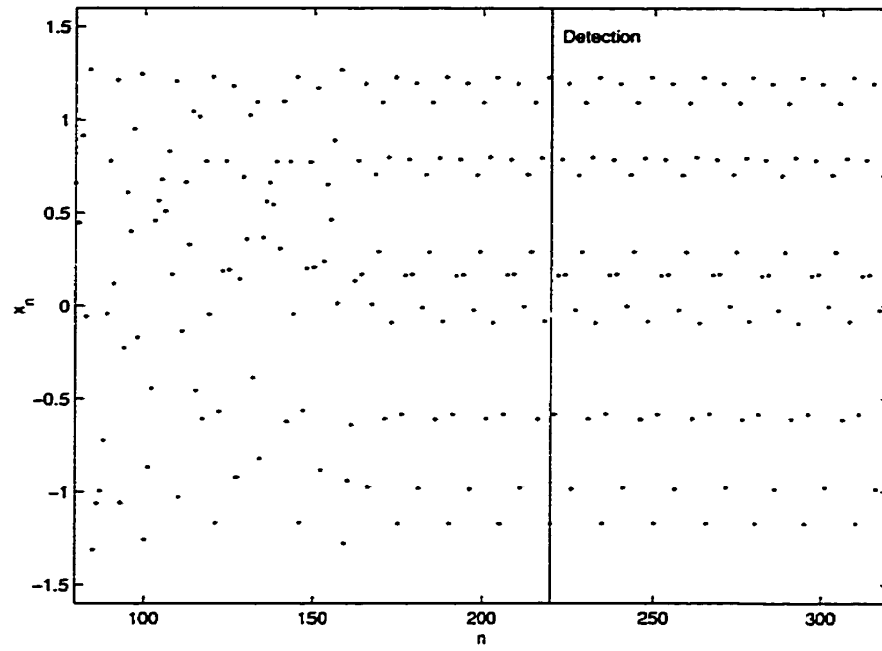
(a) Without control
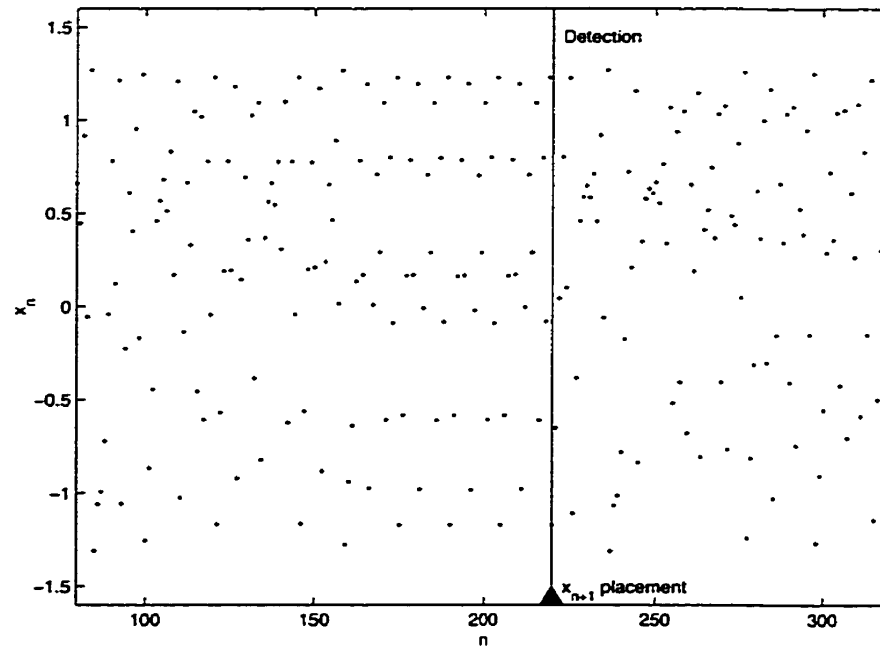
(b) With control

Figure 7.3: *Disconnected Time series of the Henon map from $n = 80$ to $n = 320$. Rhythmicity was detected at $n = 220$ (dotted line). In (b) x_{n+1} placement was initiated immediately (triangular marker). The parameter a was switched from $a = 1.4$ (chaotic) to $a = 1.42207$ (periodic) at $n = 70$.*

95
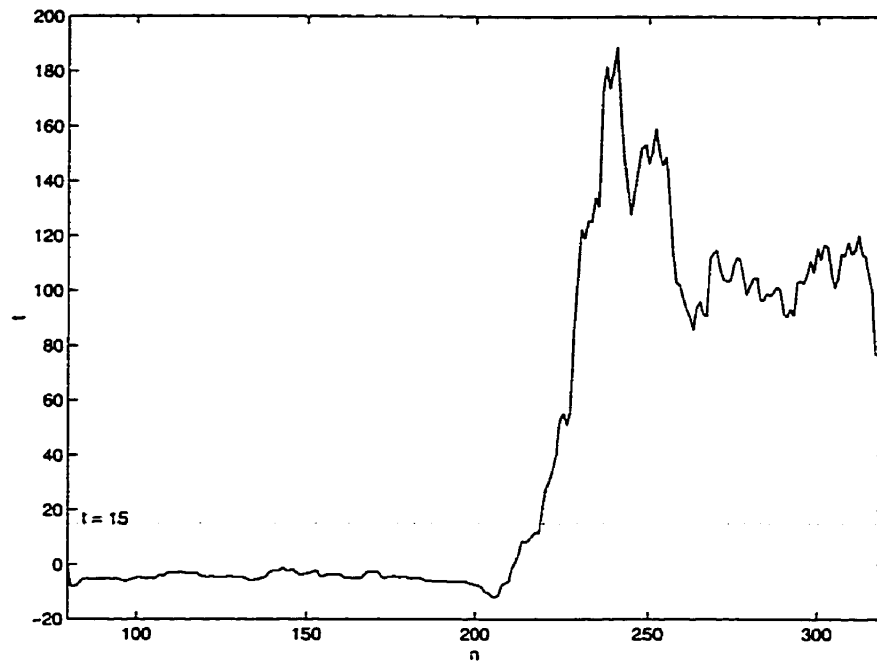
(a) Without control
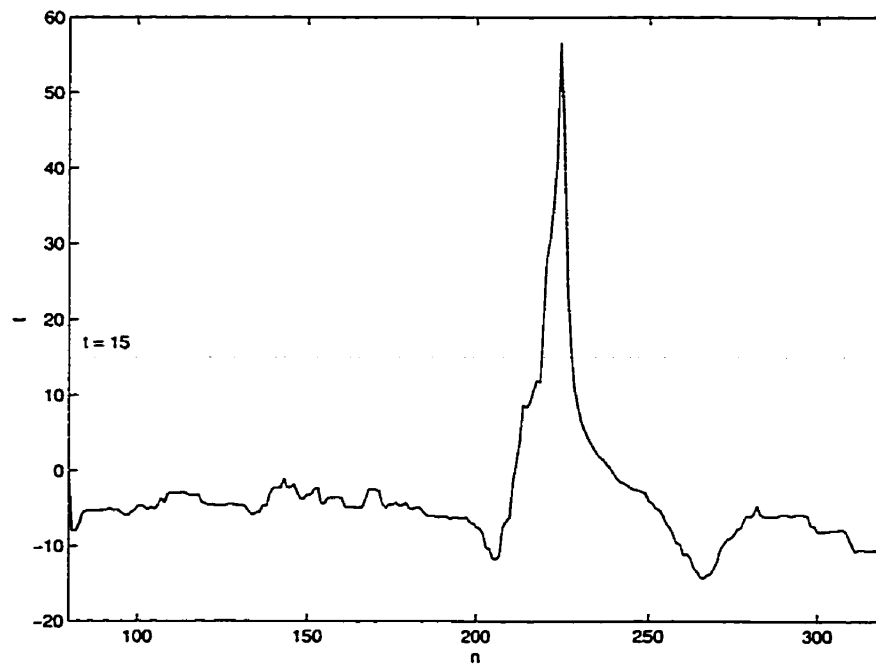
(b) With control

Figure 7.4: *The evolution of t of the Henon map from n = 80 to n = 320. t past the t = 15 threshold* (dotted horizontal line) *at n = 220, indicates a positive detection of rhythmicity. As illustrated in* (b), *once control is successfully initiated at n = 220, t returns to subthreshold values.*

96

manifold with varying degrees of success. Several of the control actions are very successful in the sense that they induce chaotic transients which remain over a long period of time before the periodic activity returns. Other control actions, such as those occurring between $n = 3500$ and $n = 3750$ and between $n = 6500$ and $n = 6750$, evoke relatively short lived transients before the restoration of the periodic activity. The variety in the duration of transients observed in Figure 7.5 is reminiscent of the variability in the times of entry into the periodic orbit after switching a from $a = 1.4$ to $a = 1.42207$, illustrated in Figure 6.7.

Figure 7.6 presents the evolution of t during the extended run of the Henon map given in Figure 7.5. The plot of t shows that the $t = 15$ detection threshold is quickly met and surpassed at corresponding instances of periodicity (shown in Figure 7.5). Following the control action, the value of t rapidly drops below threshold where it remains until the periodic orbit is regained.

A careful study of Figure 7.5 reveals an interesting occurrence between $n = 900$ and $n = 1000$. For a brief moment, it seems as though the Henon map has, once again, slipped into periodicity but then suddenly returns to the chaotic transient behaviour spontaneously without the detection algorithm ever indicating rhythmicity. Figure 7.7 presents a closer look at this event. From the time series given in Figure 7.7 (a) the Henon map seems quite clearly stuck in the periodic mode, yet our comparator t remains unconvinced as shown in (b) of Figure 7.7. Events such as this, where the trajectory skirts the outside of the periodic orbit before leaving it, motivated the use of the conservative $t = 15$ threshold for detection. In line with our policy of minimal interference, our conservative detection criteria initiates a control action as a last resort.

As a final look at the maintenance of chaos in the periodic Henon map, Figure 7.8 present a comparison of the identical simulation with and without control. The dramatic difference between the plots given in (a) and (b) is the result of 20 control actions over the entire 10000 time steps. Here we see the combined efforts of the detection and control algorithms to break the periodicity of the autonomous running Henon map over and over again through an almost insignificant amount of control action. Under control, the Henon map ran autonomously for 99.8% of the simulation. Despite the small control effort, influencing the Henon map only 0.2% of the time, the control algorithm achieved significant increase in the chaotic activity of the Henon map.
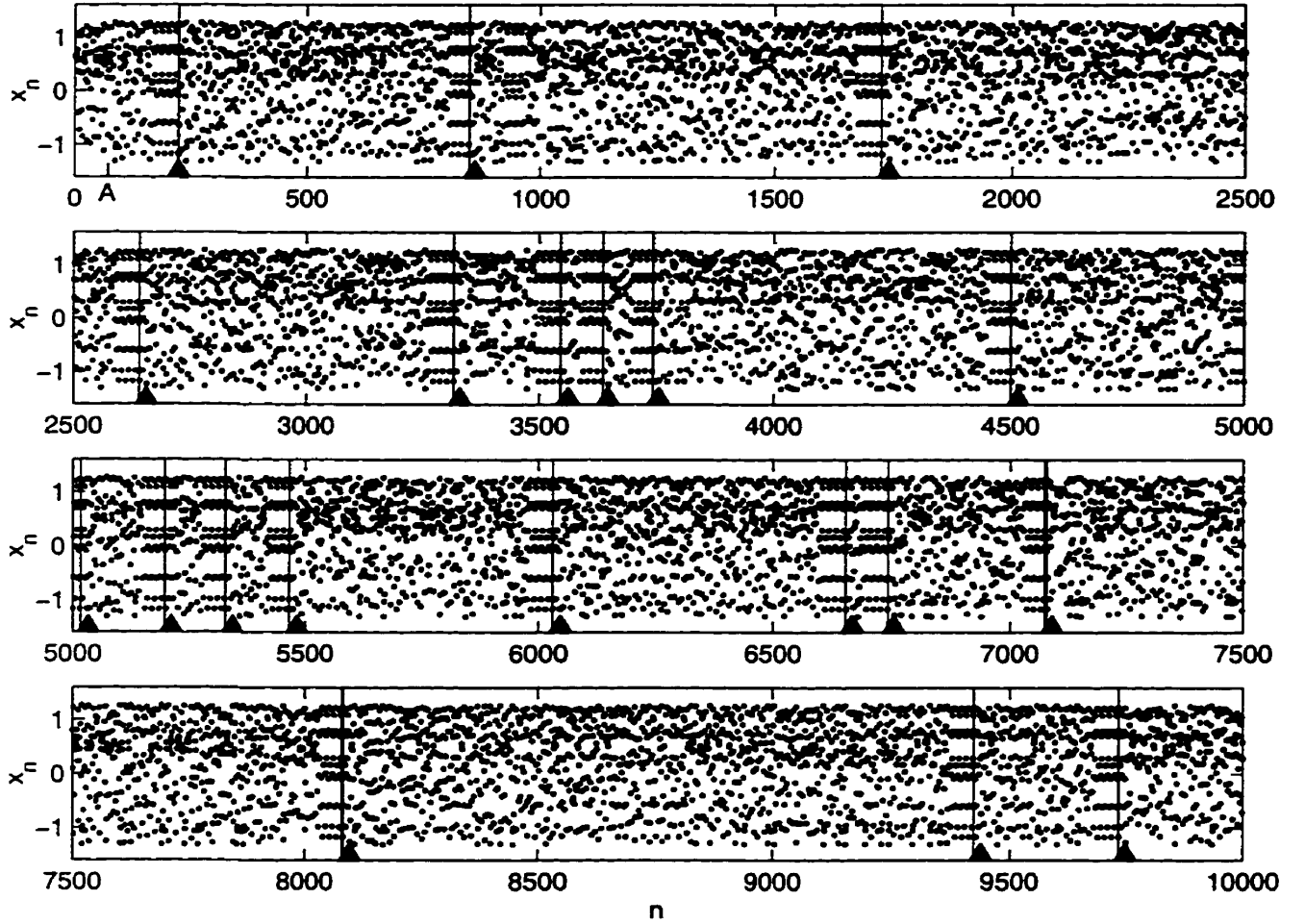
Figure 7.5: Extended Time series of the Henon map with control from $n = 0$ to $n = 10000$. The parameter a is changed from $a = 1.4$ to $a = 1.42207$ at $n = 70$ (marked: A). When the Henon map slips into periodic activity, it is detected shortly after (solid vertical line) and x_{n+1} placement ensues (triangular marker).
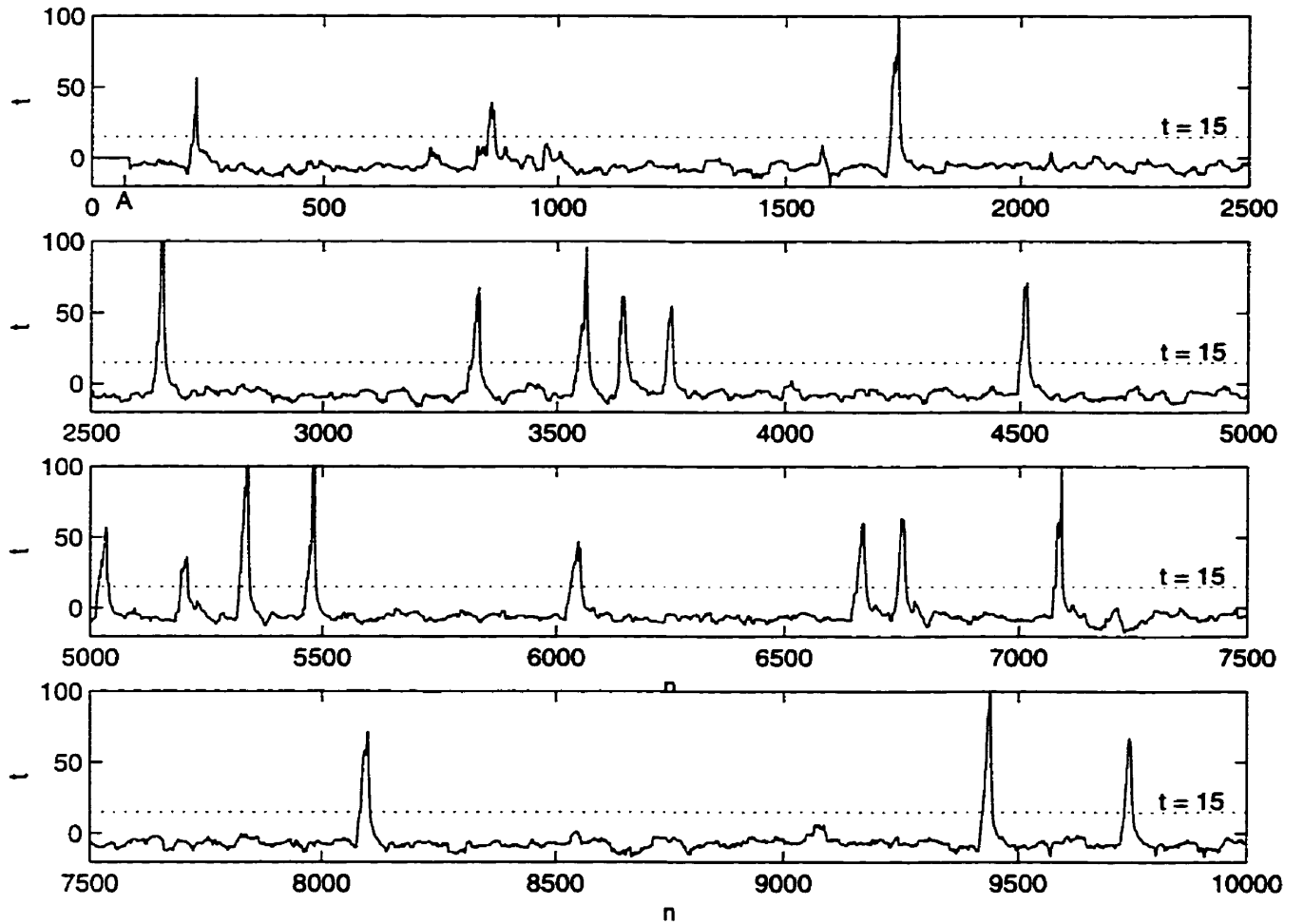
Figure 7.6: *The evolution of t of the Henon map with control from $n = 0$ to $n = 10000$. When t is above the $t = 15$ threshold* (dotted line), *the detection algorithm indicates a positive detection of rhythmicity. The parameter a is changed from $a = 1.4$ to $a = 1.42207$ at $n = 70$* (marked: A).
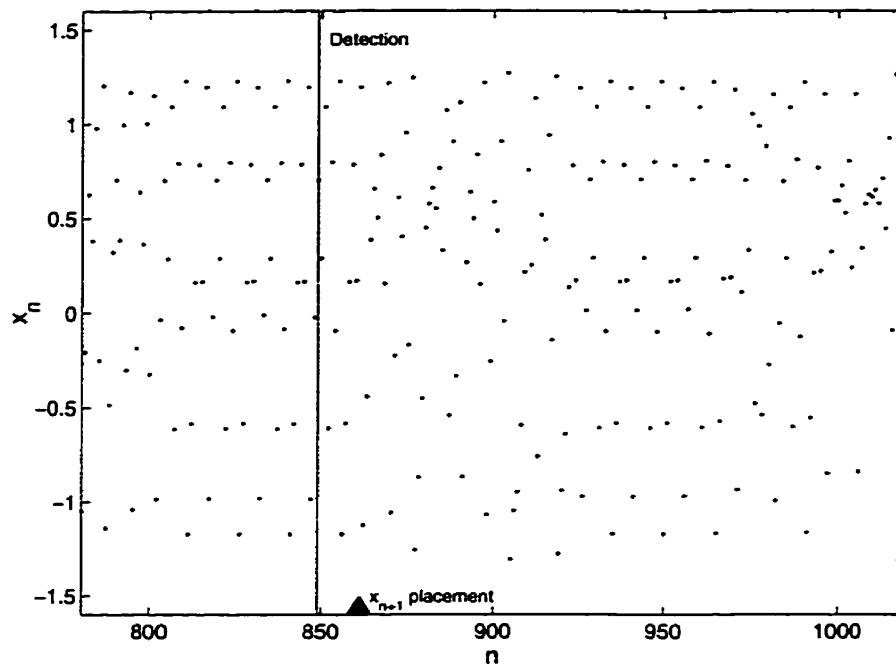
(a) Time Series
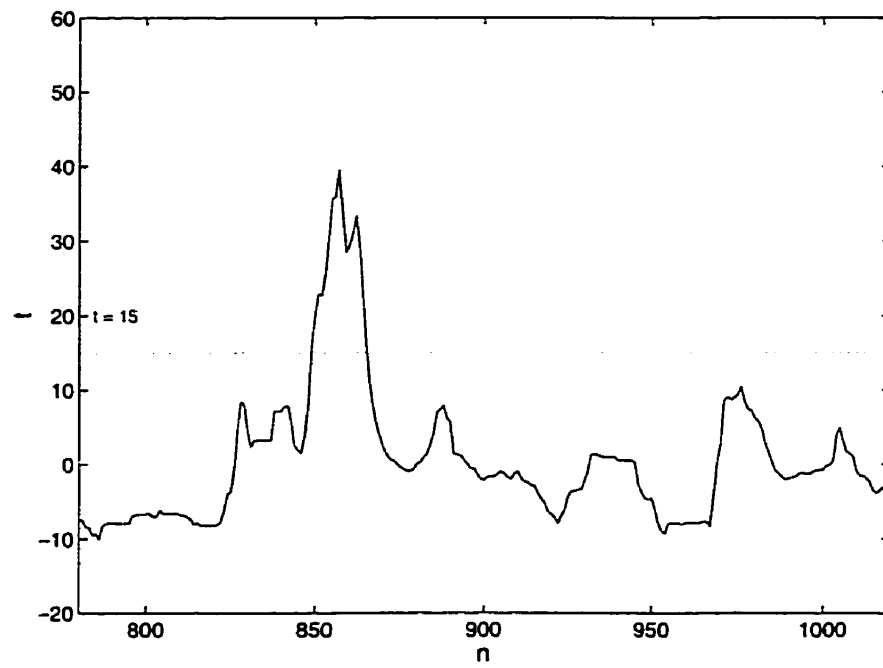
(b) Evolution of t

Figure 7.7: A segment of the time series of the Henon map (a) *under control and corresponding values of t* (b). *Note the rhythmic looking sequence between $n = 930$ and $n = 970$.*
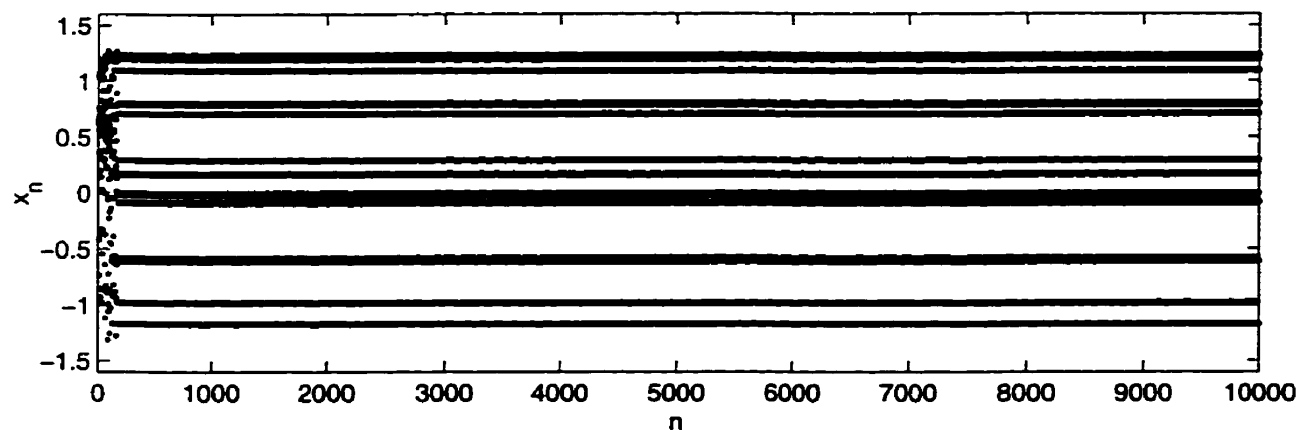
(a) Without control
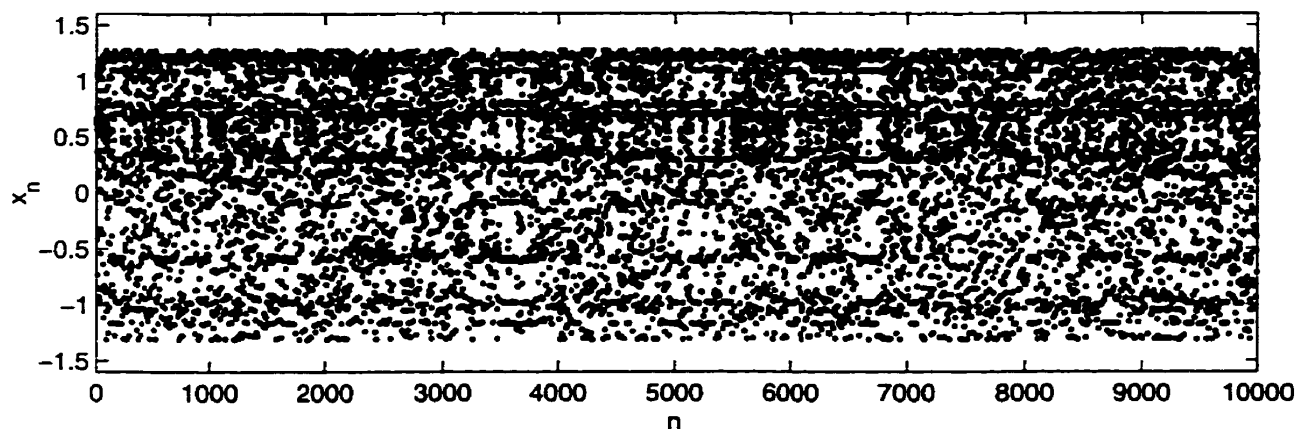
(b) With control

Figure 7.8: *Comparison of identical Henon map time series* (a) *without control and* (b) *with control.* *At* $n = 70$ *the parameter* a *switches from* $a = 1.4$ *to* $a = 1.42207$ *where it remains until* $n = 10000$.

7.3 Application to the MCO model

In this section, the control strategy is applied to the mapped clock oscillator (MCO) model. The intermittent MCO dynamics are dominated by a near period-1 orbit. We wish to determine to what extent the control algorithm is successful at restoring chaotic dynamics in the intermittent subject system.

7.3.1 Methods

The application of the control algorithm to the MCO model, once again, follows the procedure described in section 7.1. The unstable manifold is estimated by iterating the rRBF model of the MCO model (described in section 5.6) from the point of rhythmicity detection. The estimate consists of 30 iterations of 700 vectors within a an ϵ-neighbourhood ($\epsilon = 0.01$) of the state vector corresponding to the detection of rhythmicity.

After obtaining an estimate of the unstable manifold, the control strategy is to wait until the placement of the variable I_{n+1} results in the next state vector, I_n, landing on the unstable manifold. The application of the variable placement to the MCO model is not as simple as setting the next variable equal to the value corresponding to the unstable manifold. The interspike interval encoding of the MCO dynamics is only mapping from continuous time to a discrete time representation, so the control action must act on the continuous time dynamics. In the MCO model, the control action is initiated by blocking all stimulation from oscillator 2 to oscillator 1 (see Figure 2.9) for one period of oscillation and setting the intrinsic frequency parameter of oscillator 1, ω_1, such that one period (peak to peak) is equal to interspike interval (I) corresponding to a placement on the unstable manifold,

$$\omega_1 = 2\pi I_{n+1}^d. \tag{7.4}$$

The term I_{n+1}^d represents the desired placement of the interspike interval at the next time step, $n+1$. After the perturbation of I_{n+1}, control actions are blocked for a refractory period lasting 30 interspike intervals of the MCO model.

7.3.2 Results

The application of the control algorithm to the intermittent MCO model is given in Figure 7.9. The figure shows that the majority of the control actions were able to restore chaotic activity albeit briefly. The evolution of the detection algorithm comparator, t is given in Figure 7.10. The value of t seems to follow the action of the dynamics of the MCO model as they change through the action of the control algorithm. At approximately $n = 450$ the detection algorithm signals a detection of rhythmicity during activity which is not the nearly period-1 activity that dominates the MCO intermittent dynamic. As a result, the control algorithm initiates a perturbation soon after detection.

Towards the end of the time series, in the range of $n = 690$ to $n = 830$, there is an extended period of rhythmic activity over which no control action is given. A positive detection was indicated relatively early in the sequence; however, the control algorithm waited for over 100 time steps before initiating a control action. The algorithm waits until a single placement of I_{n+1} results in the placement of the state vector on the estimate of the unstable manifold. In this case, that criteria was difficult to match.

Just before $n = 200$ a control action was given to the MCO model which had little effect. Figure 7.11 shows the MCO output for the ineffective control action. These results are similar to those of the extended test of the control algorithm on the Henon map where we saw a number of variable placement attempts fail to initial a substantial chaotic transient Figure 7.12 shows the MCO output for a control action which successfully initiated chaotic activity.

The results from applying the control strategy to the intermittent MCO model indicate that, similar the periodic Henon map, we were able to restore temporary chaotic activity. Though the duration of the individual chaotic burst was typically small, the action of the control algorithm shortened the length of the longest rhythmic region from 650 time steps to approximately 150 time steps.

103
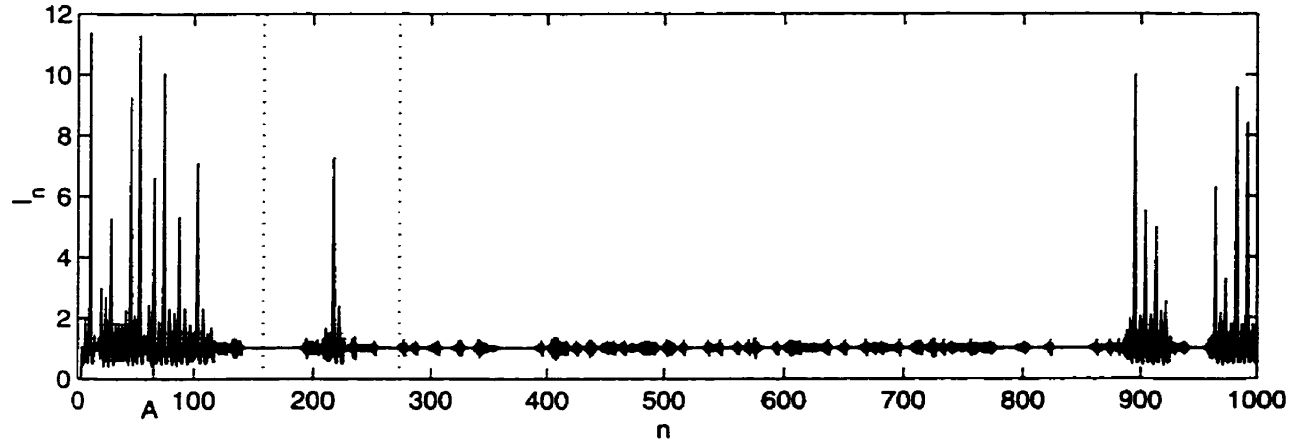
(a) Without control
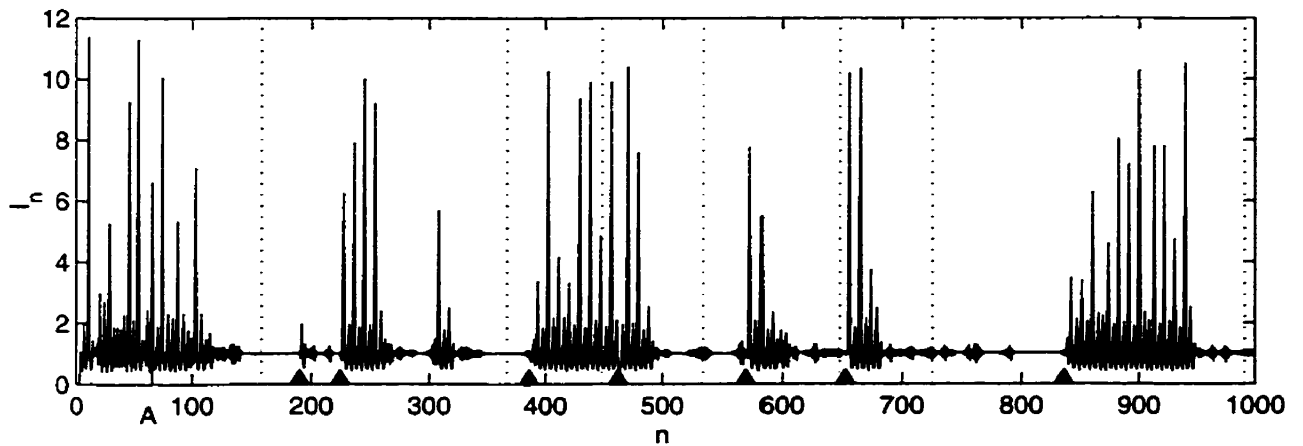
(b) With control

Figure 7.9: *The interspike interval of the MCO model in intermittent activity (a) and with the application of the control strategy (b). The* dotted lines *indicate the point where the detection algorithm signals a positive detection of rhythmicity. The solid triangles correspond to control actions. The MCO model enters the intermittent mode at* $n = 66$ *(*point A*) when* a_{01} *is changed from -54.5226 to 54.7726.*
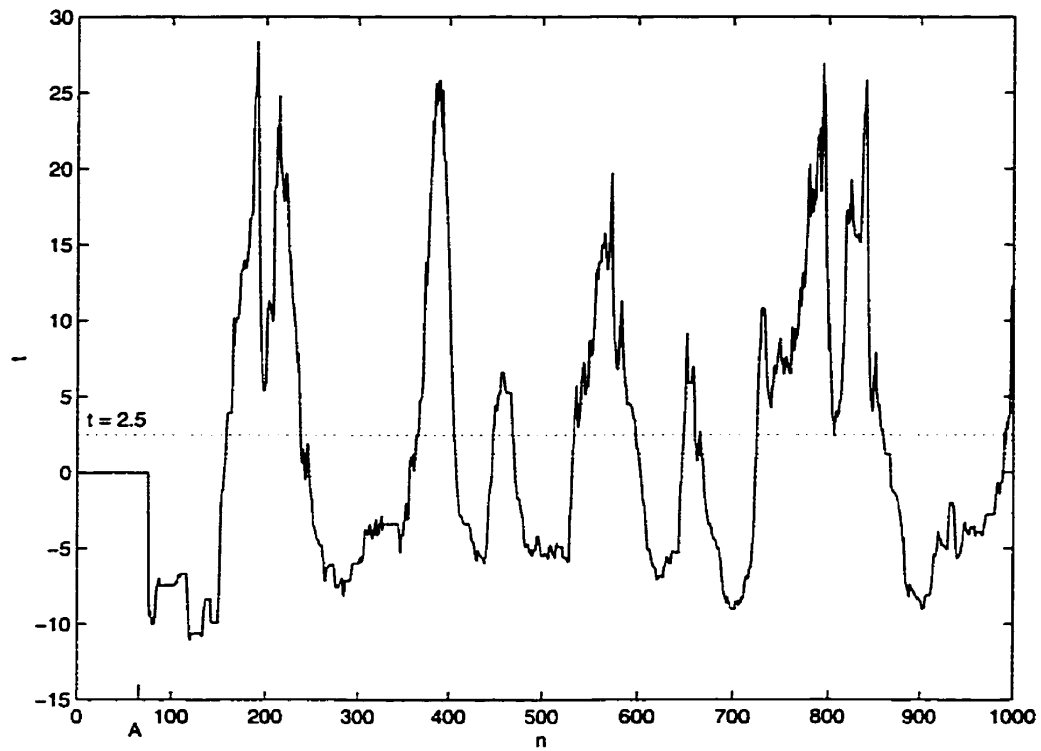
Figure 7.10: *The evolution of t for the intermittent MCO model under control. The MCO model enters the intermittent mode at $n = 66$ (point A) when a_{01} is changed from -54.5226 to 54.7726.*
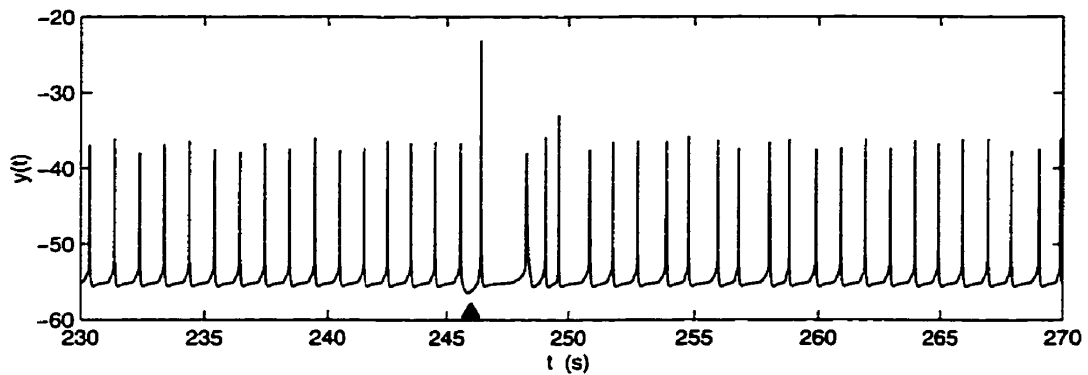
Figure 7.11: *The output of the MCO model for a failed control attempt.*
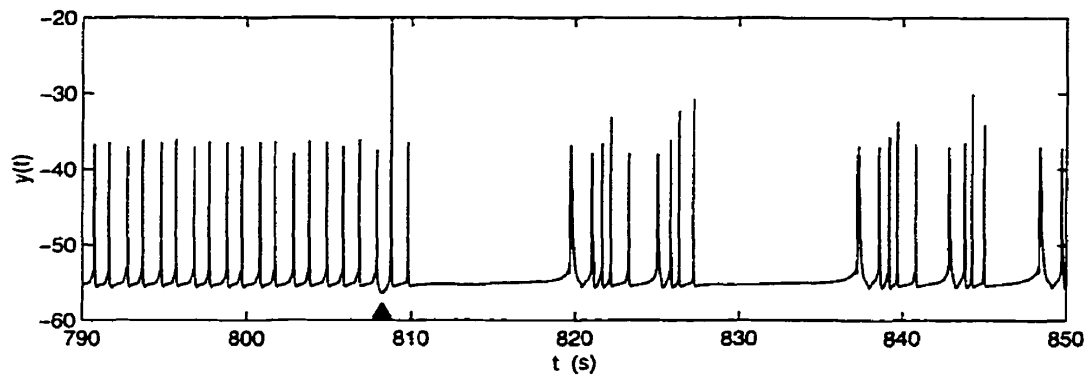
Figure 7.12: *The output of the MCO model for a successful control attempt.*

Chapter 8

Discussion and Future Work

In this concluding chapter, we discuss the results and implications of the thesis as a whole and revisit the key points which have emerged. We also compare the approach developed in the thesis to the those reviewed in Chapter 4. Next, the contributions of the thesis to the research community are summarized. Finally, we provide our conclusions and offer a brief discussion of directions for future work.

8.1 Discussion

8.1.1 RBF modelling of Chaotic dynamics

In Chapter 5, we investigated the possibility of learning chaotic dynamics from time series using radial basis function (RBF) models. We demonstrated the ability of the RBF model to learn chaotic dynamics in three versions of the Henon map time series: under ideal conditions, with noisy training data and with a small training set. The RBF model trained on noisy data and on few data points was able to capture details of the state space attractor that were not apparent from the training data. We also showed that the RBF model is able to capture the main features of the interspike interval dynamics from the four dimensional mapped clock oscillator (MCO) model.

Our approach to RBF parameter estimation includes both linear least squared optimization of the expansion coefficient, w_i, and a nonlinear optimization of the RBF parameters. The typical approach to parameter estimation is restricted to the linear optimization of

107

the expansion coefficient, w_i [4] [54]. As the plots in Figures 5.1 and 5.12 reveal, the inclusion of nonlinear optimization of the RBF parameters results in a substantial increase in the performance of the RBF model prediction. Even after the OLS algorithm chose an "optimal" choice of basis function centers for modelling the MCO dynamics, nonlinear optimization improved the prediction error by almost an order of magnitude. These results support our intuition that an optimization strategy which estimates all the model parameters is preferred over strategies which estimate a subset of these parameters.

The consequence of employing nonlinear optimization techniques is that we are faced with complex error surfaces which can be prohibitive to navigate to an adequate solution. Following the progress of the gradient descent algorithm in learning the MCO model dynamics (Figure 5.12), we see that often the prediction error would suddenly increase with the next epoch. These incidents are indications that the algorithm may not be able to follow the convolutions of the error surface. The gradient descent algorithm used in optimizing the radial basis function parameters is a relatively unsophisticated nonlinear optimization strategy. While it sufficed for application to our subject systems, we suggest that proceeding to applications of greater complexity would require a more principled approach to nonlinear optimization.

8.1.2 Detecting Transitions to Rhythmicity

In Chapter 6, we demonstrated the application of the detection algorithm to detect instances of rhythmicity in the Henon map and the MCO model. The value of t displayed significant changes in amplitude between the chaotic and periodic dynamics, allowing a simple threshold method to distinguish between the two dynamic modes.

The detection algorithm was developed to detect a transition from chaotic dynamics to rhythmicity. The strategy was to detect any periodicity and not depend on information regarding the location of the *loss region* in state space [1]. In a plastic system such as the brain the region of the *loss region* may change with time or there may be stable regions in the state space which were previously undiscovered. In these cases the *loss region* approach would not signal a detection of rhythmic activity and no control action would be initiated.

---

[1] The concept of the *loss region* was introduced by Yang et al. [50] and is described in section 4.3.

The benefit of our approach is that the algorithm measures the degree of rhythmicity directly by observing a window of previous values of the time series.

The disadvantage of the strategy of direct observation of rhythmicity is that to observe the behaviour it must be in progress. This problem was particularly acute in application to the MCO model. Given our objective of re-establishing chaotic activity as quickly as possible, it is desirable to minimize the duration of the rhythmic activity before the detection occurs. The duration of the observing window, $\mathcal{N}$, is one of the factors affecting the delay in detection. The detection algorithm determines the divergence statistic, τ, as an average across the entire window. If the subject system slips into rhythmic activity, we then have to wait until the rhythmicity dominates the observer divergence over the window. Thus, the larger the window, the larger the delay in detection of the rhythmic activity. However, reducing the size of the observer window risks having the longer period rhythmicities go undetected. For example, in detecting the period-30 Henon map dynamics, choosing a window size of less than $30 + \mathcal{M}$ [2] would result in no ϵ-neighbours by which to evaluate the divergence.

A solution to the competing objective of speed and reliability may be to encorporate the concept of the *loss region* of Yang et al. [50] in the detection algorithm of Chapter 6. The *loss region* could be defined by the location in state space of the ϵ-neighbours who resulted in a positive detection of rhythmicity. In this way, the loss region could be constructed while not interfering with the function of the detection algorithm. Then the control algorithm would be initiate either by the regular detection algorithm or by the trajectory entering the *loss region*. The compromise could eliminate both disadvantages of using a *loss region*. The detection algorithm would find the rhythmicities for which there is no identified *loss region* eliminating the problem of undetected rhythmicities. The plastic character of brain dynamics could be represented by having a finite memory for each *loss region*. We can envision this hybrid detection algorithm in a process of continually creating and destroying individual *loss regions* as the neurodynamics change over time.

---

[2]see section 6.2 for details

8.1.3 Making Chaos from Rhythmicity

Chapter 7 concerned the development of a strategy for the restoration of chaotic dynamics in systems which have drifted into the periodic regime. We showed that by appropriately timing a variable perturbation such that the state trajectory lands on the unstable manifold of the periodic or rhythmic orbit, we can initial temporary chaotic activity in the subject systems.

The duration of the induced chaotic activity in both the Henon map and the MCO model was variable. In both systems, some variable placements resulted in chaotic activity of almost no duration. Still others result in significant periods of chaotic activity. This is particularly true for the application to the Henon map where one transient endured for over 1000 time steps. Previously, we mentioned that the SDIC characteristic of chaotic systems made it impossible to distinguish *a priori* the quality of the various control actions. While this is largely true, the possibility exists that, in the case of the very short chaotic transients, the perturbed variable is placed on a region of the unstable manifold corresponding to a low order preiterate of the *loss region* [3]. In such a situation, a control algorithm should be capable of resolving the low order preiterates and avoid placing the state trajectory in these regions. The control algorithm developed in Chapter 7 placed priority on initiating the control action as soon as possible and risked potentially placing the trajectory on a preiterate of the *loss region*. The approach was appropriate for a system such as the Henon map where the average duration of the induced chaotic transient was large (500 time steps). In the case of the MCO dynamics, the induced intermittent chaotic activity was generally quite short and possibly could have benefit from a determination of the preiterates.

The strategy to repeat detection and control in each incidence of rhythmicity results in a control algorithm which is able to match the required degree of control interference with the autonomous action of the subject systems. The periodic Henon map dynamics exhibited typically long chaotic transients and, therefore, was given relatively few control actions. On the other hand, the intermittent MCO model, displayed rather short chaotic burst when stimulated and thus required more frequent control activity. In essence, the strategy uses the natural dynamics of the subject systems to the extent that it is able.

---

[3]See section 4.3 and [50] for details

Figure 7.9, of the control algorithm applied to the intermittent MCO model interspike interval dynamics, illustrates a significant variety in the time between the time of detection of rhythmicity and the initiation of a control action. The last control action occurred after more than a 100 time steps from the time of rhythmicity detection. The source of the variability is not obvious. The type of rhythmicity occurring in this system is nearly period-1, implying that each iteration of the state vector, I_n, is found in approximately the same region of state space. Why should it be that one of these seemingly identical vectors finds itself in a position amendable to placement on the unstable manifold? We speculate that the answer lies in the estimation of the unstable manifold rather that in some inherent property of the subject system. In the estimation of the unstable manifold we iterate a population of vectors originating from a random distribution within an ϵ-neighbourhood of a point in the rhythmic orbit. Perhaps the number of iterations of the RBF model is insufficient to cover the entire four dimensional strange attractor of the chaotic MCO model. If this is the case, then it is possible that the region corresponding to the part of the unstable manifold in the accessible region of state space (defined by the two criteria of section 7.1.2) is frequently not represented in the estimation of the unstable manifold and as a result no control action is taken. If this proposed situation is true, then the suggests of Kostelich et al. [45] to improve targeting in higher dimensional systems could be applied to improve our manifold estimation without excessive computational burden.

8.1.4 Comparison to Current Research

In Chapter 4, we present two contrasting perspectives on the problem of maintaining chaos in biological systems. The first perspective is that of Schiff et al. [1], who attempted to *anticontrol* chaos in the rat hippocampal slice. They used linear regression to fit eigenvectors and find an unstable saddle point in the first return map of the interspike interval. Their efforts to maintain chaos in the neuronal tissue was limited to eliciting action potentials, through stimulation, such that the interspike interval landed off the eigenvectors. Their perspective was one of increasing the variability in the neuronal activity over that observed by their model.

The second perspective on the subject of preserving chaos in biological systems, offered

by Yang et al. [50], is centered around systems which transition from healthy chaotic activity to "pathological" periodicities. Their demonstrations of maintaining the chaotic dynamics involved using the system equations to calculate perturbations of a control parameter which would counter the parameter drift into periodicity.

We believe our approach to the problem rests somewhere between these two diverse perspectives. The approach of Yang et al. seems critically dependent on the presence of system equations and, in particular, a control parameter. We suggest that no equations exists to appropriately describe the target application: the brain. Without system equations, using a control parameter would require exploratory parameter manipulations to learn the system response. Experimental manipulations may not be considered exceptable in a therapeutic application. While sharing Yang et al.'s focus on the transition from chaotic to rhythmic dynamics, we believe that the ability of our strategy to learn the necessary dynamics by passively observing the system activity is a considerable advantage.

Comparing our approach to that of Schiff et al., we see that both strategies employ model estimation from time series and make perturbations directly to the system variable. However, unlike our strategy and that of Yang et al., Schiff et al. do not consider the system as having gone through a transition. They focus their efforts on learning the low dimensional epileptic dynamics, whereas we focus on learning the higher complexity dynamics of the healthy activity. Our advantage is that once a transition to rhythmicity is detected, the initiation of a control action may begin immediately without a lengthy learning stage during the seizure activity. The approach of Schiff et al. has the advantage of learning the less complex dynamics which could be a considerably easier task than learning the high complexity dynamics.

The choice of time series model is a second point of comparison between our approach and that of Schiff et al.. The algorithm of Schiff et al. learn the local dynamics of a unstable periodic orbit (UPO) by fitting linear eigenvectors in the two dimensional first return map. The goal of our RBF model is to learn the global dynamics of the chaotic system representable in any dimension. The literature regarding the detection of nonlinearities in neuronal activity, reviewed in Chapter 3, largely suggests that embedding the interspike interval in a two dimensional state space will result in a significant number of false nearest neighbours, complicating the learning of deterministic dynamics. In the applications of chaos

112

control algorithms, the local dynamics may be well described by the two dimensional linear model; however in instances of *anticontrol*, the dynamics of interest are those of the greater chaotic attractor and not the local dynamics estimated by the model of Schiff et al.

A third distinction between our approach and that of Schiff et al. may be drawn between the two control strategies. We have attempted to implement a strategy which, by using the estimate of the unstable manifold of the higher complexity manifold, we would use the natural dynamics of the system to maintain chaotic activity through instances of rhythmicity. Schiff et al. do not model the dynamics outside the low dimensional epileptic activity and, as a result, are left with a somewhat arbitrary choice of variable placement somewhere outside the modeled dynamics.

8.1.5 Contributions

In regard to the RBF model parameter estimation, we believe this to be the first application of the OLS basis function selection algorithm as the front end of a nonlinear optimization strategy. Originally, the algorithm was presented as the entire parameter estimation algorithm. In the learning of MCO model parameters, we show that the gradient descent is able to substantially improve on the performance of the system provided to it from the OLS learning algorithm. We also believe that this is the first application of nonlinear optimization methods to RBF models of chaotic systems.

The detection strategy developed in this thesis is novel. The detection statistic, τ from 6.1, was defined to combine consecutive dynamics in an effort to involve as much of the time series as possible in the determination of a mean in order to increase statistical significance.

We believe the control algorithm to be the first application of a modified targeting algorithm to target the unstable manifold, rather than the stable manifold. This is also believed to be the first application of the targeting algorithm which is not dependent on having access to accurate system equations or control parameters.

The general approach to the problem of detection and control is unique. Learning the healthy activity and using that knowledge to both detect and suppress the rhythmic dynamics when they occur has not been proposed before as a therapeutic strategy against

epilepsy.

8.1.6 Conclusions

In conclusion, we have developed a novel approach to a potential therapy for individuals with epilepsy. The strategy is to learn the global dynamics of the healthy chaotic system using a RBF model of the time series and to use this model to detect a transition to rhythmicity. Once rhythmicity is detected, the control strategy employs the RBF model to estimate the unstable manifold of the rhythmic orbit upon which it will place the state vector. This has the effect of restoring transient chaotic activity. If and when the rhythmic dynamics return, the detection and control process is repeated.

We applied the chaosmaker to two systems: the Henon map and the mapped clock oscillator (MCO) model. The strategy was successful both at detecting the transition to rhythmicity, and at restoring chaos through a control action. From our initial success we feel that this work should be continued with the goal of clinical application.

8.2 Future Work

This thesis is an exploration of a novel approach to therapy for epilepsy, and as such leads to a great deal of potential for future work. There is much to be done, both theoretically and experimentally, before we are in a position to seriously consider the control of neurodynamics as a therapy for individuals with epilepsy. We begin with what could be done to extend this work in the short term and then conclude with a discussion of more involved projects.

The three most pressing concerns for future development of the chaosmaker are those raised in the Discussion. First, we require a better nonlinear optimization scheme than the gradient descent algorithm if we wish to attempt the learning of more complex dynamics. Second, the concept of the *loss region* should be encorporated into the detection algorithm to speed the detection of recurrent rhythmicities. Finally, the possibility of checking for preiterate of the *loss region* of a prospective variable placement should be explored.

A slightly more involved project, which is certainly required to show true viability of the chaosmaker, is the development of the time varying version, whose parameters change with time.

In the longer term, a comparison should be made of a number of different time series models. They should be evaluated on their suitability to application in the chaosmaker. Also a probablistic version of the chaosmaker, the noisemaker, should be developed and compared with the chaosmaker in an application to neuronal tissue control.

Bibliography

[1] S. J. Schiff, K. Jerger, D. H. Duong, T. Chang, M. L. Spano, and W. L. Ditto, "Controlling chaos in the brain," *Nature,* vol. 370, pp. 615–620, 1994.

[2] S. H. Strogatz, *Nonlinear Dynamics and Chaos.* Addison-Wesley Publishing Company, 1994.

[3] F. Takens, "Detecting strange attractors in turbulence," in *Lecture Notes in Mathematics,* vol. 898, New York: Springer, 1981.

[4] H. Kantz and T. Schreiber, *Nonlinear time series analysis.* Cambridge Nonlinear Science Series 7, Cambridge University Press, 1997.

[5] T. Sauer, "Reconstruction of dynamical systems from interspike intervals," *Physical Review Letters,* vol. 72, p. 3811, 1994.

[6] T. Sauer, "Interspike embedding of chaotic signals," *Chaos,* vol. 5, p. 127, 1995.

[7] H. Kantz, "A robust method to estimate the maximal lyapunov exponent of a time series," *Physics Letters A,* vol. 185, pp. 77–87, January 1994.

[8] P. Grassberger and I. Procaccia, "Measuring the strangeness of strange attractors," *Physica D,* vol. 9, p. 189, 1983.

[9] R. Aschenbrenner-Schiebe, "Chaos and entrainment in hippocampal neurons," Master's thesis, University of Toronto, 1995.

[10] B. L. Bardakjian and N. E. Diamant, "A mapped clock oscillator model for transmembrane electrical rhythmic activity in excitable cells rhythmic activity in excitable cells," *J. Theor. Biol.,* vol. 166, pp. 225–235, 1994.

[11] P. E. Rapp, I. D. Zimmerman, A. M. Albano, G. C. Deguzman, and N. N. Greengaun, "Dynamics of spontaneous neural activity in the simian motor cortex: The dimension of chaotic neurons," *Physics Letters*, vol. 110A, pp. 335–338, August 1985.

[12] A. R. Osborne and A. Provenzula, "Finite correlation dimension for stochastic systems with power-law spectra," *Physica D*, vol. 35, pp. 357–381, 1989.

[13] P. E. Rapp, "Chaos in the neurosciences: cautionary tales from the frontier," *Biologist*, vol. 40, pp. 89–94, 1993.

[14] J. P. Pijn, J. V. Neerven, A. Noest, and F. H. L. da Silva, "Chaos or noise in eeg signals; dependence on state and brain site," *Electroencephalography and clinical Neurophysiology*, vol. 79, pp. 371–381, 1991.

[15] J. Theiler, S. Eubank, A. Longtin, B. Galdrikian, and J. D. Farmer, "Testing for nonlinearity in time series: the method of surrogate data," *Physica D*, vol. 58, pp. 77–94, 1992.

[16] T. Chang, S. Schiff, T. Sauer, J.-P. Gossard, and R. E. Burke, "Stochastic versus deterministic variability in simple neuronal circuits: I. monosynaptic spinal cord reflexes," *Biophysical Journal*, vol. 67, pp. 671–683, August 1994.

[17] S. Schiff, K. Jerger, T. Chang, T. Sauer, and P. G. Aitken, "Stochastic versus deterministic variability in simple neuronal circuits: Ii. hippocampal slice," *Biophysical Journal*, vol. 67, pp. 684–691, August 1994.

[18] P. Cvitanovic, "Invariant measurement of strange sets in terms of cycles," *Physical Review Letters*, vol. 61, pp. 2729–2732, December 1988.

[19] X. Pei and F. Moss, "Characterization of low-dimensional dynamics in the crayfish caudal photoreceptor," *Nature*, vol. 379, pp. 618–621, February 1996.

[20] P. So, J. T. Francis, T. I. Netoff, B. J. Gluckman, and S. J. Schiff, "Periodic orbits: A new language for neuronal dynamics," *Biophysical Journal*, vol. 74, pp. 2776–2785, June 1998.

[21] P. So, E. Ott, S. J. Schiff, D. T. Kaplan, T. Sauer, and C. Grebogi, "Detecting unstable periodic orbits in chaotic experimental data," *Physical Review Letters*, vol. 76, pp. 4705–4708, 1996.

[22] P. So, E. Ott, T. Sauer, B. J. Gluckman, C. Grebogi, and S. J. Schiff, "Extracting unstable periodic orbits from chaotic time seires data," *Physical Review E*, vol. 55, pp. 5398–5417, 1997.

[23] A. Babloyantz, J. M. Salazar, and C. Nicolis, "Evidence of chaotic dynamics of brain activity during the sleep cycle," *Physics Letters*, vol. 111A, pp. 152–156, September 1985.

[24] R. Cerf, A. Daoudi, M. O. Henoune, and E. H. E. Ouasda, "Episodes of low-dimensional self-organized dynamics from electroencephalographic α-signals," *Biological Cybernetics*, vol. 77, pp. 235–245, 1997.

[25] W. J. Freeman, "Strange attractors that govern mammalian brain dynamics shown by trajectories of electroencephalographic (eeg) potential," *IEEE Transactions on Circuits and Systems*, vol. 35, pp. 781–783, 1988.

[26] W. J. Freeman, "Tutorial on neurology: From single neurons to brain chaos," *International Jounal of Bifurcation and Chaos*, vol. 2, no. 3, pp. 451 – 482, 1992.

[27] J. A. S. Kelso and A. Fuchs, "Self-organizing dynamics of the human brain: Critical instabilities and sil'nikov chaos," *Chaos*, vol. 5, no. 1, pp. 64–69, 1995.

[28] M. C. Mackey and J. G. Milton, "Dynamical disease," *Annals New York Academy of Sciences*, vol. 504, pp. 16–32, 1987.

[29] J. Milton and D. Black, "Dynamic disease in neurology and psychiatry," *Chaos*, vol. 5, no. 1, pp. 8–13, 1995.

[30] A. Babloyantz and A. Destexhe, "Low-dimensional chaos in an instance of epilepsy," *Proc. Natl. Acad. Sci. USA*, vol. 83, pp. 3515–3517, May 1986.

[31] M. C. Casdagli, L. D. Iasemidis, R. S. Savit, R. L. Gilmore, S. N. Roper, and J. C. Sackellares, "Non-linearity in invasive eeg recordings from patients with temporal lobe

epilepsy," *Electroencephalography and clinical Neurophysiology*, vol. 102, pp. 98–105, 1997.

[32] M. L. V. Quyen, J. Martinerie, C. Adam, and F. J. Varela, "Unstable periodic orbits in human epileptic activity," *Rhysical Review E*, vol. 56, pp. 3401–3411, September 1997.

[33] J. L. P. Velazquez, H. Khosravani, A. Lozano, B. L. P. L. Carlen, and R. Wennberg, "Type iii intermittency in human partial epilepsy," *European Journal of Neuroscience*, vol. 11, pp. 1–6, 1999.

[34] E. Ott, C. Grebogi, and J. A. Yorke, "Controlling chaos," *Physical Review Letters*, vol. 64, no. 11, pp. 1196 – 1199, 1990.

[35] W. L. Ditto, M. L. Spano, and J. F. Linder, "Techniques for the control of chaos," *Physica D*, vol. 86, pp. 198 – 211, 1995.

[36] D. Auerbach, C. Grebogi, E. Ott, and J. A. Yorke, "Controlling chaos in high dimensional systems," *Physical Review Letters*, vol. 69, no. 24, pp. 3479–3482, 1992.

[37] M. Ding, W. Yang, V. In, W. Ditto, M. L. Spano, and B. Gluckman, "Controlling chaos in high dimenison: Theory and experiment," *Physical Review E*, vol. 53, no. 5, pp. 4334–4344, 1996.

[38] M. Ding, E.-J. Ding, W. L. Ditto, B. Gluckman, V. In, J.-H. Peng, M. L. Spano, and W. Yang, "Control and synchronization of chaos in high dimensional system: Review of some recent results," *Chaos*, vol. 7, no. 4, pp. 644–652, 1997.

[39] C. Grebogi and Y.-C. Lai, "Controlling chaos in high dimensions," *IEEE Transactions on Circuits and Systems I*, vol. 44, no. 10, pp. 971–975, 1997.

[40] W. L. Ditto, S. N. Rauseo, and M. L. Spano, "Experimental control of chaos," *Physical Review Letters*, vol. 65, no. 26, pp. 3211–3214, 1990.

[41] E. R. Hunt, "Stabilizing high-period orbits in a chaotic system: The diode resonator," *Physical Review Letters*, vol. 67, no. 15, pp. 1953–1955, 1991.

[42] T. Shinbrot, E. Ott, C. Grebogi, and J. A. Yorke, "Using chaos to direct trajectories to targets," *Physical Review Letters*, vol. 65, no. 26, pp. 3215–3218, 1990.

[43] T. Shinbrot, E. Ott, C. Grebogi, and J. A. Yorke, "Using chaos to direct orbits to targets in systems describable by a one-dimensional map," *Physical Review A*, vol. 45, no. 6, pp. 4165–4168, 1992.

[44] T. Shinbrot, "Progress in the control of chaos," *Advances in Physics*, vol. 44, no. 2, pp. 73–111, 1995.

[45] E. J. Kostelich, C. Grebogi, E. Ott, and J. A. Yorke, "Higher-dimensional targeting," *Physical Review E*, vol. 47, pp. 305–310, January 1993.

[46] A. Garfinkel, M. L.Spano, W. L. Ditto, and J. N. Weiss, "Controlling cardiac chaos," *Science*, vol. 257, pp. 1230–1235, 1992.

[47] J. M. Weiss, A. Garfinkel, M. L. Spano, and W. L. Ditto, "Chaos and chaos contorl in biology," *Journal of Clinical Investigations*, vol. 93, pp. 1355–1360, April 1994.

[48] K. Hall, D. J. Christini, M. Tremblay, J. J. Collins, L. Glass, and J. Billette, "Dynamic contorl of cardiac alternans," *Physical Review Letters*, vol. 78, no. 23, pp. 4518–4521, 1997.

[49] D. J. Christini and J. Collins, "Control of chaos in excitable physiological systems: A geometric analysis," *Chaos*, vol. 7, no. 4, pp. 544–549, 1997.

[50] W. Yang, M. Ding, A. J. Mandell, and E. Ott, "Perserving chaos: Control strategies to preverve complex dynamics with potential relavance to biological disorders," *Physical Review E*, vol. 51, no. 1, pp. 102–110, 1995.

[51] D. J. Christini, "Controlling nonchaotic neuronal noise using chaos control techniques," *Physical Review Letters*, vol. 75, no. 14, pp. 2782–2785, 1995.

[52] F. M. A. Acosta, "Radial basis function and related models: An overview," *Signal Processing*, vol. 45, pp. 37–58, 1995.

[53] J. Park and I. W. Sandberg, "Universal approximation using radial basis function networks," *Neural Computation*, vol. 3, pp. 247–257, 1991.

[54] S. Haykin and J. Principe, "Making sense of a complex world," *IEEE Signal Processing Magazine*, pp. 66–81, May 1998.

[55] M. Casdagli, "Nonlinear prediction of chaotic time series," *Physica D*, vol. 35, pp. 335–356, 1989.

[56] W. H. Press, S. A. Teukolsky, W. T. Vetterling, and B. P. Flannery, *Numerical Recipes in C: The Art of Scientific Computing*. New York: Cambridge University Press, second ed., 1994.

[57] C. M. Bishop, *Neutral Networks for Pattern Recognition*. Clarendon Press, 1995.

[58] S. Chen, C. F. N. Cowan, and P. M. Grant, "Orthogonal least squares learning algorithm for radial basis function networks," *IEEE Transactions on Neural Networks*, vol. 2, no. 2, pp. 302–309, 1991.

[59] J. T. McClave, I. Frank H. Dietrich, and T. Sincich, *Statistics*. Prentice Hall, 7th ed., 1997.